

# The Application of Negative Refractive Index Metamaterials to mm and Sub-mm Wavelength Instrumentation

A thesis submitted to The University of Manchester for the degree of  
Doctor of Philosophy  
in the Faculty of Engineering and Physical Sciences

**2013**

**Imran Mohamed**  
**School of Physics and Astronomy**



# Contents

List of Figures	9
List of Tables	17
Abstract	19
Declaration	21
Copyright Statement	22
Dedication	24
Acknowledgements	25
The Author	27
Supporting Publications	28
Acronyms & Initialisms	29
Symbols	30
<b>1 Negative Refractive Indices &amp; Metamaterials</b>	<b>31</b>
1.1 Introduction . . . . .	31
1.2 Material Parameters . . . . .	33
1.2.1 Permittivity . . . . .	33

## CONTENTS

1.2.2	Permeability . . . . .	36
1.2.3	Refractive Index & Impedance . . . . .	36
1.3	Negative Refractive Indices . . . . .	38
1.3.1	Negative Refraction . . . . .	38
1.3.2	Superlensing . . . . .	40
1.3.3	Backward Waves . . . . .	44
1.4	A Brief History of Negative Refractive Index Metamaterials . . . . .	45
1.5	A Role for NRI Metamaterials in Astronomical Instrumentation . . . . .	50
1.5.1	Lenses . . . . .	51
1.5.2	Wave Plates . . . . .	52
1.6	Thesis Outline . . . . .	53
<b>2</b>	<b>Designing Metamaterials</b>	<b>55</b>
2.1	Introduction . . . . .	55
2.2	Finite Element Method Modelling & HFSS . . . . .	56
2.2.1	Designing & Drawing . . . . .	56
2.2.2	Boundary Conditions . . . . .	57
2.2.3	Excitations . . . . .	60
2.2.4	Simulation Process . . . . .	61
2.2.5	Frequency Sweeps . . . . .	61
2.3	Transmission Line Modelling . . . . .	63
2.4	The New Transmission Line Model . . . . .	65
2.4.1	FEM Seeding of Transmission Line Matrices . . . . .	65
2.4.2	Comparison Between FEM & New TL Model . . . . .	68
<b>3</b>	<b>Manufacturing Metamaterials</b>	<b>73</b>
3.1	Introduction . . . . .	73
3.2	Metamaterial Fabrication . . . . .	74
3.2.1	Photolithography . . . . .	74
3.2.1.1	Mounting & Polypropylene Annealing . . . . .	74

3.2.1.2	Copper Coating . . . . .	76
3.2.1.3	Photoresist Coating . . . . .	77
3.2.1.4	Photo Mask Production & Exposure . . . . .	77
3.2.1.5	Development & Etching . . . . .	80
3.3	Device Manufacture . . . . .	81
3.3.1	Alignment & Stacking . . . . .	81
3.3.2	Hot Pressing & Bonding . . . . .	85
3.4	Alternative Manufacturing Techniques . . . . .	87
<b>4</b>	<b>Artificial Dielectrics with Metamaterials</b>	<b>89</b>
4.1	Introduction . . . . .	89
4.2	Material Parameter Extraction . . . . .	90
4.2.1	Nicolson-Ross-Weir Method . . . . .	90
4.2.2	Robust Parameter Extraction Method . . . . .	93
4.2.3	Testing of Material Parameter Extraction Method . . . . .	97
4.2.3.1	Effective Surface . . . . .	98
4.2.3.2	Refractive Index . . . . .	100
4.3	Negative Refractive Index Slab . . . . .	102
4.3.1	NRI Block Design & Modelling . . . . .	102
4.3.2	Modified Parameter Extraction Method . . . . .	108
4.3.3	NRI Slab Design . . . . .	113
4.3.4	Manufacture . . . . .	115
4.3.5	Measurements . . . . .	118
4.3.6	Results . . . . .	120
4.4	Conclusions . . . . .	131
<b>5</b>	<b>Highly Birefringent Artificial Dielectrics</b>	<b>133</b>
5.1	Introduction . . . . .	133
5.2	Birefringence . . . . .	134
5.3	Highly Birefringent Metamaterials . . . . .	135

## CONTENTS

5.3.1	Narrowband Implementations . . . . .	135
5.3.2	Increasing the Bandwidth with the Pancharatnam Method	136
5.3.3	TL Modelling of the Pancharatnam Method . . . . .	138
5.4	Air Gap Half Wave Plates . . . . .	143
5.4.1	Theory & Application . . . . .	143
5.4.2	Design . . . . .	143
5.4.3	Manufacture . . . . .	148
5.4.4	Measurements . . . . .	150
5.4.5	Results . . . . .	151
5.5	Embedded Quarter Wave Plates . . . . .	156
5.5.1	Theory & Applications . . . . .	156
5.5.2	Design . . . . .	157
5.5.3	Manufacture . . . . .	163
5.5.4	Measurements . . . . .	164
5.5.5	Results . . . . .	164
5.6	Conclusions . . . . .	168
<b>6</b>	<b>Summary, Conclusions &amp; Further Work</b>	<b>169</b>
6.1	Introduction . . . . .	169
6.2	FEM Seeded Transmission Line Modelling . . . . .	170
6.3	Photolithography & Grid Alignment . . . . .	171
6.4	Material Parameter Extraction & the Negative Refractive Index Slab	172
6.5	Highly Birefringent Wave Plates . . . . .	173
6.5.1	Air Gap Half Wave Plate . . . . .	174
6.5.2	Polypropylene Embedded Quarter Wave Plate . . . . .	174
6.6	Summary of Results . . . . .	175
6.7	Conclusions . . . . .	176
6.8	Suggestions for Further Work . . . . .	178
6.8.1	Negative Refractive Index Slab . . . . .	178

6.8.2 Metamaterials with Other Refractive Index Values . . . . . 178

**References** . . . . . **179**

**Approximate Word Count:** 27 000

*CONTENTS*

# List of Figures

1.1	Electron clouds without and with an electric field applied to them.	34
1.2	Light rays undergoing positive and negative refraction. . . . .	39
1.3	Light rays travelling through blocks with refractive indices $> 1$ and equal to $-1$ . . . . .	40
1.4	Radiation scattering off surfaces with features sizes larger than and smaller than the radiation's wavelength. . . . .	41
1.5	Diagram showing the backward and forward $E$ -fields of radiation incident on, reflected from and transmitted through a slab. . . . .	42
1.6	A wave's phase and group velocity within a positive and negative refractive index medium. . . . .	44
1.7	Wire grid and Split Ring Resonator (SRR) structures. . . . .	46
1.8	A close up the split ring resonator and wire structure used in Shelby et al. (2001b) to demonstrate negative refractive indices. . . . .	48
1.9	Origin of planar metmaterials magnetic response to incident $E$ -fields.	49
1.10	Gallery of different planar unit cell designs. . . . .	50
2.1	A Jerusalem Cross Pair (JCP) unit cell within an air box, both drawn in HFSS. . . . .	58
2.2	Modelling a Jerusalem Cross Pair (JCP) with different boundary conditions. . . . .	59
2.3	A Jerusalem Cross Pair (JCP) after being meshed by HFSS. . . . .	62
2.4	Side view of an air box containing a single unit cell. . . . .	66

*LIST OF FIGURES*

2.5	Diagram of the simulation layout used in the two PEC square case in section 2.4.2. . . . .	69
2.6	Finite Element Method (FEM) modelling vs. FEM seeded Transmission Line (TL) modelling. . . . .	70
2.7	Finite Element Method (FEM) modelling vs. FEM seeded Transmission Line (TL) modelling. . . . .	71
3.1	Five 10 cm aluminium rings on top of a sheet of polypropylene. . .	75
3.2	Rings with polypropylene being annealed inside fan oven. . . . .	75
3.3	A freshly copper coated polypropylene sample 53 cm in diameter. . .	77
3.4	Photo mask on the vacuum tray. . . . .	78
3.5	Positioning of copper sample on photo mask. . . . .	79
3.6	Vacuum tray containing the photo mask and sample about to loaded into the exposure box. . . . .	79
3.7	Copper coated PP sample in etching solution above light box. . .	80
3.8	Copper sample after etching is complete. . . . .	81
3.9	Two grids layered on top of one another and held down with a cylindrical glass block, part 1. . . . .	83
3.10	Two grids layered on top of one another and held down with a cylindrical glass block, part 2. . . . .	83
3.11	Two grids layered on top of one another and held down with a cylindrical glass block, part 3. . . . .	84
3.12	An example of an alignment mark. . . . .	84
3.13	Spot welded sample to be bonded resting on teflon sheet and bottom press plate. . . . .	86
3.14	Sample inside of the vacuum oven. . . . .	86
4.1	Side on view of the parameter extraction setup in HFSS simulations. . .	91
4.2	Schematic of an experimental equivalent to the parameter extraction setup shown in figure 4.1. . . . .	91

4.3 Diagram showing the difference between weakly and strongly coupled metamaterial setups. . . . . 96

4.4 Graph taken from Zhou et al. (2009, figure 4) showing the refractive index calculated for different numbers of cascaded “tightly coupled” metamaterial unit cells based on a fishnet design (figure 1.10e). . . 96

4.5 Schematic of the HFSS setup for the parameter extraction test. . . 97

4.6 Surface plot of the cost function, equation (4.12), between 2 mm and 3 mm thick blocks of water. . . . . 99

4.7 Calculated values of silicon’s refractive index based on  $S_{11}$  and  $S_{21}$  data from HFSS simulations. . . . . 100

4.8 The calculated refractive index,  $n$ , of the 0.8 mm blocks of water, polypropylene (PP) and imaginary negative material (INM). . . . 101

4.9 The calculated relative permittivity,  $\epsilon_r$ , of the 0.8 mm blocks of silicon, water, polypropylene (PP) and imaginary negative material (INM). . . . . 101

4.10 The calculated relative permeability,  $\mu_r$ , of the 0.8 mm blocks of silicon, water, polypropylene (PP) and imaginary negative material (INM). . . . . 102

4.11 Schematic of the unit cell used in the making of the negative refractive index block. . . . . 103

4.12 Drawing showing the arrangement of the unit cells when they are cascaded. . . . . 104

4.13 Convergence of  $\text{Re}(n)$  of the first fishnet design. . . . . 105

4.14  $\text{Im}(n)$  of the first fishnet design with various numbers of cascaded unit cells. . . . . 106

4.15 Convergence of  $\text{Re}(n)$  of the second fishnet design. . . . . 107

4.16  $\text{Im}(n)$  of the second fishnet design with various numbers of cascaded unit cells. . . . . 108

4.17 The transmitted intensity of the second fishnet design. . . . . 108

*LIST OF FIGURES*

4.18 The reflected intensity of the second fishnet design. . . . . 109

4.19 The absorption of the second fishnet design. . . . . 109

4.20 Schematic of the modified parameter extraction setup. . . . . 110

4.21 The value of  $n$  for a 3 mm block of silicon with a 1.426 mm coat of polypropylene calculated from the embedded parameter extraction equations, equation (4.23). . . . . 113

4.22 Photo demonstrating how seven 6 cm circles may be cut from a larger 21 cm sample. . . . . 114

4.23 Recipe for the three unit cell structure consisting of six fishnet grids. 115

4.24 Layer A copper side down on top of a light box before initial alignment. The curling effect is evident. . . . . 116

4.25 Transmitted intensity,  $|S_{21}|^2$  of Layer C as simulated by HFSS (dashed) and experimentally measured by the VNA (solid). . . . . 116

4.26 Transmitted phase,  $\arg(S_{21})$ , of Layer C as simulated by HFSS (dashed) and experimentally measured by the VNA (solid). . . . . 117

4.27 Diagram of the experimental setup used for the transmission readings of the individual layers and the combined layers. . . . . 119

4.28 Annotated photo of an experimental set up for transmission readings of individual layers and the combined layers. . . . . 119

4.29 Diagram of the experimental setup used for the reflection readings of the hot pressed layers. . . . . 120

4.30 Annotated photo of an experimental set up for reflection readings of individual layers and the combined layers. . . . . 120

4.31 Trasmitted intensity,  $\text{dB}(S_{21})$ , readings taken along the  $x$ -axis for the spot welded layers ABCDEF. . . . . 122

4.32 Trasmitted phase,  $\arg(S_{21})$ , readings taken along the  $x$ -axis for the spot welded layers ABCDEF. . . . . 122

4.33 Layer A side of the spot welded layers ABCDEF. . . . . 123

4.34 Transmitted intensity,  $\text{dB}(S_{21})$ , readings taken along the  $x$ -axis for the spot welded layers ABCDEF sandwiched between two  $47\ \mu\text{m}$  polypropylene sheets. . . . . 124

4.35 Transmitted phase,  $\text{arg}(S_{21})$ , readings taken along the  $x$ -axis for the spot welded layers ABCDEF sandwiched between two  $47\ \mu\text{m}$  polypropylene sheets. . . . . 124

4.36 Transmitted intensity,  $|S_{21}|^2$ , readings taken along the  $x$ -axis of the spot welded layers DEF sandwiched between two  $47\ \mu\text{m}$  polypropylene sheets to squash the layers together and ensure more thorough contact between the layers. . . . . 125

4.37 Transmitted phase,  $\text{arg}(S_{21})$ , readings taken along the  $x$ -axis of the spot welded layers DEF sandwiched between two  $47\ \mu\text{m}$  polypropylene sheets. . . . . 125

4.38 Transmitted intensity,  $|S_{21}|^2$ , readings taken along the  $x$ -axis of the hot pressed layers DEF. . . . . 126

4.39 Transmitted phase,  $\text{arg}(S_{21})$ , readings taken along the  $x$ -axis of the hot pressed layers DEF. . . . . 126

4.40 Transmitted intensity,  $|S_{21}|^2$ , readings taken along the  $x$ -axis of the hot pressed layers ABCDEF. . . . . 127

4.41 Transmitted phase,  $\text{arg}(S_{21})$ , readings taken along the  $x$ -axis of the hot pressed layers ABCDEF. . . . . 127

4.42 Reflected intensity,  $|S_{11}|^2$ , readings taken along the  $x$ -axis of the hot pressed layers ABCDEF. . . . . 129

4.43 Reflected phase,  $\text{arg}(S_{11})$ , readings taken along the  $x$ -axis of the hot pressed layers ABCDEF. . . . . 129

4.44 The real part of the refractive index,  $\text{Re}(n)$ , of the negative index block. . . . . 130

4.45 The imaginary part of the refractive index,  $\text{Im}(n)$ , of the negative index block. . . . . 130

*LIST OF FIGURES*

5.1 The arrangement of the polarisation states on the surface of the Poincarè sphere. Image taken from Savini et al. (2006, Figure 1). . . 137

5.2 Schematic of Dog Bone Triplet (DBT) cell used to create Half Wave Plate (HWP). . . . . 144

5.3 HFSS simulated transmitted intensity,  $|S_{21}|^2$ , of  $x$ - and  $y$ - polarised radiation after passing through a single Dog Bone Triplet (DBT). 145

5.4 HFSS simulated phase difference,  $\Delta\phi$ , between the  $x$ - and  $y$ - polarised radiation after passing through a single Dog Bone Triplet (DBT). . . . . 146

5.5 The refractive indices along the  $x$ -axis calculated from HFSS simulation data of a single Dog Bone Triplet (DBT). . . . . 146

5.6 The refractive indices along the  $y$ -axis calculated from HFSS simulation data of a single Dog Bone Triplet (DBT). . . . . 147

5.7 Side on and face on views of the Pancharatnam based Half Wave Plate (HWP) design). . . . . 147

5.8 Transmitted intensity,  $|S_{21}|^2$ , of Pancharatnam based Half Wave Plate (HWP) (figure 5.7) calculated with the TL based code. . . . 148

5.9 Transmitted phase difference,  $\Delta\phi$ , of Pancharatnam based Half Wave Plate (HWP) (figure 5.7) calculated with the TL based code. 149

5.10 The recipes for the Dog Bone Triplet Half Wave Plates (DBT-HWP).150

5.11 Schematic outline of the experimental set up. . . . . 151

5.12 The expected and experimental transmitted intensities,  $|S_{21}|^2$ , as modelled by the TL based code (dashed lines) and from the VNA readings (solid lines) respectively. . . . . 152

5.13 The differential phase,  $\Delta\phi$ , between the transmitted radiation's  $x$ - and  $y$ -axes. . . . . 153

5.14 An example of the misalignment between the individual layers that make up the Dog Bone Triplets (DBT). . . . . 153

5.15 The measured transmitted phase differences (solid lines) of the individual DBT-HWPs that made the first version of the Pancharatnam based HWP compared to the expected result as simulated by HFSS (dashed). . . . . 154

5.16 The measured transmitted phase differences (solid lines) of the individual DBT-HWPs that made the second version of the Half Wave Plate (HWP) compared to the expected result as simulated by HFSS (dashed). . . . . 154

5.17 The experimental and expected transmitted intensities,  $|S_{21}|^2$ , as modelled by the TL based code (dashed lines) and from the VNA readings (solid lines) respectively of the second version of the Half Wave Plate (HWP). . . . . 155

5.18 The differential phase,  $\Delta\phi$ , between the transmitted radiation's  $x$ - and  $y$ -axes of the second version of the Half Wave Plate (HWP). . . 155

5.19 Schematic of cut wire pair cell used for the Quarter Wave Plate (QWP). . . . . 158

5.20 HFSS simulated transmitted intensity,  $|S_{21}|^2$ , data of the cut wire pair geometry embedded within polypropylene. . . . . 158

5.21 HFSS simulated transmitted phase difference,  $\Delta\phi$ , data of the cut wire pair geometry embedded within polypropylene. . . . . 159

5.22 The refractive index along the  $x$ -axis calculated from HFSS simulation data. . . . . 159

5.23 The refractive index along the  $y$ -axis calculated from HFSS simulation data. . . . . 160

5.24 Side on and face on view of the Pancharatnam based Quarter Wave Plate (QWP). . . . . 160

5.25 The transmitted intensity,  $|S_{21}|^2$ , of the embedded Pancharatnam QWP (figure 5.24) calculated by the TL based code. . . . . 162

*LIST OF FIGURES*

5.26 The transmitted phase difference,  $\Delta\phi$ , of the embedded Pancharatnam QWP (figure 5.24) calculated by the TL based code. . . . . 162

5.27 Recipe for the four unit cell structure of the full quarter wave plate (QWP). . . . . 163

5.28 Transmitted intensity readings of layer A measured experimentally (solid) compared to the data from a HFSS simulation (dashed) of the same layer. . . . . 164

5.29 Transmitted phase difference readings of layer A measured experimentally (solid) compared to the data from a HFSS simulation (dashed) of the same layer. . . . . 165

5.30 Measured (solid) and HFSS simulated (dashed) transmitted intensity readings of CWP-QWP made by spot welding layers G and H together. . . . . 166

5.31 Measured (solid) and HFSS simulated (dashed) phase difference readings of CWP-QWP made by spot welding layers G and H together. . . . . 166

5.32 The experimental (solid) and TL modelled (dashed) of the transmitted intensity data of the full QWP. . . . . 167

5.33 The experimental (solid) and TL modelled (dashed) of the phase difference data of the full QWP. . . . . 167

6.1 “And for my final words...” . . . . . 190

# List of Tables

4.1	Material properties of the blocks simulated in HFSS to test the material parameter extraction method. . . . .	98
4.2	The final values of $x_1$ and $x_2$ from the optimisation of the cost function, equation (4.12). . . . .	99
4.3	The matrices used in equation (4.13). . . . .	111

*LIST OF TABLES*

# The University of Manchester

ABSTRACT OF THESIS submitted by Imran Mohamed for the Degree of Doctor of Philosophy and entitled *The Application of Negative Refractive Index Metamaterials to mm and Sub-mm Wavelength Instrumentation*. December 2013.

The manipulation of electromagnetic radiation via the use of periodic arrays of sub-wavelength metallic structures (unit cells), nowadays named “metamaterials”, has been known of in the microwave engineering community for over fifty years. In the last decade interest in such sub-wavelength structures grew, mainly due to their ability to interact with radiation in ways natural materials could not e.g. by producing a negative refractive index (NRI). This project sought to see whether NRI metamaterials could provide benefits to the mm and sub-mm wavelength astronomical instrumentation currently in use.

To aid rapid design and optimisation of devices made from a cascaded set of metamaterial unit cells, a hybridised Transmission Line (TL) model was developed where the matrix components used in the TL model were “seeded” with data taken from a Finite Element Method (FEM) model of a simpler structure. A comparison between the two found that the TL model was capable of providing results that differed from the FEM model by no more than  $\sim 10^{-4}$  for the transmitted intensity,  $|S_{21}|^2$ , and  $< 1^\circ$  for transmitted phase,  $\arg(S_{21})$ .

A slab of material with a refractive index,  $n = -1$ , can exhibit an effect known as “superlensing”. A three unit cell thick NRI slab was designed, manufactured and experimentally tested. It was found to be capable of producing an NRI across a fractional band of at least 21 %, producing a refractive index value of  $n = -1$  at around 90 GHz. The experimental and simulated transmission and reflection data show good match with each other.

A highly birefringent air gap Half Wave Plate (HWP) was designed, manufactured and experimentally tested. Defining its useful bandwidth as the region where the phase difference, is equal to  $(-180 \pm 3)^\circ$  a single HWP had a fractional bandwidth of 0.3 %. The bandwidth was extended by using the Pancharatnam method, developed in the 1950’s to produce highly achromatic optical wave plates. The method however is applicable to other frequencies and polarisation control technologies. Optimising a three HWP TL-based Pancharatnam model, the HWP’s modelled fractional bandwidth increased to 6.6 %. Experimental data agrees with

the model showing a plateauing of the phase difference at  $-180^\circ$ .

A highly birefringent polypropylene embedded Quarter Wave Plate (QWP) was also designed, manufactured and tested. Defining its useful bandwidth as the region where the differential phase is  $(90 \pm 2)^\circ$  a single QWP produced a fractional bandwidth of 0.6%. By optimising a four QWP TL-based Pancharatnam model, the QWP's performance was improved to 7.8%. Experimental data, whilst not in complete agreement with the model does show a reduction in the gradient of phase difference where it crossed  $90^\circ$ .

It was found that current designs for NRI metamaterials fall short of the standards required to be used in quasi-optical astronomical instrumentation due to high dispersion and absorption. The high dispersion limits NRI metamaterials to uses in instruments built for narrowband applications. Whilst the Pancharatnam method can increase bandwidths where a flat differential phase response is required, this comes at the cost of increased absorption. To reach their full potential, NRI metamaterials' lossiness must be reduced e.g. possibly by cryogenic means or the use of "active" metamaterials.

# Declaration

I declare that no portion of the work referred to in the thesis has been submitted in support of an application for another degree or qualification of this or any other university or other institute of learning.

# Copyright Statement

- (i) The author of this thesis (including any appendices and/or schedules to this thesis) owns certain copyright or related rights in it (the “Copyright”) and s/he has given The University of Manchester certain rights to use such Copyright, including for administrative purposes.
- (ii) Copies of this thesis, either in full or in extracts and whether in hard or electronic copy, may be made only in accordance with the Copyright, Designs and Patents Act 1988 (as amended) and regulations issued under it or, where appropriate, in accordance with licensing agreements which The University has from time to time. This page must form part of any such copies made.
- (iii) The ownership of certain Copyright, patents, designs, trade marks and other intellectual property (the “Intellectual Property”) and any reproductions of copyright works in the thesis, for example graphs and tables (“Reproductions”), which may be described in this thesis, may not be owned by the author and may be owned by third parties. Such Intellectual Property and Reproductions cannot and must not be made available for use without the prior written permission of the owner(s) of the relevant Intellectual Property and/or Reproductions.
- (iv) Further information on the conditions under which disclosure, publication and commercialisation of this thesis, the Copyright and any Intellectual Property and/or Reproductions described in it may take place is available in the University IP Policy<sup>1</sup>, in any relevant Thesis restriction declarations deposited in the University Library, The University Library’s regulations<sup>2</sup> and in The University’s policy on presentation of Theses.

---

<sup>1</sup><http://www.campus/manchester.ac.uk/medialibrary/policies/intellectual-property.pdf>

<sup>2</sup><http://www.manchester.ac.uk/library/aboutus/regulations>

*For some time he sat gazing  
stupidly at the paper.*

George Orwell, Nineteen  
Eighty-Four, 1949 June

*Anyone who makes graphs in  
Excel isn't a scientist.*

Dr. R. A. Battye, 2010  
September

*Who cares if that someone likes  
the other someone because of  
their race? It's when they hate  
them, that's the problem.*

Orked, Sepet, 2004 February

*Flags are bits of coloured cloth  
that governments use first to  
shrink-wrap people's brains and  
then as ceremonial shrouds to  
bury the dead.*

Arundhati Roy, Come  
September, 2002 September

*Every one of us is, in the cosmic  
perspective, precious. If a human  
disagrees with you, let him live.  
In a hundred billion galaxies, you  
will not find another.*

Carl Sagan, Cosmos, 1980

# Dedication

Ramlah binti Tasrip (1923 – 2013)

# Acknowledgements

To my dear parents, thank you for giving me the freedom to pursue what I wanted. I realise this means that I haven't always been around to help and for that I'm sorry. Maaf zahir dan batin.

Thank you to the menagerie of characters at JBCA who made it a work place like no other. Especially those who brought in cake! Thanks to Fahri Öztürk and Stefania Maccalli: We made it! What would have happened to my sanity if you two weren't around? Thanks to Mareike Haberichter for the late night company in the office and the many laughs that usually happened at your expense. Future TED Talk speaker Peter Schemmel, it's been bewildering and awe inspiring seeing how much one person can manage. Olivia "Libby" Jones for your hyper sociability. Matias Vidal Navarro for your late night falsetto singing in the old West Office. Doctora Lizette Guzman-Ramirez, your accent and personality always made Manchester feel sunny. Amy Tyndall, your long jaunts away from Manchester and the places you got to visit make me regret not doing something more observational. Sean Chapman, I think you had the right idea. Honourable mentions to Ho-Ting "Tony" Fung, Dr. Vic Haynes, Δόκτωρ Foteini "Claire" Lykou, Gülay Gürkan, Rieul Gendron, Dr. Myfanwy Lloyd, Adelaide Ladu and the Cornerhouse.

A non-partisan "Thank you" to all in the various technology groups, teams and cliques for all the knowledge that has been imparted my way over the years.

I am indebted to Uncle er... I mean 博士 Ming Wah "Richard" Ng for your excellent expertise and assistance in the RF lab and the making of the grids. It's safe to say chapters 3 to 5 wouldn't have existed without your help. To SUPERvisor Dottore Giampaolo Pisano: Thank you for all the advice and support you offered. I'll miss our little cultural exchanges. Cheers to Docteur Bruno Maffei for being the sensible one! Many thanks to Dr.'s Anthony Holloway and Bob Dickinson for bearing with our groups many problems and requests with regards to HFSS and its license server.

Thanks to Dr. Mark Purver for the accommodation and all the others who dared

enter: Mohamed Ebadinejad, Andrey Paska, Lingjie Kong, อดิเทพ Phrudth Jaroenjittichai and Melis Irfan. It's been interesting.

To my long lost friends from UG times: the now Dr. Andrew Pollitt and the still Jools Blackburn. I hope you're both doing well.

To almost everyone I had the pleasure of meeting and hitting (and being hit by!) during my time at Kick Start/UWT/"SMART": 詠-what!? 詠春! You all helped me keep my ratio of non-Astrophysicist friends to Astrophysicist friends at a sane level. Also thanks to the good folk I met during my brief stint doing kendo. Kiri-kaeshi is a great stress reliever. 始め!

The author was funded by a studentship from the Science and Technology Facilities Council<sup>3</sup> (STFC). This project made use of Ansys (née Ansoft) HFSS, Mathwork's MATLAB, a Differential Evolution optimisation algorithm written by Markus Buehren<sup>4</sup> and Wolfram's Mathematica. Reference management was carried out with Zotero<sup>5</sup>.

This thesis was typeset with L<sup>A</sup>T<sub>E</sub>X (and a tiny bit of X<sub>Y</sub>L<sup>A</sup>T<sub>E</sub>X) and was based off a template made by Dr. Paul Ruffle (1951–2013). Unless otherwise noted as coming from another source in their captions, all drawings and graphs were respectively made by the author using TikzEdt<sup>6</sup> and PGFPlots<sup>7</sup>. L<sup>A</sup>T<sub>E</sub>X all the things<sup>8</sup>!

---

<sup>3</sup><http://www.stfc.ac.uk>

<sup>4</sup><http://www.mathworks.com/matlabcentral/fileexchange/18593>

<sup>5</sup><https://www.zotero.org/>

<sup>6</sup><http://www.tikzedt.org/>

<sup>7</sup><http://www.ctan.org/tex-archive/graphics/pgf/contrib/pgfplots>

<sup>8</sup><http://knowyourmeme.com/memes/x-all-the-y>

# The Author

The author<sup>9</sup> gained his undergraduate MPhys degree in Physics with Astrophysics from the University of Manchester in 2009. Whilst an undergraduate he partook in a six week summer internship with the Radio Astronomy Technology group in 2008, reverse engineering a Low Noise Amplifier (LNA). After doing an MPhys project in 2009 with the same group he decided to stay and do a PhD. The result of that decision is detailed in this thesis.

---

<sup>9</sup><http://orcid.org/0000-0002-2190-934X>

# Supporting Publications

## Conference Papers

### **Dog Bone Triplet Metamaterial Wave Plate**

I. Mohamed, G. Pisano, M. W. Ng, V. Haynes and B. Maffei (2012). *PIERS 2012 Kuala Lumpur Proceedings*, 1756–1760. Kuala Lumpur, Malaysia, 27th–30th March 2012. The Electromagnetics Academy.

### **A negative refractive index metamaterial wave plate for millimetre wave applications**

I. Mohamed, G. Pisano, M. W. Ng, B. Maffei, V. Haynes and F. Ozturk (2012). *Millimeter, Submillimeter, and Far-Infrared Detectors and Instrumentation for Astronomy VI*, **8452**, 845228. Amsterdam, Netherlands, 1st–7th July 2012. SPIE.

## Refereed Journal Paper

### **W-Band Pancharatnam Half Wave Plate Based on Negative Refractive Index Metamaterials**

I. Mohamed, G. Pisano, M. W. Ng. *Applied Optics*, submitted for publication.

# Acronyms & Initialisms

CAD	Computer Aided Design
CEM	Computational Electromagnetics
CMBR	Cosmic Microwave Background Radiation
CWP	Cut Wire Pair
DBT	Dog Bone Triplet
FDTD	Finite Difference Time Domain
FEM	Finite Element Model
FSS	Frequency Selective Surfaces
HFSS	High Frequency Structure Simulator
HWP	Half Wave Plate
M+S	Master and Slave
MOM	Method of Moments
MUT	Metamaterial/Material Under Test
NRI	Negative Refractive Index
PCB	Printed Circuit Board
PE	Perfect E
PEC	Perfect Electric Conductor
PH	Perfect H
PMC	Perfect Magnetic Conductor
PP	Polypropylene
PRI	Positive Refractive Index
QWP	Quarter Wave Plate
SMA	Submillimeter Array
SRR	Split Ring Resonator
TL	Transmission Line
UV	Ultraviolet
VNA	Vector Network Analyser
ZRI	Zero Refractive Index

# Symbols

$c_0$	Free space velocity of light, $299\,792\,458\text{ m s}^{-1}$
$\delta$	Loss tangent
$\Delta n$	Birefringence
$\Delta\phi$	Phase difference
$\varepsilon_0$	Permittivity of free space, $8.854 \times 10^{-12}\text{ F m}^{-1}$
$\varepsilon_r$	Relative permittivity
$\mu_0$	Permeability of free space, $4\pi \times 10^{-7}\text{ H m}^{-1}$
$\mu_r$	Relative permeability
$n$	Refractive index
$Y$	Admittance of medium, $Y_0 n$
$Y_0$	Admittance of free space, $2.654\text{ mS}$
$Z$	Impedance of medium, $Z_0/n$
$Z_0$	Impedance of free space, $376.7\ \Omega$

# Chapter 1

## Negative Refractive Indices & Metamaterials

*Are you sitting comfortably?  
Then I'll begin.*

Listen with Mother (1950–1982)

### 1.1 Introduction

Where would astronomers or the field of astronomy and astrophysics be today without the invention of telescopes? Such instruments have opened up our horizons from those just on this Pale Blue Dot<sup>1</sup> to those of the observable Universe. The majority of our knowledge about the Universe and its contents has been garnered with telescopes. But telescopes can only be as good as their component parts and the instruments they are connected to (and the people who design and use them). In this thesis the components and instruments will be referred to as “devices” when being spoken of in general. These devices are used to manipulate electromagnetic radiation either by altering its polarisation state (e.g. wave plates), direction of propagation (e.g. lenses and mirrors), splitting it into different components (e.g.

---

<sup>1</sup><http://fettss.arc.nasa.gov/collection/details/the-pale-blue-dot/>

orthomode transducers and diffraction gratings) or just absorbing some of it (e.g. filters and bolometers). These devices, especially those that work optically via interactions with photons, are reliant on the optical properties of the materials they are made from. So for example to manipulate polarisation states, wave plates require birefringent materials that present different optical properties to radiation depending on its incident polarisation state. Lenses require materials that have low reflectivity but also be able to refract radiation.

These two mentioned devices are mainly reliant on a material's optical property known as the refractive index,  $n$ . This is equal to  $n = \pm\sqrt{\epsilon_r\mu_r}$  where  $\epsilon_r$  and  $\mu_r$  are the relative permittivity and permeability of the material. They relate how the material reacts to and how it effects the electric and magnetic components of an electromagnetic field. These material parameters will be described more fully in section 1.2. The materials available to us for device construction are actually limited in regards to their available material properties, especially so in the microwave and terahertz region of electromagnetic spectrum (Peralta et al. 2009; Tao et al. 2010). One such limitation is on the sign of the material property i.e. whether it is positive or negative. For example refractive indices for all known naturally occurring materials and man made compounds are positive and have magnitudes greater than one.

To overcome this limitation, instead of relying on chemical means of creating better compounds and materials, we can use physical means to produce our required material parameters by using "metamaterials". The name metamaterial has become popular in the science community over the past decade, but the idea behind them has been in use since the middle of the 20th century under other names such as Frequency Selective Surfaces (FSS) and metal mesh grids. By creating subwavelength metallic structures we are free to interact with radiation in ways not normally possible. One of these ways is by creating a metamaterial with refractive index of less than zero.

This chapter will start at the small scales by discussing the parameters that

describe electromagnetic radiation's interaction with matter in section 1.2, firstly at the atomic level and moving up in size to bulk materials. Then in section 1.2.3 we move on to describing refraction and how having a negative refractive index effects radiation compared to a positive refractive index. Moving up from bulk materials, a brief history of metamaterials is covered in section 1.4. A description of some types of astronomical instrumentation will be given in section 1.5 and how negative refractive indices may find uses in them. Lastly we finish on the outline of the chapters ahead in this thesis.

## 1.2 Material Parameters

The effect a material has upon electromagnetic radiation can be described via four parameters: the relative permittivity,  $\epsilon_r$ , relative permeability,  $\mu_r$ , refractive index,  $n$ , and the impedance,  $Z$ . The former two are the “canonical” parameters that relate how radiation effects materials (and vice versa) at the atomic level. The latter two are quantities derived from the first two and allow the description of how the bulk behaviour of a material effects radiation. They will now be described in turn.

### 1.2.1 Permittivity

The permittivity of a material defines its response to an electric field which is governed by what occurs at the atomic level of the material. The details are dependent on whether the material is a dielectric or conductor.

In dielectrics the electrons are bound into negatively charged clouds around a central positively charged nucleus. This is shown in figure 1.1a. An oscillating electric field,  $\mathbf{E}(\mathbf{r}, t) = E_0 \exp[i(\omega t - \mathbf{k} \cdot \mathbf{r})]$ , passing through a dielectric will cause the electrons within to experience a driving force,  $-e\mathbf{E}$ , where  $-e$  is the charge of the electron. This acts to displace them from their equilibrium position which has the nucleus at their centre. This is shown in figure 1.1b. The effect of displacing the

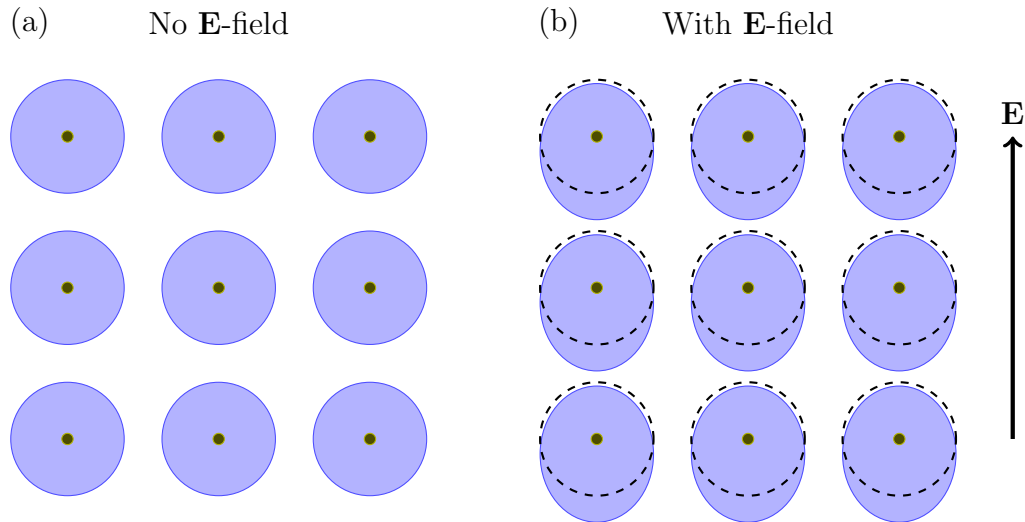


Figure 1.1: The appearance of the electron cloud (blue) surrounding the central nucleus (dark green) (a) with and (b) without an electric field applied. The dashed lines in (b) denote the original position of the electron cloud with no field applied. In this figure a small amount of positive charge now exists on the top and negative charge on the bottom.

electrons with respect to the nucleus (whose position remains relatively unchanged due to its larger mass) is to produce an electric dipole because of the net charge that now exists in the system. The term given to this is polarisation (*not* to be confused with the polarisation of the electric field). The amount of polarisation,  $\mathbf{P}$ , experienced is related to the permittivity by

$$\mathbf{P}(t) = \varepsilon_0(\varepsilon_r(\omega) - 1)\mathbf{E}(\mathbf{r}, t) \quad (1.1)$$

where  $\varepsilon_0$  is the permittivity of free space ( $8.854 \times 10^{-12} \text{ F m}^{-1}$ ). The electrons, being bound, feel a position dependent restoring force,  $-\alpha\mathbf{r}$ , that acts to return the electron to its equilibrium position, as well as a velocity dependent damping term,  $\beta\dot{\mathbf{r}}$ , arising from the resistance to the radiation. Putting this all together using Newton's Second Law of Motion we obtain

$$m_e\ddot{\mathbf{r}} = -e\mathbf{E}_0 \exp[i\omega t] - \alpha\mathbf{r} - \beta\dot{\mathbf{r}} \quad (1.2)$$

where  $m_e$  is the electron's mass. This is a damped harmonic oscillator, the solution to which is

$$\mathbf{r}(t) = \mathbf{r}_0 \exp[i\omega t] = \frac{-(e/m_e)\mathbf{E}_0}{(\omega_0^2 - \omega^2) + i\omega\gamma} \exp[i\omega t] \quad (1.3)$$

where  $\mathbf{r}_0$  is the displacement of the electron cloud's centre,  $\omega_0^2 = \alpha/m_e$  and  $\gamma = \beta/m_e$ . The polarisation  $\mathbf{P}(t)$  from equation (1.1) is also equal to the summation of the individual electric dipole moments,  $\mathbf{p} = -e\mathbf{r}_0$ , of the charges in the material. If we assume that each dipole is the same, then for  $N$  electrons we have

$$\mathbf{P}(t) = -N e \mathbf{r}_0. \quad (1.4)$$

Substituting equation (1.3) into equation (1.4) and equating the result with equation (1.1) we find that

$$\varepsilon_r(\omega) = 1 + \frac{\omega_p^2}{(\omega_0^2 - \omega^2) + i\omega\gamma} \quad (1.5)$$

where  $\omega_p$  is the plasma frequency and is given by

$$\omega_p^2 = \frac{Ne^2}{\varepsilon_0 m_e}. \quad (1.6)$$

A similar result to equation (1.5) can be reached for conductors by assuming that its constituents behave as a plasma with free electrons and fixed positive ions. The differences are that 1) the electrons are unbounded so there is no restoring force and hence no  $\omega_0$  appears in the final equation and 2) the damping term  $\gamma$  is the result of electrons colliding with the positive ions. This results in

$$\varepsilon_r(\omega) = 1 - \frac{\omega_p^2}{\omega(\omega + i\gamma)}. \quad (1.7)$$

### 1.2.2 Permeability

In the same way that permittivity arose from the electric dipoles reacting to an incident electric field, permeability arises from magnetic dipoles reacting to magnetic fields. An electron orbiting a nucleus forms a current loop and as a result produces a magnetic dipole moment,  $\mathbf{m} = e\mathbf{J}/2m_e$  where  $\mathbf{J}$  is the electron's angular momentum. What happens when a magnetic field is applied is dependent on whether the material is diamagnetic, paramagnetic or ferromagnetic. For diamagnetic materials the constituent atoms have paired electrons, the magnetic dipole moment of which is about zero. When a magnetic field is applied, the electron's orbital velocity changes, altering the orbital angular momentum. This produces a magnetic dipole moment that acts to counter the applied magnetic field. This counteraction occurs with the dipole precessing about the direction of the magnetic field. In paramagnetic and ferromagnetic materials there is an unpaired electron in the atomic shell and this results in there being a non-zero magnetic dipole moment which aligns *with* the applied magnetic field. Similar equations to equations (1.5) and (1.7) can be obtained that relates the permeability to  $\omega$ . From Engheta and Ziolkowski (2005) we have

$$\mu(\omega) = 1 - \frac{\omega_{\text{mp}}^2}{\omega(\omega + i\gamma_{\text{m}})} \quad (1.8)$$

where  $\omega_{\text{mp}}$  and  $\gamma_{\text{m}}$  are respectively the magnetic equivalents to the plasma frequency and damping term from the permittivity equations in section 1.2.1.

### 1.2.3 Refractive Index & Impedance

To describe the behaviour of electromagnetic radiation in media, the relative permittivity and relative permeability are often combined into two other values: the refractive index,  $n$ , and impedance,  $Z$ , which are respectively given by

$$n = \pm\sqrt{\epsilon_r\mu_r} \quad \text{and} \quad (1.9)$$

$$Z = \sqrt{\frac{\mu_0 \mu_r}{\epsilon_0 \epsilon_r}}. \quad (1.10)$$

The refractive index gives the ratio between the speed of radiation in free space,  $c_0$ , and its speed within a medium such that  $n = c_0/v$ . It is most commonly known for its use in Snell's Law (equation (1.15)) to calculate angles of refraction when radiation passes between two media. In optics it also finds use in calculating a field's reflected,  $\rho$ , and transmitted,  $\tau$ , amplitudes when it passes between media. Collectively they are known as Fresnel's equations and are usually given in optics text books e.g. Longhurst (1986) and Orfanidis (2010) as

$$\rho = \frac{n_1 - n_2}{n_1 + n_2} \quad \text{and} \quad (1.11)$$

$$\tau = \frac{2n_1}{n_1 + n_2} \quad (1.12)$$

where  $n_{1,2}$  refer to the refractive indices of the two media involved. This form is only true for non-magnetic materials where  $\mu_r = 1$  and when radiation is incident perpendicularly to the interface between the media. Generally, where  $\mu_r \neq 1$ , we must use the impedances,  $Z_1$  and  $Z_2$ , of the media instead giving

$$\rho = \frac{Z_2 - Z_1}{Z_2 + Z_1} \quad \text{and} \quad (1.13)$$

$$\tau = \frac{2Z_2}{Z_2 + Z_1} \quad (1.14)$$

An even more general form of equation (1.13) that allows for non-perpendicular incident angles is shown in equation (1.20) on page 43. Together these two values are more commonly used to describe the macroscopic behaviour of the interaction between radiation and materials.

## 1.3 Negative Refractive Indices

All known naturally occurring or man made materials have a positive refractive index (PRI). Negative refractive indices (NRI) are not known to exist in nature. To do so requires a material to simultaneously have a negative  $\varepsilon_r$  and negative  $\mu_r$  in the same frequency range. In nature, only single negative values are achieved i.e. either one of  $\varepsilon_r$  or  $\mu_r$  is negative whilst the other is positive.

Although discussed prior to 1968 by the likes of Schuster (1904) for example, the widely cited Veselago (1968) has become the canon paper for discussing the consequences of radiation interacting with a medium with simultaneously negative values of  $\varepsilon_r$  and  $\mu_r$ . Veselago noted that if such a material existed then the negative root of equation (1.9) should be taken. At first this may seem counter intuitive. The product of two negative numbers is positive, so why would their individual signs effect the sign of the square root taken in equation (1.9)? Ziolkowski and Heyman (2001) and Pendry (2004) made arguments based on causality. Assuming an  $\exp(i\omega t)$  time dependence for radiation, real materials have  $\text{Im}(\varepsilon_r) < 0$  and  $\text{Im}(\mu_r) < 0$  representing their absorptive behaviour. When  $\text{Re}(\varepsilon_r) < 0$  and  $\text{Re}(\mu_r) < 0$ , the negative root must be taken to ensure the correct sign of the imaginary components as well as the analytical continuity of the real components.

The results from this paper remained a mere curiosity for the majority of the 20th century until Pendry (2000) was published where upon a new branch of research began. Some of the phenomena predicted by these two papers are briefly described below.

### 1.3.1 Negative Refraction

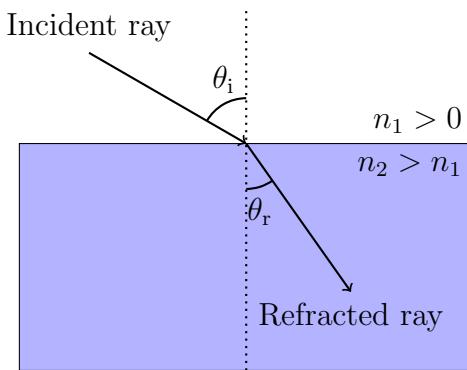
The refraction of radiation as it crosses the boundary of two media has been well known for more than a millennium, with the earliest correct mathematical description written in 984 by Ibn Sahl (Rashed 1990). This mathematical description,

now commonly referred to as Snell's Law (after Willebrord Snellius, who derived the law more than 600 years after Ibn Sahl) is

$$n_1 \sin \theta_i = n_2 \sin \theta_r \quad (1.15)$$

where  $n_{1,2}$  refer to the refractive indices of the two media present and  $\theta_{i,r}$  are the angles of the incident and refracted radiations to the normal of the interface between the two media. It follows from equation (1.15) that when one medium has a negative value of  $n$  the angle by which a light ray is refracted occurs on the opposite side of the normal (figure 1.2).

(a) Positive refraction:



(b) Negative refraction:

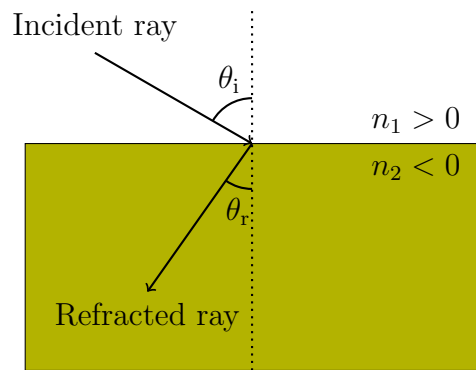


Figure 1.2: Light rays undergoing (a) positive and (b) negative refraction.

This results in the role of convex and concave lenses becoming reversed such that convex lenses will cause radiation to diverge and concave lenses will cause radiation to converge. From a lens manufacturing stand point this is an interesting proposition because with a concave shaped lens the majority of the mass is located near the circumference where lenses are held. Such a configuration is advantageous as it can reduce the amount of sagging that occurs for large lenses.

A more interesting effect is observed when a flat block of NRI material is used. As shown in figure 1.3(b) a flat block with a negative refractive index can bring diverging light rays to a focus. The location of the focal point on the other side of the block is equal to  $d_2 = 2d - d_1$  if  $n = -1$  as it is in figure 1.3(b). It should be

noted that only diverging rays can be brought to a focus, unlike a regular PRI convex lens that can handle parallel rays too, and so cannot strictly be considered a lens.

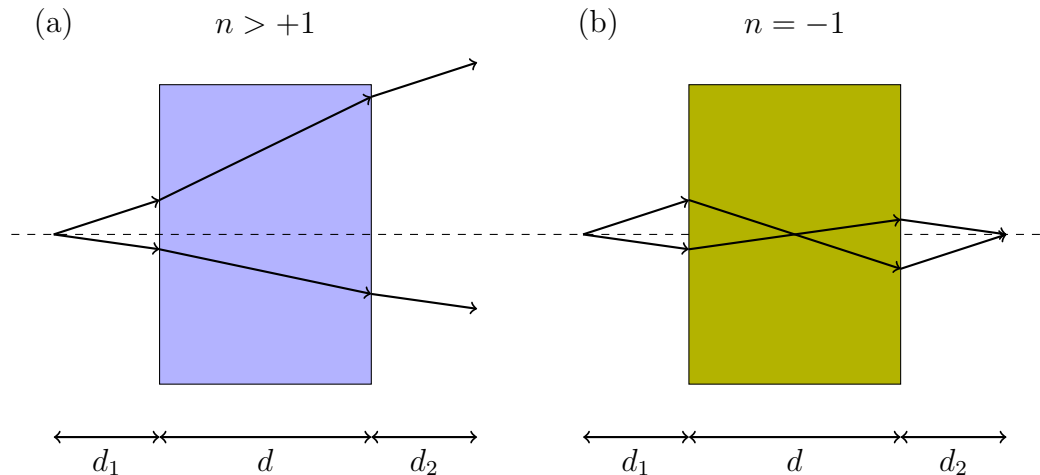


Figure 1.3: (a) A block with refractive index  $> 1$ . Light rays pass through the block and continue on their divergent path. (b) The block with refractive index,  $-1$ , is able to bring the diverging rays to a focus twice, once within the block and once again when the rays exit.

### 1.3.2 Superlensing

Staying with the flat slab example from the end of section 1.3.1, the key result presented in Pendry (2000) was that in addition to allowing a flat slab to bring two diverging rays to a focus, a slab with a negative refractive index would also allow the resolving images beyond the diffraction limit.

To see where this limitation in resolving power arises, Ramakrishna (2005) pictures a flat surface scattering incoming radiation on a plane  $z = 0$  (figure 1.4). The associated electric field takes the form  $E(x, y, 0)$ . The fields over all space can then be written down as

$$\mathbf{E}(x, y, z, t) = \left(\frac{1}{2\pi}\right)^2 \int_{k_x} \int_{k_y} dk_x dk_y F(k_x, k_y) \exp[i(k_x x + k_y y + k_z z - \omega t)] \quad (1.16)$$

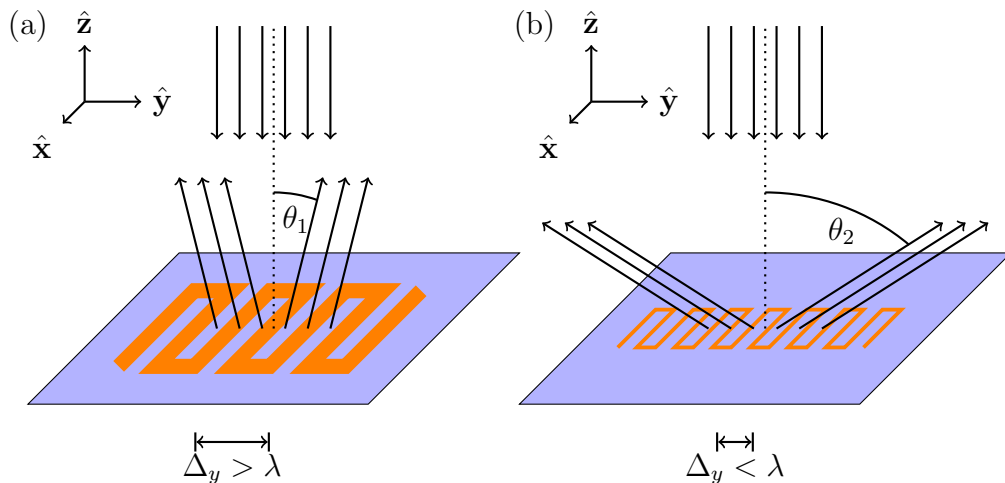


Figure 1.4: Two different surfaces in the plane  $z = 0$  with incident radiation travelling in the  $-z$  direction. The surface (a) contains a feature with a large physical size ( $\Delta_y > \lambda$ ) whilst (b) contains a feature with a smaller physical size ( $\Delta_y < \lambda$ ). Incident radiation is scattered in (a) through relatively shallow angles, whilst in (b) the angle is much greater. Drawing based on Ramakrishna (2005, figure 24).

where  $\omega$  is the  $2\pi$  times the frequency of the radiation and

$$F(k_x, k_y) = \int_x \int_y dx dy \mathbf{E}(x, y, 0) \exp[-i(k_x x + k_y y)] \quad (1.17)$$

is the Fourier transform of the surface's spatial variation. From Maxwell's equations we know

$$k_z = +\sqrt{k_0^2 - k_x^2 - k_y^2} \quad (1.18)$$

where  $k_0 = \omega/c_0 = 2\pi/\lambda$  and  $k_{x,y}$  represent the Fourier components of the spatial variation in the  $x$ - and  $y$ -directions and  $\lambda$  is the wavelength of the radiation. They are related to the physical size of the spatial variations  $\Delta_{x,y}$  by  $\Delta_{x,y} = 2\pi/k_{x,y}$ . To allow wave propagation in the  $z$ -direction,  $k_z$  must have a real value, hence requiring that  $k_0^2 > k_x^2 + k_y^2$ . This is seen in figure 1.4a where the radiation is scattered through a small angle,  $\theta_1$ , because  $k_y < k_0$  or equivalently,  $\Delta_y > \lambda$ . So to have a propagating wave, the wave may only carry information about structures larger than the wavelength of the radiation. Structures smaller than  $\lambda$  implies

1: NEGATIVE REFRACTIVE INDICES & METAMATERIALS

$k_x^2 + k_y^2 > k_0^2$  and as seen in figure 1.4b results in radiation being scattered through a much larger angle,  $\theta_2$ . Inserting values of  $k_{x,y}^2 > k_0^2$  into equation (1.18), results in  $k_z$  taking an imaginary value. Such a wave no longer represents a propagating wave, but instead an evanescent wave whose amplitude exponentially decays as it propagates away from its source. Information carried about spatial variations smaller than  $2\pi/k_0$  or  $\lambda$  is lost once the evanescent wave's amplitude has decayed away.

Pendry noticed that a slab of material that had a  $\epsilon_r$  and  $\mu_r$  of  $-1$  (or indeed any negative value), the evanescent waves would increase in amplitude as it travelled through the slab.

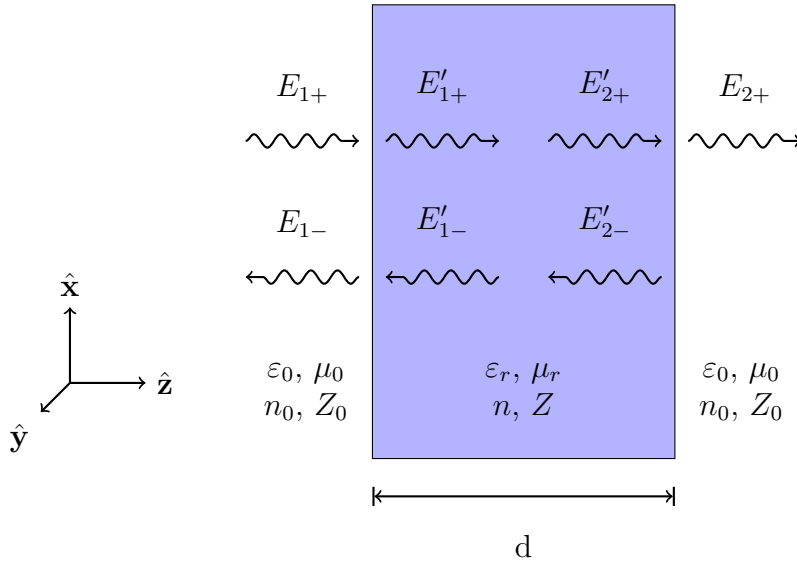


Figure 1.5: Diagram showing the backward and forward  $E$ -fields of radiation incident on the left hand side of the slab and the resulting reflected and transmitted radiation field components.

To demonstrate this, take a wave with  $\exp(-i\omega t)$  time dependence travelling in free space in the  $z$ -direction and let it be incident on a slab of thickness,  $d$ , relative permittivity,  $\epsilon_r$ , and relative permeability,  $\mu_r$ , and hence refractive index,  $n$ , and impedance,  $Z = (\mu_r\mu_0)/(\epsilon_r\epsilon_0)$  as shown in figure 1.5.  $E_+$  and  $E_-$  are the amplitudes of the  $E$ -fields travelling in the forward and backward directions respectively i.e.  $E_0 \exp(+ikz)$  and  $E_0 \exp(-ikz)$ . Using the matching

and propagation matrices that will be explained further in section 2.3, the total reflected and transmitted amplitudes of the  $E$ -fields radiation can be derived giving

$$R = \frac{E_{1-}}{E_{1+}} = \frac{\rho [1 - \exp(-i2k_0nd)]}{1 - \rho^2 \exp(-i2k_0nd)} \quad \text{and} \quad (1.19a)$$

$$T = \frac{E_{2+}}{E_{1+}} = \frac{(1 - \rho^2) \exp(-ik_0nd)}{1 - \rho^2 \exp(-i2k_0nd)} \quad (1.19b)$$

respectively. The Fresnel reflection coefficient,  $\rho$ , is dependent on whether the wave is TE-polarised (s-polarised), with the  $E$ -field orientated along the  $y$ -axis, or TM-polarised (p-polarised), with the  $E$ -field orientated along the  $x$ -axis:

$$\rho = \begin{cases} \frac{Z \cos \theta_i - Z_0 \cos \theta_r}{Z \cos \theta_i + Z_0 \cos \theta_r}, & \text{TE polarisation} \\ \frac{Z \cos \theta_r - Z_0 \cos \theta_i}{Z \cos \theta_r + Z_0 \cos \theta_i}, & \text{TM polarisation.} \end{cases} \quad (1.20a)$$

$$(1.20b)$$

If the slab has  $\varepsilon_r = \mu_r = -1$  and hence  $n = -1$  and  $Z = Z_0$  it can be seen from equation (1.20) that in both TE and TM cases,  $\rho = 0$  resulting in  $R = 0$  and  $T = \exp(-ik_0nd)$  i.e. perfect transmission and is applicable with any incident angle,  $\theta_i$ .

To show that evanescent waves are recovered in addition to the regular propagating waves, we make the substitution  $\cos \theta = k_z/k$  and noting that  $k = nk_0 = n\omega/c_0$  we can recast equation (1.20) as

$$\rho = \begin{cases} \frac{k_z \mu_r - k'_z}{k_z \mu_r + k'_z}, & \text{TE polarisation} \\ \frac{k_z \varepsilon_r - k'_z}{k_z \varepsilon_r + k'_z}, & \text{TM polarisation.} \end{cases} \quad (1.21a)$$

$$(1.21b)$$

An incoming evanescent wave would have a  $k_z$  of  $i\sqrt{k_x^2 + k_y^2 - k_0^2}$ . Note the imaginary number,  $i$ , causes the exponential component of the wave to be real and negative, creating the evanescent wave's exponential decay. Once within the slab,  $k'_z$  takes the form  $i\sqrt{k_x^2 + k_y^2 - (nk_0)^2}$ . Substituting these into equations (1.19)

both result in  $R = 0$  and  $T = \exp(-ik_0nd)$ .

These calculations show that for both propagating and evanescent waves, the transmitted wave has the same amplitude as the incident wave. The remarkable result is that a slab of refractive index,  $n = -1$ , is capable of reversing the decay of the evanescent wave. With all the wave components  $k_{x,y} > 0$  and  $k_{x,y} < 0$  being restored, a perfect image of the source is created.

### 1.3.3 Backward Waves

Solving Maxwell's equations for a planar wave gives the solutions  $\mathbf{k} \times \mathbf{E} = \omega\mu_0\mu_r\mathbf{H}$  and  $\mathbf{k} \times \mathbf{H} = -\omega\varepsilon_0\varepsilon_r\mathbf{E}$  where  $\mathbf{k}$  is the wave propagation direction,  $\mathbf{E}$  the electric field component and  $\mathbf{H}$  the magnetic field component. In a PRI medium these equations form a right-handed triad. However, if the values of  $\varepsilon_r$  and  $\mu_r$  are negative the resulting triad becomes left-handed. This provides the origins of the term "Left-Handed Materials" used by some authors when referring to NRI materials. In contrast the Poynting vector,  $\mathbf{S} = \mathbf{E} \times \mathbf{H}$ , which defines the energy flux of an electromagnetic wave travelling in the direction  $\mathbf{E} \times \mathbf{H}$  remains the same regardless of whether the material has a positive or negative refractive index.

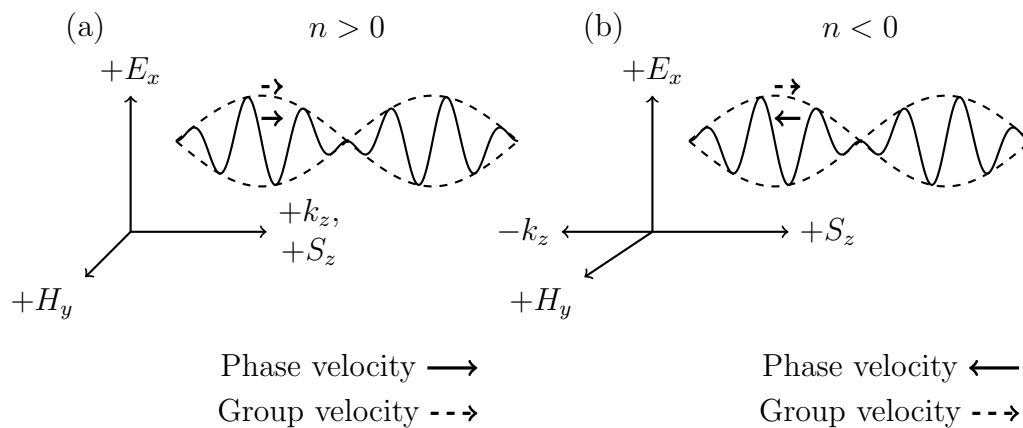


Figure 1.6: Diagram showing the motions of a wave packet's different components within a medium with (a) a positive refractive index and (b) a negative refractive index. The solid line represents the wave, whilst the dashed line serves to outline the wave's envelope.

Physically, this means that within a NRI medium, energy flow of an electromagnetic wave given by the group velocity is in the direction away from the source as expected but the oscillations of the wave itself travel in the opposite direction toward the source at the phase velocity (figure 1.6).

## 1.4 A Brief History of Negative Refractive Index Metamaterials

A number of definitions for metamaterials exist in the scientific community. In this thesis they are defined as being a repeated array of subwavelength structures, referred to as “unit cells”, that are able to interact with electromagnetic radiation. Metamaterials that work with other types of wave behaviour e.g. acoustic and seismic were not covered in this project (but they are interesting in their own right). The requirement for the unit cells to be subwavelength in size is important. When radiation passes by a metamaterial’s unit cell that is smaller than its wavelength the radiation doesn’t “see” its individual components. Instead it feels the average effect of the repeated unit cells. This is akin to radiation not “seeing” individual electrons in a material but feeling the average effect of their charge distribution around an atom or molecule.

In the literature, the history and creation of NRI metamaterials is generally begun and attributed to two or three papers: Veselago (1968) for coming up with the idea of negative refractive indices, Pendry (2000) for popularising NRI and Smith et al. (2000) for the first experimental verification of NRI behaviour using metamaterials. The history of manipulating radiation with subwavelength metallic structures however can actually be brought back further to the 1960’s when the microwave engineering community were using metallic meshes and FSS as filters and polarisation controllers for radiation (Marcuvitz 1965; Ulrich 1967).

The precursors to the first NRI metamaterial were Pendry et al. (1996, 1998) that used a wire grid to create a negative permittivity and Pendry et al. (1999)

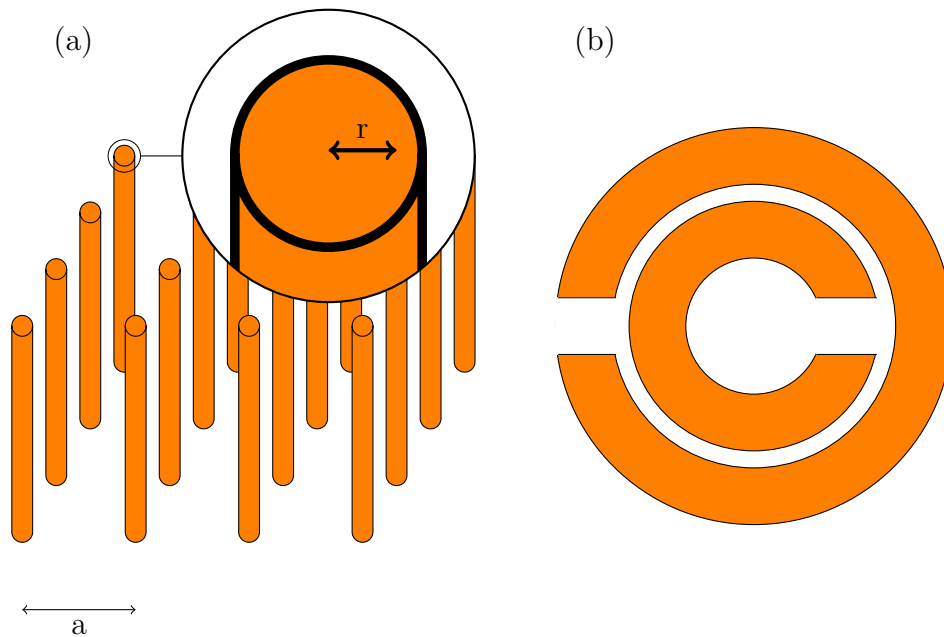


Figure 1.7: (a) The wire grid structure used to create negative permittivity in the GHz frequency range. Drawing is based on Pendry et al. (1999, figure 3). (b) Face on view of a single split ring resonator used to produce a negative permeability. Drawing based on Pendry et al. (1999, figure 12).

that used split-ring resonators (SRRs) to produce a negative permeability. The structures are shown in figure 1.7.

From equation (1.7) we can see that if radiation's frequency,  $\omega$ , is lower than the plasma frequency,  $\omega_p$ , a negative permittivity exists when losses are minimal. For conductors this is easily achievable with ultraviolet radiation. But as the frequency approaches the infrared part of the spectrum the dissipation term,  $\gamma$ , increases and prevents negative permittivity being observed at radio frequencies. So to produce a negative permittivity, Pendry et al. (1996, 1998) devised a way to mimic the behaviour of a low density plasma using periodically aligned arrays of thin wires (figure 1.7a) of radius,  $r$ , separated by a distance,  $a$ . Both of these values were less than  $\lambda$ , the operating wavelength. The wires both restricted the movement of the electrons and increased the electrons' effective masses. By restricting their movements, the electron number density within a volume is lowered. The increase in effective mass results from the difficulty in altering the current flow within

the wires due to the wires large inductance. Taking these effects into account in equation (1.6), we see that the effective plasma frequency of the wire array is lowered. In Pendry et al. (1996)'s case, into the GHz range.

Just as before, a negative permeability can exist if the frequency of radiation is below the materials magnetic plasma frequency,  $\omega_{mp}$  (equation (1.8)). With the aim of producing a magnetic equivalent of the aforementioned wire arrays Pendry et al. (1999) came up with split ring resonators that could produce magnetic response in the radio regime. Consisting of two concentric rings with a split in them, as shown in figure 1.7b, when a magnetic field perpendicular to the rings passes through the rings' holes, a current is induced in them. The splits prevent the current going around the rings and instead causes charge build up at the two ends of the split, creating behaviour akin to a capacitor. Together with the rings' inductance, a resonant LC-circuit is produced. Radiation of a frequency close to that of the SRRs resonant frequency, will produce a negative permeability.

By altering the dimensions of the wire grid and SRR structures so that respectively, their negative  $\epsilon_r$  and negative  $\mu_r$  regions overlapped in the same frequency range and combining these two structures (figure 1.8), experimental verification of negative refractive indices were demonstrated in Smith et al. (2000) and Shelby et al. (2001b).

To use the SRR and wire design to build large optical instruments is not practical however. The first issue arises when the SRR is reduced in size to function in the  $\sim 100$  THz frequency range and higher. Shrinking the dimensions reduces the strength of the magnetic resonance which in turn adversely effects the NRI properties of the metamaterial. The sizes required to function at  $\gtrsim 100$  THz means the metal used to create the SRR ceases to behave as an ideal conductor (Zhou et al. 2005; Soukoulis et al. 2007). The second issue comes from manufacturing difficulties arising from how the SRR functions. To create a negative  $\mu_r$  the magnetic field must pass through the ring. For this condition to be met, radiation must propagate parallel to the SRRs surface. So to create a three dimensional slab



Figure 1.8: A close up the split ring resonator and wire structure used in Shelby et al. (2001b) to demonstrate negative refractive indices. The SRR and wires were printed on opposite sides of the same substrate and together were capable of creating a negative index band for radiation with its  $E$ -field aligned with the wires. To provide a sense of scale the size of the SRRs is 5 mm. Photo taken from Shelby et al. (2001b, figure 1). Reprinted with permission from AAAS.

from the two dimensional sheets fabricated via photolithography (see section 3.2.1) the sheets must be cut into strips that then need to be manually slotted together in some way to form an interlocking lattice, as shown in figure 1.8.

The solution to these problems came via the use of what is sometimes referred to as “planar” metamaterials. Like the SRR and Wire metamaterial design, they consisted of metallic components placed onto the surface of a dielectric. Unlike the SRR and Wire design, but like the previously existing FSS and metal mesh grids, they were designed to work with radiation passing perpendicularly to its surface. They were made by closely pairing up the metallic grids (separations  $\ll \lambda$ ) with a substrate sandwiched between the two (figure 1.9). Like the SRR and wires design, the electric response arises from the interaction of the  $E$ -field with the metallic components. Unlike the SRR and Wire designs, the planar designs could recreate a magnetic response when radiation was incident perpendicular to its surface. The electric component of the incident radiation induces anti-parallel currents in the two metallic parts. The displacement current that passes through the substrate then completes the current loop and allows the production of the

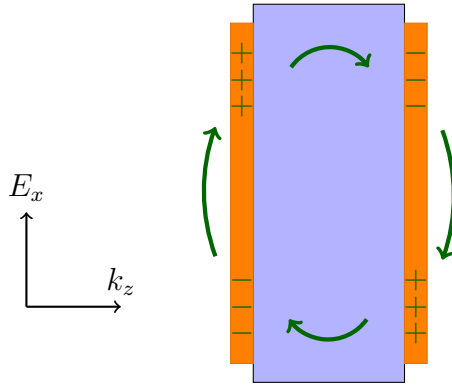


Figure 1.9: A side on view of a single planar metamaterial cell, with the metallic parts coloured orange and the substrate coloured blue. The  $E$ -field of radiation propagating to the right induces anti-parallel currents in the copper components. These currents in turn produce a current loop (green arrows) that then produces a magnetic response causing  $\mu_r \neq 1$ .

magnetic response (figure 1.9).

Planar designs for NRI metamaterials began appearing in the literature from 2005 onwards starting with Zhang et al. (2005) and Shalaev et al. (2005) who both utilised a cut wire pair (CWP) geometry (figure 1.10a) to create NRI in the near infrared regime. Since then, a plethora of different geometries, some shown in figure 1.10, have been reported. Designs such as the CWP and SRR are polarisation dependent, only capable of producing a negative refractive index band for one polarisation. Others such as those based on crosses are able to work for any polarisation angle and incident angle. Additional metallic components can be added to these crosses such as bars (figure 1.10b) or circles (figure 1.10f) to alter the base shapes behaviour by adding additional degrees of freedom to manipulate. In the case of the Jerusalem Cross Pair (JCP), the addition of the bars allowed the capacitance between the neighbouring unit cells to be controlled and hence control the resonant frequency (Vallecchi et al. 2009; Vallecchi and Capolino 2009). Adding circles or squares to the intersections of a fishnet type geometry allowed control of the impedance matching to its environment (Zaoui et al. 2012).

Although originally conceived in the radio frequencies,  $\sim 1$  GHz ( $\sim 30$  cm), the

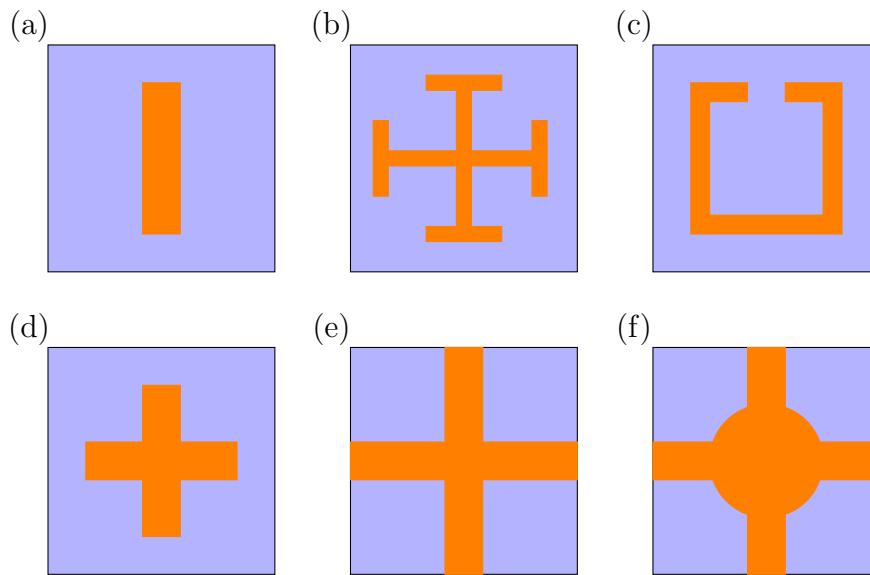


Figure 1.10: Face on view of some of the many unit cell designs used in the literature to produce negative refractive indices. These designs are repeated to form two dimensional arrays. The side on view of all of these would look like figure 1.9. Metallic components are coloured orange. Substrate is coloured blue. (a) Cut wire pair (CWP). (b) Jerusalem cross pair (JCP). (c) Split ring resonator (SRR). (d) Cross. (e) Fishnet. (f) Alternative fishnet.

march of technology has allowed the creation of smaller and smaller metamaterial unit cells, allowing negative refractive indices to be observed at ever increasing frequencies. From examples in the visible,  $\sim 500$  THz ( $\sim 600$  nm), demonstrated by Tang and He (2010) to even ultraviolet frequencies,  $\sim 800$  THz ( $\sim 360$  nm), recently shown by Xu et al. (2013).

## 1.5 A Role for NRI Metamaterials in Astronomical Instrumentation

As stated in Tao et al. (2010), how radiation is manipulated and controlled is dependent on its frequency. In the infrared part of the spectrum, radiation manipulation is done via photon based interactions using optical components such as mirrors and lenses. Electron based interactions form the basis of components such

as waveguides and microstrip which are more commonly used at radio frequencies. Between the two regimes lies the terahertz (mm and sub-mm wavelength) region of the spectrum that extends from 100 GHz to 10 THz. In this region the efficiency of either method tapers off (Tao et al. 2010). Even outside of the terahertz region, there are few suitable materials to use to create optical devices such as lenses and wave plates. Metamaterials, with their ability to have tailored electromagnetic responses allows them to be used in place of regular materials such as high-density polyethylene (HDPE) or sapphire. In this way they can be seen as artificial dielectrics.

Given that a large amount of NRI metamaterial research has been carried out in the radio and microwave frequencies, it seems only natural to think of ways they could be applied to existing instrumentation used in radio and microwave astronomy. Here we will look at two examples of instruments and devices used in astronomical instrumentation and propose how negative refractive indices may be applied.

### 1.5.1 Lenses

Much like their visible spectrum counterparts, lenses in the radio frequencies are also used to focus radiation. They can be found placed in front of horn antennas, reducing the size of the antenna's side lobes and increasing their directivity. This allows for a greater amount of signal to be detected from the region of sky that the horn antenna is pointing toward. Lenses are generally made out of dielectric materials such as HDPE or silicon and are milled into their required shape. There are applications needing lenses able to create highly convergent beams. These require the lenses to have a short focal lengths (Pisano et al. 2013). This can be achieved in one of two ways: 1) Use of a low refractive index material (e.g. HDPE) to create a thick, highly curved lens, or 2) Use of a high refractive index material (e.g. silicon) to create a thinner lens that requires the application of an antireflective coating to improve the impedance matching between it and its

surrounding environment to reduce reflections. In cases where large diameter lenses ( $\gtrsim 50$  cm) are required to cover an array of horns, such lenses made from these dielectric materials can become unwieldy to handle and manufacture. In the case of the low refractive index materials, physical deformation can become an issue if made too thick (as noted in section 1.3.1).

How might NRI be useful here? Whilst the thought of using the superlens of section 1.3.2 to produce unprecedented high resolution images of the cosmos is tempting, such enthusiasm must be curbed. The ability of an NRI material to produce a superlens that can beat the diffraction limit is dependent on it being able to amplify the evanescent waves from the radiation's source. But because the amplitude of these evanescent waves decays exponentially from their source and astronomical sources are such a vast distance away, there is practically no evanescent field left to amplify.

However, there is still an advantage for using NRI lenses. Aside from the diffraction limit, PRI lenses are subject to physical imperfections, that for monochromatic radiation can be described by five quantities: spherical aberration, coma, astigmatism, field curvature and distortion. Collectively these are referred to as Seidel aberrations. Theoretical work by Schurig and Smith (2004) and Zhi-Li et al. (2008), has suggested the use of NRI lens can aid in removing a number of these aberrations. When using only PRI lenses, a suite of them must be used to correct for all five of them. With only a single NRI lens, Schurig and Smith (2004) showed that all but one aberration can be corrected for. With two lenses in either a PRI-NRI or NRI-NRI setup, Zhi-Li et al. (2008) claimed that all five could be corrected, causing the authors to suggest that such a setup would be the best for use in far field imaging situations such as astronomy.

## 1.5.2 Wave Plates

A more in depth analysis of wave plates and birefringences will be given in chapter 5, but briefly wave plates are devices used to modulate the polarisation

of the radiation transmitted through it. By rotating them in front of a suitable detector different types of polarisations can be detected and their signals distinguished from unpolarised radiation which may be stronger in magnitude than the polarised signals. Wave plates work by imparting a differential phase shift between the orthogonal axes of incident radiation's  $E$ -field. The value of this phase shift is proportional to the difference in the refractive index values,  $n_x$  and  $n_y$ , along its axes and the wave plates thickness.

Regular birefringent materials used in the radio frequencies include sapphire and quartz tend to have low birefringences,  $\Delta n = n_x - n_y = 0.1$ . So to impart any meaningful differential phase shift (either  $90^\circ$  or  $180^\circ$ ) requires thick samples of sapphire or quartz. With a shortage of high birefringent materials in the radio frequencies, we can instead use highly birefringent metamaterials that have NRI in one axis and PRI in the other, hence allowing for  $\Delta n \gtrsim 1$ .

The advantages of thinner wave plates are the same as those for thinner lenses in that they are easier to handle, less massive, less susceptible to deforming under their own weight and less absorbing. Also, certain future astronomical experiments (e.g. those looking for polarisation in the cosmic microwave background radiation (CMBR)) will require wave plates in excess of 50 cm in diameter. To continue using materials such as sapphire at these sizes would become problematic from a manufacturing point of view because they are only available in diameters up to  $\sim 30$  cm. So here once again, metamaterials (in general this time, not just those exhibiting NRI) have an advantage in that the upper limit on their diameter is restricted by the available manufacturing equipment. Lastly, thinner plates are less likely to cause a problem known as cross polarisation.

## 1.6 Thesis Outline

The aims of this thesis are to study whether using negative refractive index metamaterials in mm-wavelength astronomical instrumentation has any advantage

over current systems. As described previously, negative refractive indices provide some promising benefits which are worthy of investigation.

Chapter 2 will describe the finite element modelling software used to draw, design and simulate metamaterial unit cells. How the software does its simulations will also be covered as well as some of its features that were used during this project. Then a transmission line based code based on a matrix formalism that was used to model devices made from a cascade of unit cells will be described.

Chapter 3 will go into the details of how the grids that make up the metamaterials used during this project were manufactured using the process of photolithography. The process of the alignment and hot pressing of those grids to form larger devices is then covered.

Chapter 4 will describe the creation of an artificial dielectric slab with a refractive index of  $n = -1$ . It begins with the derivation and testing of a parameter extraction method that will allow the refractive index (and the other three material parameters) to be calculated from just the reflection and transmission readings. Then it moves onto the design and manufacturing stage of the NRI slab. Comparisons between experimental data and simulation are given. Difficulties encountered during the various stages and how they were overcome are also given.

Chapter 5 will go into a description of birefringent materials and how they are used to create wave plates. A brief survey on how the simultaneous use of negative and positive refractive indices can be used to create highly birefringent metamaterials. Two types of wave plates are designed, modelled, manufactured and experimentally tested: An air gap half wave plate and a quarter wave plate embedded within polypropylene. The modelled and experimental data are compared.

Finally the conclusions are presented in chapter 6, where a summary of its preceding chapters will be given and later the final conclusions. Suggestions for possible avenues for further work are also provided.

# Chapter 2

## Designing Metamaterials

*The probability of success is difficult to estimate; but if we never search, the chance of success is zero.*

Giuseppe Cocconi & Philip Morrison, 1959 September

### 2.1 Introduction

Before a device (e.g. lens or wave plate) could be built, the metamaterial unit cell it would be made from must be designed and optimised. This could be done by studying a single isolated unit cell from the periodic array that will make up the final device. Similarly the device itself must be designed and optimised afterwards. These design and optimisation steps required the use of computational tools and it is these tools that are the subject of this chapter.

Firstly, a description of a commercial software implementation of the Finite Element Method (FEM) is given. Details of how the software works and how it is used to model single unit cells will be provided. Later, an improved version of the Transmission Line (TL) model used to model and optimise devices made from a cascade of metamaterials will be explained. Finally a comparison between the two

different methods will be given.

## 2.2 Finite Element Method Modelling & HFSS

In the field of Computational Electromagnetics (CEM), different methods have been developed to model the behaviour of electromagnetic radiation when it is in the presence of complex structures made from different media. The most widely used (Davidson 2011) include the Finite Difference Time Domain (FDTD) method, the Method of Moments (MOM) and the Finite Element Method (FEM). In this project the latter method was used with the aid of a commercial three-dimensional electromagnetic full wave solver, HFSS<sup>1</sup> (High Frequency Structure Simulator), by Ansys (formerly Ansoft).

### 2.2.1 Designing & Drawing

The design process begins by selecting a suitable metamaterial unit cell from the existing literature. It is then scaled to work within the frequency range of interest for this project, the W-band (75 GHz to 110 GHz). If necessary, further optimisation is carried out to take into account the manufacturing materials usually used by the Technology Group at the Jodrell Bank Centre for Astrophysics (JBCA). Namely: Polypropylene for the dielectric substrate and 2  $\mu\text{m}$  thick copper for the metallic parts.

The drawing of the design takes place within the HFSS user interface. The Computer Aided Design (CAD) tools provided in HFSS allows the drawing of simple two-dimensional polygons and three-dimensional objects from which more complicated structures can be obtained via boolean operations. These can be carried out on entire objects or only their individual faces and edges, as required. Very complicated structures e.g. corrugated horns can be imported

---

<sup>1</sup><http://www.ansys.com/Products/Simulation+Technology/Electromagnetics/Signal+Integrity/ANSYS+HFSS>

from existing CAD drawings made in more specialised CAD software such as AutoCAD<sup>2</sup> or VariCAD<sup>3</sup>. It is also possible to parametrise the dimensions and material parameters of the drawn objects, allowing the software to directly optimise those quantities should it be needed.

Whilst drawing, materials can be assigned to any drawn three-dimensional object. Two-dimensional surfaces can be assigned material properties in the form of surface impedances. HFSS includes a large library of preloaded materials ranging from elements such as copper and silicon to compounds ranging from sea water to a variety of printed circuit board substrates. The library specifies the material properties, the ones relevant to this project being the relative permittivity,  $\epsilon_r$ , permeability,  $\mu_r$ , and their respective loss tangents,  $\delta$ . Custom materials may be added, as was required with polypropylene.

Due to the way FEM works, once the structure has been drawn, what we refer to as an “air box” that encases the structure must be defined. The air box defines the simulation volume within which the electromagnetic fields are calculated by the software. It should be noted that despite being referred to as an *air* box, the material assigned to the volume contained within that box is generally a vacuum (and in some cases polypropylene). Figure 2.1 shows an example of a Jerusalem Cross Pair (JCP) unit cell taken from Vallecchi et al. (2009) within an air box.

### 2.2.2 Boundary Conditions

To ensure the accurate simulation of the electromagnetic fields within the air box, the appropriate boundary conditions must be applied to the walls of the air box. The boundary conditions define the behaviour of the electromagnetic fields at the walls of the air box and this in turn defines what is being simulated. The boundary conditions used in this project, when surrounding a single unit cell, cause the simulation to be that of an infinite two-dimensional array of that unit

---

<sup>2</sup><http://www.autodesk.co.uk/suites/autocad-design-suite/overview>

<sup>3</sup><http://www.varicad.com>

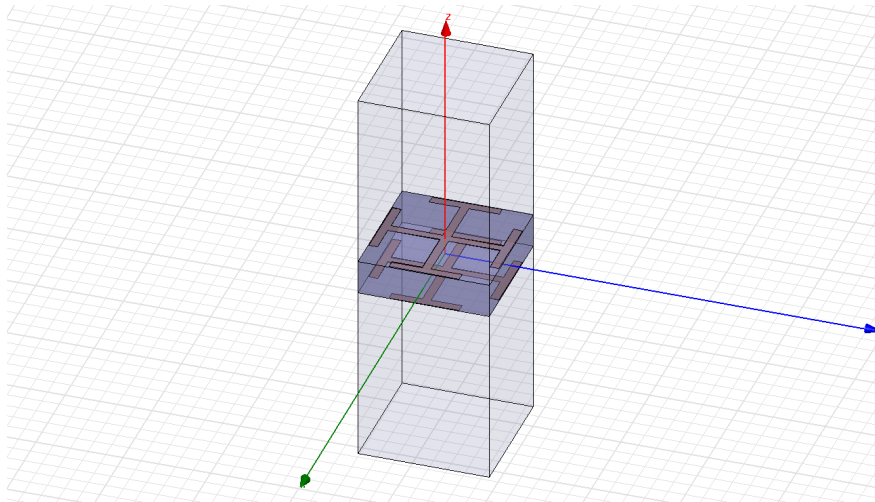


Figure 2.1: An example of a Jerusalem Cross Pair (JCP) unit cell within an air box in HFSS. The outer transparent box is the air box that defines the simulation volume. The copper is seen as the orange-brown structures and the polypropylene substrate is the darker blue box separating the copper pairs. In this simulation setup, to model a planar wave travelling in the  $z$ -direction, ports are defined on the top and bottom surfaces of the air box, and suitable boundary conditions are placed on the remaining side.

cell. HFSS simulations that provide the data presented in this thesis used one of the following three combinations of boundary conditions: 1) Perfect  $E$  (PE) and Perfect  $H$  (PH), 2) PE, PH and symmetry, or 3) Master and slave (M+S).

The JCP from figure 2.1 is now used to demonstrate how the boundary conditions are arranged around the walls of the air box to simulate  $y$ -polarised radiation travelling through an infinite two-dimensional array.

In the first case, involving PE and PH, shown in figure 2.2a, the walls of the air box in the  $x$ -plane are given PE boundaries and the walls in the  $y$ -plane are given PH boundaries. The walls with PE boundaries are defined as being Perfect Electric Conductors (PEC). This means that all  $E$ -fields are forced to be perpendicular to the wall. Similarly, the PH boundaries are defined as being Perfect Magnetic Conductors (PMC) where the  $E$ -fields are forced to be parallel to them. The effect of this is to enforce the  $y$ -polarisation of the radiation.

In the second case if the unit cell has a suitable geometry, and the symmetry

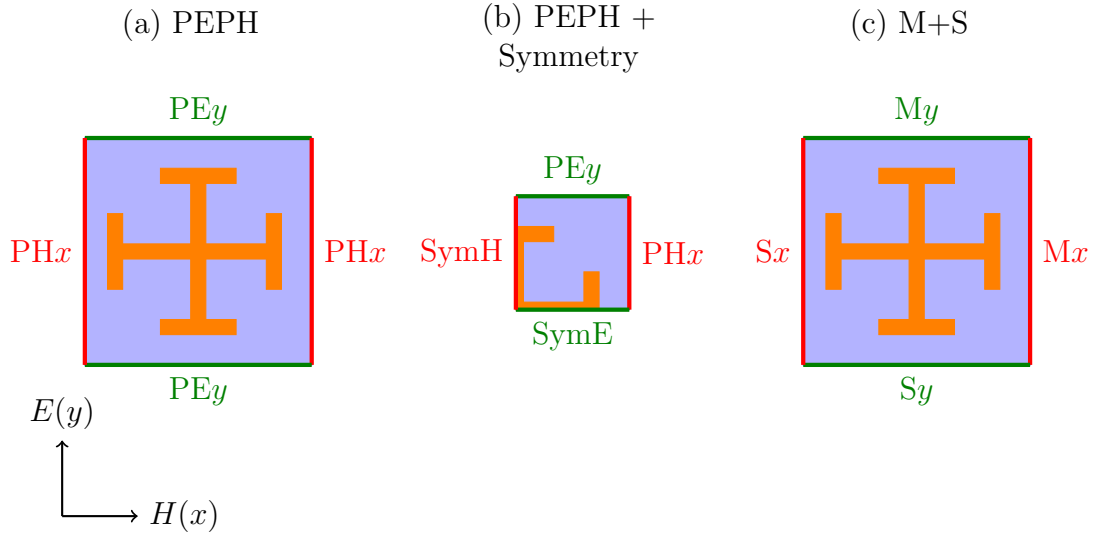


Figure 2.2: Face on view of a Jerusalem Cross Pair (JCP) unit cell inside an air box showing how the boundary conditions are paired up on the walls of the air box to simulate an infinite two-dimensional array of JCP. The alignment of the  $E$  and  $H$  fields are shown by the axis. (a) Utilising PE and PH ensures that the radiation propagating through the JCP is polarised along the  $y$ -axis. (b) The symmetry of the unit cell and the fields in the  $xy$ -plane when radiation is incident allows a simulation that only requires a quarter of the unit cell to be drawn. SymH refers to the  $H$ -plane symmetry boundary condition and SymE refers to the  $E$ -plane symmetry boundary. (c) The Master and slave setup looks similar to that of the PE and PH but the workings are different.

of field lines allow it, symmetry boundary conditions may be applied to reduce the simulation volume (figure 2.2b) and reduce simulation times. Two types of symmetry boundaries exist:  $E$  (labelled SymE in figure 2.2b) and  $H$  (labelled SymH in figure 2.2b). The former is applied when there is symmetry in the  $E$ -field such that the field lines pass perpendicularly through a plane of symmetry. The latter when the  $E$ -fields are parallel to the symmetry plane. These boundaries are used in conjunction with the PE and PH boundaries that are still used on the walls denoting the edges of the unit cell.

The third case uses M+S boundaries. These boundaries work in tandem with one another to also allow the simulation of an infinite two-dimensional array. They do this by forcing the magnitude of the  $E$ -fields on the “slave” boundary

(labelled S in figure 2.2c) to be equal to those on the “master” boundary (labelled M in figure 2.2c) within a given user defined phase difference. An advantage of simulating an infinite array in this way over the PE and PH way was that being able to specify the phase difference between the master and slave walls allowed simulations with incident radiation of arbitrary polarisation rotations and incident angles. With the PE and PH setup only radiation with polarisations aligned with the unit cell’s lattice vectors can be modelled.

### 2.2.3 Excitations

To simulate electromagnetic fields in the presence of the drawn structure in HFSS, a source of electromagnetic radiation must be defined. HFSS has seven types of excitations, of which only two were used in the simulations shown in this thesis. They were wave ports and floquet ports.

Wave ports act as entrances and exits for linearly polarised plane wave radiation to enter and exit the air box. When wave ports are defined in HFSS, the polarisation of the radiation can be defined. During simulations, HFSS uses the location of the ports as the reference planes where the scattering parameters (S-parameters) are calculated. They are used with PE and PH boundary conditions described in section 2.2.2. Wave ports, in combination with the PE and PH boundaries, are good for quick simulations where the incident radiation is incident at  $0^\circ$  and its polarisation is aligned to one of the unit cell’s lattice vectors.

Floquet ports, like wave ports, also act as an entrance and exit for radiation. However they are used solely with the master and slave boundary conditions to enable simulations of structures periodically arranged into an infinite two-dimensional array e.g. Frequency Selective Surfaces (FSS) and phased array antennas. Floquet ports have the ability to act as the source and sink for more than one type of polarisation at a time. It can also be used in simulations that require data where the incident radiation has a non-zero degree angle of incidence.

### 2.2.4 Simulation Process

As part of the FEM modelling process, when running a simulation, HFSS goes through an iterative process where the air box and its contents are “meshed” into smaller and smaller tetrahedra. In each iteration or “adaptive pass” after a new mesh has been created, HFSS solves the differential forms of Maxwell’s equations at various locations on each tetrahedra to recreate the electromagnetic fields within the air box.

Assuming wave ports or Floquet ports as the excitation, from this mesh HFSS then calculates the values of the S-parameters at the ports. The value of the S-parameters are compared to the values calculated in the previous iteration and a value referred to in the HFSS manuals as Max Delta S or  $\max |\Delta S_{ij}|$  is calculated. This value is equal to the maximum magnitude change made by one of the S-parameters between the consecutive iterations. Once this value reaches below a user defined threshold for a user defined number of adaptive passes the simulation is said to have converged. The author generally set the value of  $\max |\Delta S_{ij}|$  to be between 0.001 to 0.01 for three to six consecutive runs. Large structures and those requiring a further frequency sweep were set closer to the minimum value of the  $\max |\Delta S_{ij}|$  for a greater number of consecutive passes.

To reach convergence, HFSS adapts the mesh in each pass such that it becomes finer in regions where the electromagnetic field is strong and coarser in regions where it is weak. It also adapts for the material parameters so that a material with high values of  $\epsilon_r$  or  $\mu_r$  are also finely meshed. This can be seen in figure 2.3 where the mesh density is greatest at the top and bottom arms of the JCP where the magnitude of the  $E$ -fields between neighbouring cells is high.

### 2.2.5 Frequency Sweeps

The mesh created in section 2.2.4 is optimised for the user defined solution frequency. In cases when the frequency dependent behaviour is required an inter-

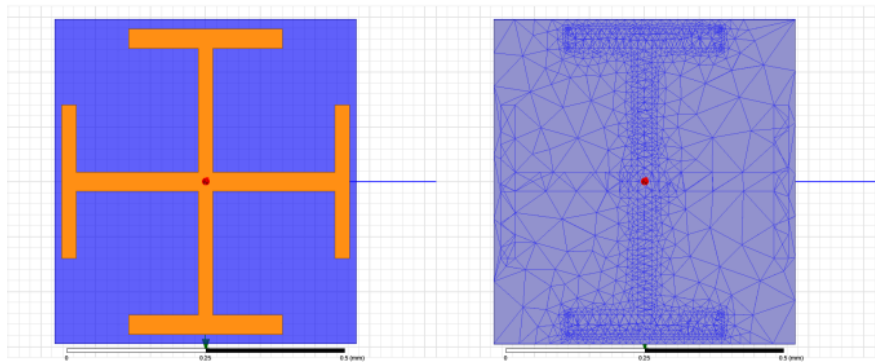


Figure 2.3: A face on view of the JCP unit cell from figure 2.1 on the left and the plot of the tetrahedral mesh made by the adaptive meshing as part of the simulation process on the right. Note how the mesh is finer on the top and bottom copper arms. This is where the fields were strongest in this particular simulation.

polating frequency sweep was generally used. Other frequency sweeps available are the fast sweep and the discrete sweep. Each sweep type has their advantages and disadvantages.

The interpolating sweep has the advantage of requiring less RAM to run and can be used for frequency sweeps covering very large bandwidths. Anecdotally, the author found that frequency sweeps in the range 10 GHz to 60 GHz, equivalent to a fractional bandwidth of 143 %, were possible when modelling blocks of dielectric. The sweep works in a similar way to the iterative meshing process described in 2.2.4. By using the existing mesh, the software solves for the fields at other frequency points within the sweep's bandwidth, interpolates the frequency dependence of the S-parameters from the points and then calculates the difference between the interpolation solutions between this and the previous sweep. This continues until the error tolerance is below a user defined value, which the author set to 0.1 %.

Another type of frequency sweep used was the fast sweep that relies on an Adaptive Lanczos-Padé Sweep procedure. According to the literature provided by Ansys (Ansoft 2009) the advantage of this sweep is that it is accurate in cases where the behaviour of a structure near resonance is required. It allows the visualisation of the fields at any frequency point within the sweep's bandwidth once the sweep has completed. This is in contrast to the interpolating sweep that

can only provide the data for the solution frequency it was initially set at. The fast sweep cannot be used for sweeps as broad as what the interpolating sweep can achieve. It also requires a lot more RAM than the interpolating sweep.

Discrete frequency sweeps are slowest sweeps if a large number of points is required. Whereas the above two methods use different numerical methods to interpolate the frequency dependent behaviour, the discrete sweep directly solves the fields at each frequency point within the sweep using the mesh that was adapted for the initial solve frequency. Because of this, discrete sweeps can be viewed as being the more accurate sweeps of the three available. It also allows the visualisations of the fields at frequencies other than at where the solution frequency was set.

In all three of the sweeps above, data is computed from a mesh that was adapted to the solution frequency. Using this mesh to compute data at frequencies close to the solution frequency is okay, but the further the frequency being calculated is from the solution frequency, the less accurate the results. Through trial and error the author found that with the interpolating sweep set to a solution frequency of 103 GHz the full W-band could be swept in one go, as opposed to needing to make a number of smaller sweeps. To ensure the S-parameters were accurate across the entire W-band, two to three further simulations were set up with their solution frequencies set at 78 GHz, 92.5 GHz and 108 GHz. If the S-parameters for these simulations concurred with those of the interpolating sweep at those frequencies, the sweep was deemed accurate. In cases where the fast sweep was utilised the same procedure was also carried out albeit with the solution frequency of the sweep set to 92.5 GHz.

## 2.3 Transmission Line Modelling

Noting that the  $E$  and  $H$  fields of electromagnetic radiation have counterparts in the transmission line realm as voltages and currents we are able to model the

behaviour of metal mesh grids, FSS and metamaterials with a Transmission Line (TL) based model. The behaviour of an individual 2D grid can be described with one or more lumped elements to form an equivalent circuit. A single layered grid of metallic squares for example, otherwise known as a capacitive grid, can be simply modelled as a shunt capacitor. The complementary of the capacitive grid, a single layer of metal wires, is known as an inductive grid, and a simple model can be made from a single shunt inductor. More accurate models can be made by adding additional lumped elements to the equivalent circuit e.g. a resistor to account for absorption and the associated losses (Ulrich 1967).

Analytical forms for values such as the reflection and transmission can be derived from these equivalent circuits. The values of the capacitance, inductance and resistance of the lumped elements can be calculated from analytically derived equations that relate the geometry of the grid to the lumped elements, examples of which can be seen in Marcuvitz (1965). Alternatively they can be fitted to match lab measured or simulated transmissions of the grids. When a cascade of grids is required to be modelled, the equivalent circuit can be represented in calculations by a transmission matrix taken from existing tables such as Pozar (2012, Table 4.1). These matrices can then be cascaded one after the other mimicking the layout of the real life device. The reflection and transmission of the device can then be calculated via a simple matter of matrix multiplication. This is advantageous due to the minimal computing resources required to carry it out and the simplicity of coding the model in various programming languages. Indeed, all TL modelling carried out during this project was coded using MATLAB<sup>4</sup> by the author.

A downside to using analytically derived expressions for the lumped elements is that such constructions are, in the end, approximations to the real behaviour of the fields involved. This can manifest itself when accurate values of phase are required from TL models (Pisano et al. 2012c).

---

<sup>4</sup><http://www.mathworks.co.uk/products/matlab/>

## 2.4 The New Transmission Line Model

### 2.4.1 FEM Seeding of Transmission Line Matrices

Modelling the frequency dependent behaviour of a cascaded set of metamaterial cells via FEM can be prohibitively expensive in terms of CPU time and RAM. Also, certain constructions of cascaded metamaterials cannot be modelled easily as a single unit cell in HFSS e.g. the cascaded wave plates that will be described in chapter 5 where the unit cells are rotated with respect to one another through arbitrary angles. To overcome this, the FEM model of section 2.2 and the TL modelling of section 2.3 were combined into a hybrid method.

Accurate S-parameters from HFSS simulations are used to seed the matrices of the TL method. This method combines the accuracy of the data calculated by HFSS with the less computationally intensive process of multiplying a chain of smaller  $2 \times 2$  or  $4 \times 4$  matrices to obtain a final result.

The frequency dependent behaviour of a unit cell can be described using the  $ABCD$  (transmission) matrix of the form:

$$\begin{bmatrix} E \\ H \end{bmatrix}_i = \begin{bmatrix} A & B \\ C & D \end{bmatrix} \begin{bmatrix} E \\ H \end{bmatrix}_t \quad (2.1)$$

where  $E$  and  $H$  are electric and magnetic fields. The subscripts  $i$  and  $t$  respectively denote whether the fields are incident or transmitted. To obtain the  $ABCD$  parameters, a HFSS simulation of a unit cell is set up and run as described in section 2.2. As noted in section 2.2.3, when HFSS calculates the S-parameters it does so using the position of the ports as the reference plane. The location of the reference plane controls the recorded value of the S-parameters' phase. For the purpose of this method, we required the phase information to be taken at the outer most surfaces of the unit cell, and so this is where the reference planes (dashed green lines in figure 2.4) are moved.

This can be done either in HFSS (where the process is called “deembedding”)

## 2: DESIGNING METAMATERIALS

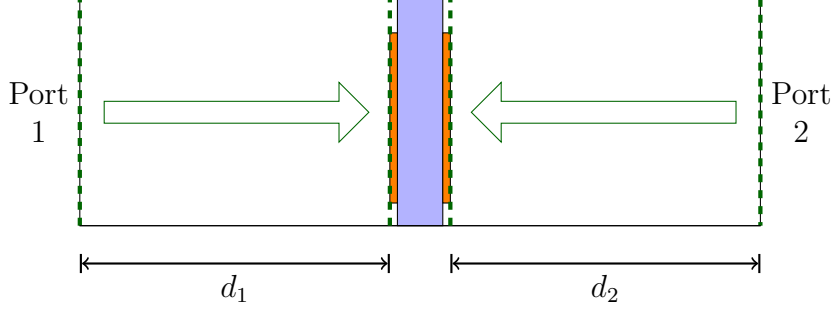


Figure 2.4: Side view of an air box containing a single unit cell. The dashed lines represent the reference planes on which the phase component of the S-parameters lie.

or manually after the S-parameters have been exported using

$$S_{11} = S'_{11} \exp(i2n_{\text{env}}k_0d_1) \quad (2.2a)$$

$$S_{12} = S'_{12} \exp(in_{\text{env}}k_0(d_1 + d_2)) \quad (2.2b)$$

$$S_{21} = S'_{21} \exp(in_{\text{env}}k_0(d_1 + d_2)) \quad (2.2c)$$

$$S_{22} = S'_{22} \exp(i2n_{\text{env}}k_0d_2) \quad (2.2d)$$

where  $S'_{ij}$  and  $S_{ij}$  are respectively the S-parameters before and after the reference planes have been moved,  $n_{\text{env}}$  is the refractive index of the environment around the unit cell,  $k_0$  is the free space wave number equal to  $2\pi f/c_0$  and  $f$  is frequency and  $d_1$  and  $d_2$  are the distances between the unit cell's outermost surface and the wave ports.

The S-parameters are then converted to  $ABCD$  matrices using equations taken from Pozar (2012, Table 4.2):

$$A = \frac{(1 + S_{11})(1 - S_{22}) + S_{12}S_{21}}{2S_{21}} \quad (2.3a)$$

$$B = Z \cdot \frac{(1 + S_{11})(1 + S_{22}) - S_{12}S_{21}}{2S_{21}} \quad (2.3b)$$

$$C = Y \cdot \frac{(1 - S_{11})(1 - S_{22}) - S_{12}S_{21}}{2S_{21}} \quad (2.3c)$$

$$D = \frac{(1 - S_{11})(1 + S_{22}) + S_{12}S_{21}}{2S_{21}} \quad (2.3d)$$

where  $Z$  is  $Z_0/n_{\text{env}}$  and  $Y$  is  $Y_0n_{\text{env}}$ . This  $ABCD$  matrix, now models the frequency dependent behaviour of the unit cell. When modelling a cascade of unit cells that are separated by a distance,  $d$ , between their outermost surfaces this separation can be represented by the propagation matrix (Pozar 2012, Table 4.1):

$$\begin{bmatrix} E \\ H \end{bmatrix}_i = \begin{bmatrix} \cos(n_{\text{env}}k_0d) & iZ \sin(n_{\text{env}}k_0d) \\ iY \sin(n_{\text{env}}k_0d) & \cos(n_{\text{env}}k_0d) \end{bmatrix} \begin{bmatrix} E \\ H \end{bmatrix}_t. \quad (2.4)$$

In the scenario that the cells are embedded within a non-magnetic medium (i.e.  $\mu_r = 1$  and  $\varepsilon_r \neq 1$ ), a matching matrix is also required to account for the effects caused by the radiation passing between the air/media interface. So for radiation passing from medium 1 with refractive index,  $n_1$ , to medium 2 with refractive index,  $n_2$ , the matrix takes the form:

$$\begin{bmatrix} E \\ H \end{bmatrix}_i = \begin{bmatrix} 1 & 0 \\ 0 & \frac{n_2}{n_1} \end{bmatrix} \begin{bmatrix} E \\ H \end{bmatrix}_t. \quad (2.5)$$

To model a device using the TL method, the matrices are cascaded one after the other, and then multiplied in the usual way with the values of the incident  $E$  and  $H$  set to equal one. To get the S-parameters back for further analysis, the following equations from Pozar (2012, Table 4.2) are used:

$$S_{11} = \frac{A + YB - CZ - D}{A + YB + ZC + D} \quad (2.6a)$$

$$S_{12} = \frac{2(AD - BD)}{A + YB + ZC + D} \quad (2.6b)$$

$$S_{21} = \frac{2}{A + YB + ZC + D} \quad (2.6c)$$

$$S_{22} = \frac{-A + YB - CZ + D}{A + YB + ZC + D}. \quad (2.6d)$$

An alternative to the  $E$  and  $H$  fields, are the forward and backward  $E$ -fields. For an  $x$ -polarised wave with  $\exp(+i\omega t)$  time dependence, propagating along the  $z$ -axis, the forward and backward  $E$ -fields are respectively represented as

$E_+ = E \exp(-ikz)$  and  $E_- = E \exp(ikz)$ .  $E_+$  and  $E_-$  are related to  $E$  and  $H$  by the following matrices from Orfanidis (2010, Chapter 5):

$$\begin{bmatrix} E \\ H \end{bmatrix} = \begin{bmatrix} 1 & 1 \\ Y & -Y \end{bmatrix} \begin{bmatrix} E_+ \\ E_- \end{bmatrix} \quad \text{and} \quad \begin{bmatrix} E_+ \\ E_- \end{bmatrix} = \frac{1}{2} \begin{bmatrix} 1 & Z \\ 1 & -Z \end{bmatrix} \begin{bmatrix} E \\ H \end{bmatrix}. \quad (2.7)$$

Equivalent forms of equations (2.3) to (2.5) for  $E_+$  and  $E_-$  can be derived from equation (2.7) as described in Orfanidis (2010, Chapter 5).

### 2.4.2 Comparison Between FEM & New TL Model

A simple demonstration will be made to show that the hybrid method is able to produce results as accurate as those derived from an FEM as well as show the regime where it ceases to function. The demonstration involves two 2D arrays of metallic squares with side length  $300 \mu\text{m}$  that are made of a PEC. The gap between each neighbouring square in the same layer is  $50 \mu\text{m}$ . The distance between the two squares is varied from  $50 \mu\text{m}$  to  $500 \mu\text{m}$  and the results derived via HFSS and those using the hybrid TL method are compared.

Two HFSS simulations were run by the author. The first with only a single PEC square in vacuum simulation volume. The S-parameter data from this simulation would be used to seed the  $ABCD$  matrices in the TL model coded by the author using MATLAB. The second simulation performed the parameter sweep, altering the distance between the squares and making frequency sweeps at each increase in distance. The setup of which is shown in figure 2.5. The S-parameter data from this simulation would provide the accurate FEM modelled S-parameters with which to compare the TL model with.

The results are displayed in a series of graphs in figure 2.6 and figure 2.7. Below  $300 \mu\text{m}$  separation we see that there is no match between the FEM and TL data. This is because of the break down in the TL model that assumes no interaction between different components. In this regime the electric fields of the

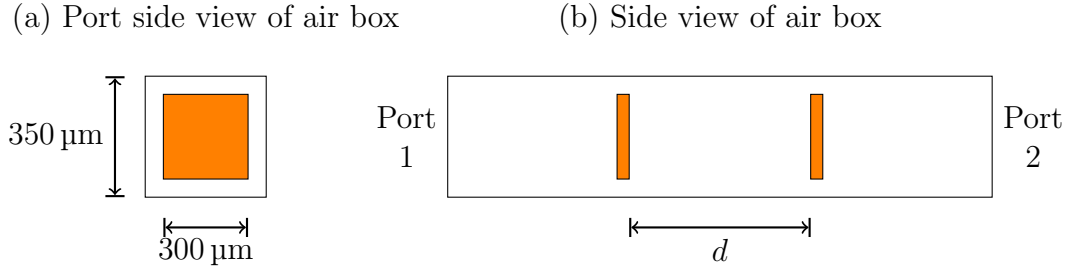


Figure 2.5: Diagram of the simulation layout used in the two PEC square case in section 2.4.2. The air box is represented as a black outline. The PEC used in the HFSS simulations had a thickness of  $2\ \mu\text{m}$  and is represented here by orange.

two metallic squares are able to influence one another. The effect of the TL model not accounting for this interaction is the underestimation of the final transmitted intensity,  $|S_{21}|^2$  and the shifting of the transmitted phase,  $\arg(S_{21})$ .

This entails that when doing TL modelling, there is a minimum distance that must be exceeded if the results are to be accurate. The required minimum separation is dependent on the surrounding medium, the geometry of the grids and the frequency of the radiation involved. As the separation of the two squares grids increases the difference between the FEM and TL model decreases. At  $300\ \mu\text{m}$  separation and above the match between the FEM and TL data is very good. For these grids a minimum separation of  $300\ \mu\text{m}$  could be assigned. Once we reach  $500\ \mu\text{m}$  the difference between the two are negligible. The values of  $|S_{21}|^2$  only differ by  $\sim 10^{-4}$  and  $\arg(S_{21})$  differ by  $< 1^\circ$ .

The FEM seeded TL model has been used with other geometries and with cascades of more than two grids with similar convergence seen. It also works in the metamaterial cases described later in this thesis where instead of a single grid being represented by the  $ABCD$  matrix, pairs and triplets of grids are. In this project the FEM seeded TL model was used for the modelling of the wave plates described in chapter 5.

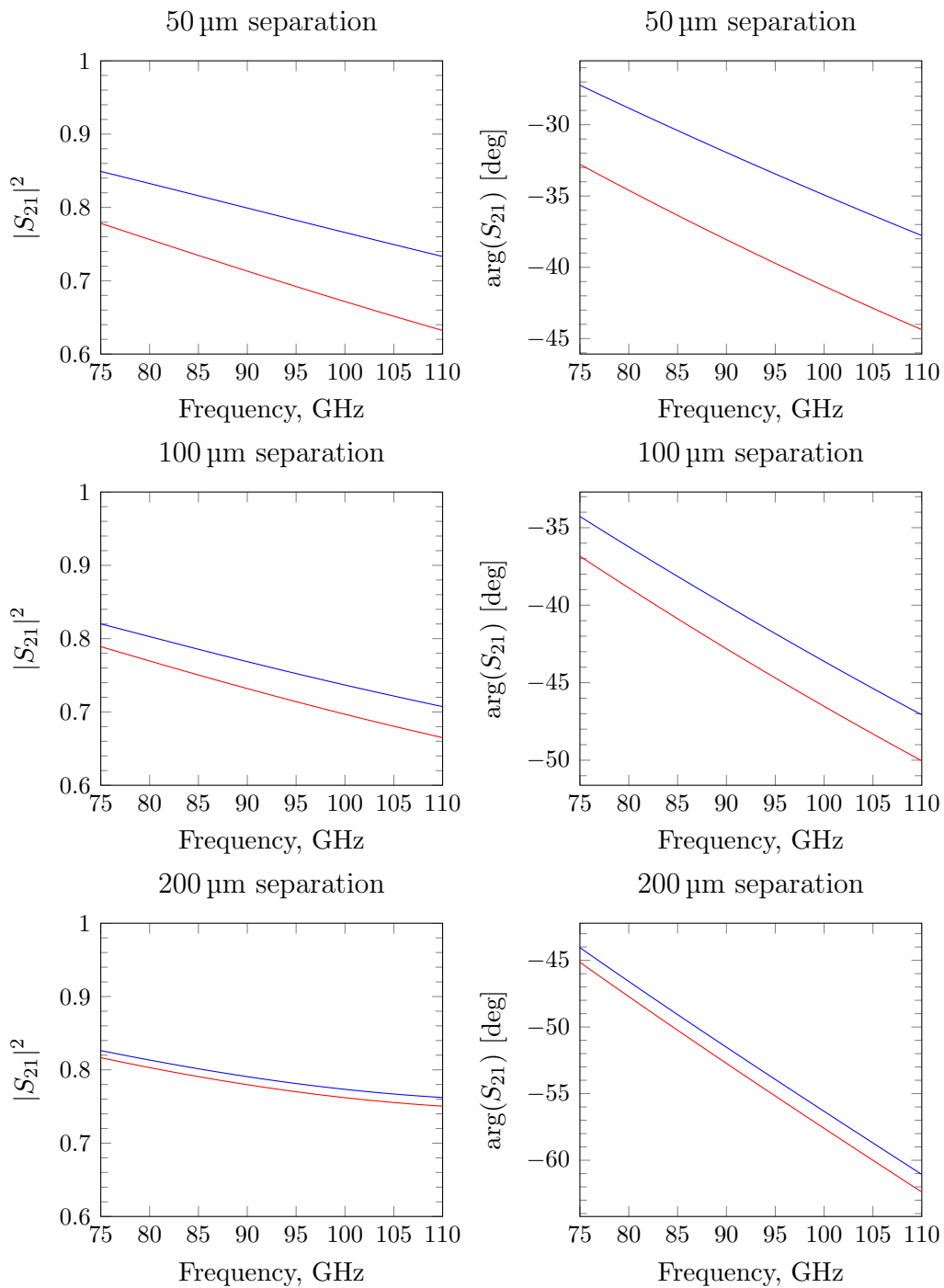


Figure 2.6: Calculated values of transmitted intensity and transmitted phase of radiation from HFSS simulations (blue) and TL model (red) for two PEC squares separated between 50  $\mu\text{m}$  to 200  $\mu\text{m}$ .

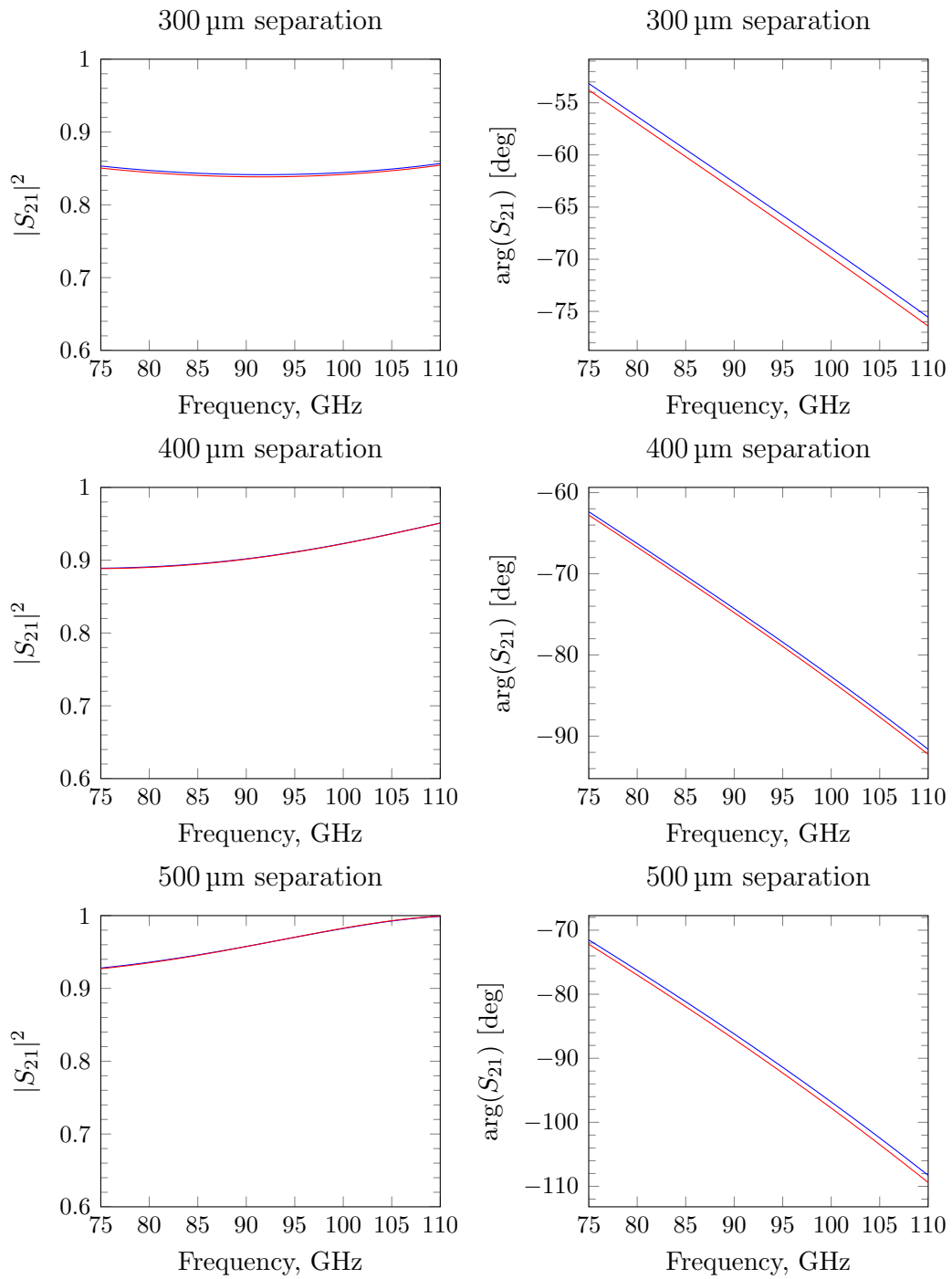


Figure 2.7: Calculated values of transmitted intensity and transmitted phase of radiation from HFSS simulations (blue) and TL model (red) for two PEC squares separated between 300  $\mu\text{m}$  to 500  $\mu\text{m}$ .

*2: DESIGNING METAMATERIALS*

# Chapter 3

## Manufacturing Metamaterials

*I have never done anything  
'useful'. No discovery of mine has  
made, or is likely to make,  
directly or indirectly, for good or  
ill, the least difference to the  
amenity of the world.*

Godfrey Harold Hardy, 1940  
November

### 3.1 Introduction

To quote a line from Pendry (2000), “No scheme can be of much interest if the means of realizing [sic] it are not available.” The means of realising metamaterials can take different forms but the majority are based on some form of lithography and etching. In this chapter, the means of metamaterial fabrication and device construction used during this project are described. A brief description of other types of fabrication and construction methods used in the scientific literature will be given along with the differences and similarities to the method used during this project brings this chapter to a close.

During this project, the stages of fabrication and manufacture of the devices described in chapter 4 and chapter 5 were carried out by Dr. M. W. Ng, Dr. V.

Haynes and the author in various combinations. Unless otherwise stated, the stages described in this chapter were carried out by the former two.

## 3.2 Metamaterial Fabrication

### 3.2.1 Photolithography

Photolithography is the fabrication method adopted by the Technology Group at the Jodrell Bank Centre for Astrophysics (JBCA). The method has been applied successfully in the fabrication of metal mesh grids that have been used to manufacture devices such as metal mesh wave plates, metal mesh lenses and dichorics that work between 30 GHz to  $> 100$  GHz region of the radio spectrum. These same fabrication methods can be applied to the manufacture of planar metamaterials. The details of the method are outlined in the following subsections.

#### 3.2.1.1 Mounting & Polypropylene Annealing

With a suitable geometry, a metamaterial could be manufactured as a free standing metallic structure. However, this is difficult to manufacture and the end result is impractical for most applications. For this reason a dielectric substrate, polypropylene, is used. Polypropylene is chosen for its low dielectric losses ( $\delta = 7 \times 10^{-4}$  (Lamb 1996)) and its thermo-mechanical properties that allow it to be used with relative ease to manufacture complex devices.

Initially, the polypropylene substrate must be mounted onto aluminium rings. This is done by laying a sheet of polypropylene onto a clean surface inside a fume cupboard. Aluminium rings with adhesive applied to one side are placed onto the polypropylene sheet and left to dry for 24 h (figure 3.1). Once dried, the polypropylene outside the ring is cut away from the sheet. Excess polypropylene on the rings are scraped away from the edges with a scalpel. The rings are then placed into a computer controlled fan oven (figure 3.2) which heats the polypropylene

### 3.2: METAMATERIAL FABRICATION

according to a temperature profile that results in temperature being slowly raised up to 150 °C where it remains for ~ 30 min and then slowly cooled back down to room temperature. The heating process is required to make the polypropylene taut and provide a flat surface for the copper that will be evaporated onto it in



Figure 3.1: Five 10 cm aluminium rings on top of a sheet of polypropylene.

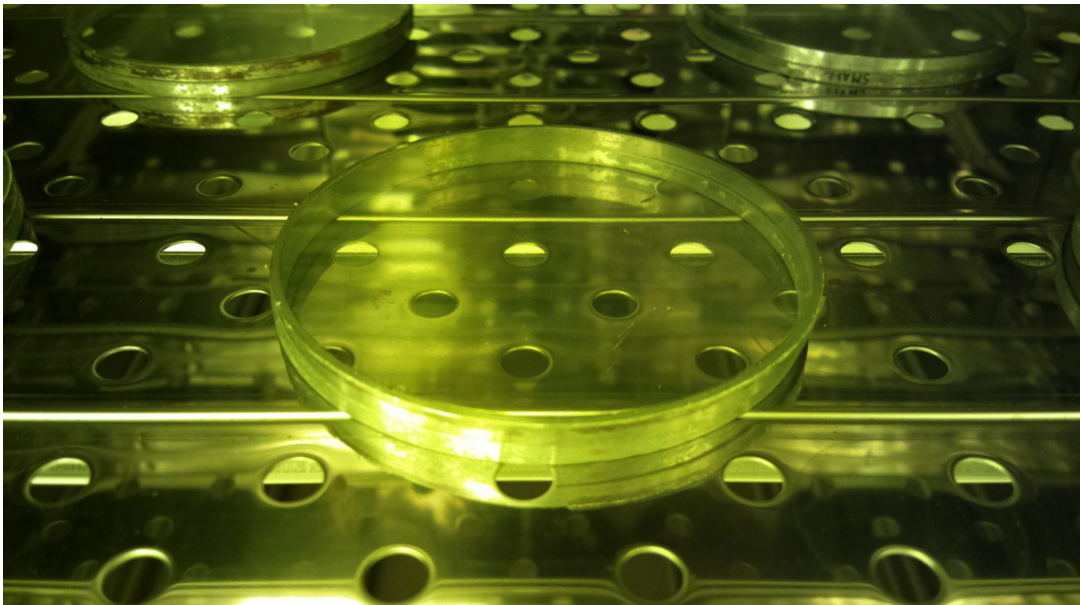


Figure 3.2: Rings with polypropylene being annealed inside fan oven.

the next step. The tautening happens because when heated close to its melting point, the polymer chains in the polypropylene gain enough energy to slide past one another, realigning themselves, allowing them to reach a lower equilibrium state.

This stage was carried out by the author to create the aluminium mounted polypropylene described on page 121 of section 4.3.6 and the ring mounted Half Wave Plates (HWPs) of section 5.4.3.

#### **3.2.1.2 Copper Coating**

The ring mounted polypropylene is then coated with a 2  $\mu\text{m}$  layer of copper using an evaporation chamber. Within this chamber, kept at low pressure by a vacuum pump, a sample of copper is heated to very high temperatures by application of an electric current. The combination of the low pressure and high temperature cause the copper to evaporate. The vacuum ensures that the copper atoms have a large mean free path to reach the polypropylene substrate without bumping into air molecules. This would have negative consequences such as reducing the uniformity of the copper being deposited onto the polypropylene. The thickness of the copper on the polypropylene samples is measured using a quartz piezoelectric crystal located near the rotating stage at the height of the polypropylene sample. An alternating current passing through the crystal causes it to oscillate at its resonant frequency. As copper gets deposited on the crystal, the resonant frequency changes, allowing the thickness of copper deposited to be determined.

The ring mounted polypropylene samples are placed onto a rotating circular platform above the heated copper sample. The evaporated copper atoms that reach the rotating stage condense onto the surface of the polypropylene (and the rotating stage). Figure 3.3 shows a large sample that has been coated in copper. The entire process takes between 3 h to 6 h with the copper being deposited at a rate of  $0.1 \text{ nm s}^{-1}$  to  $0.2 \text{ nm s}^{-1}$ .



Figure 3.3: A freshly copper coated polypropylene sample 53 cm in diameter.

### 3.2.1.3 Photoresist Coating

This and the remaining steps are carried out within a clean room to prevent contamination from unwanted particles such as dust, fibres and chemical vapours. A solution of positive photoresist (S1805) is applied on the copper's surface using a spin coater. The copper sample is spun up to 4000 rpm for  $\sim 20$  s to ensure that an even coating of the photoresist is established on the copper's surface. A photoresist is a chemical that when exposed to ultraviolet light in section 3.2.1.4, breaks down and becomes soluble in a developer solution. The photoresisted copper is heated in an oven at  $95^{\circ}\text{C}$  for  $\sim 1$  h to evaporate the solvent leaving behind the photoresist on the copper.

### 3.2.1.4 Photo Mask Production & Exposure

A necessary step in the grid production is the transferring of the grid design onto the copper and the removal of the unwanted material. To do this requires the use of a "positive" photo mask and an ultraviolet (UV) exposure box. The photo mask is a positive of the grid design and it blocks the UV light from reaching

### 3: MANUFACTURING METAMATERIALS

the photoresist in the regions where copper is required. From the initial unit cell geometry, a two-dimensional CAD drawing is made by Dr. M. W. Ng from which the photo masks were manufactured by JD Photo-Tools<sup>1</sup>.

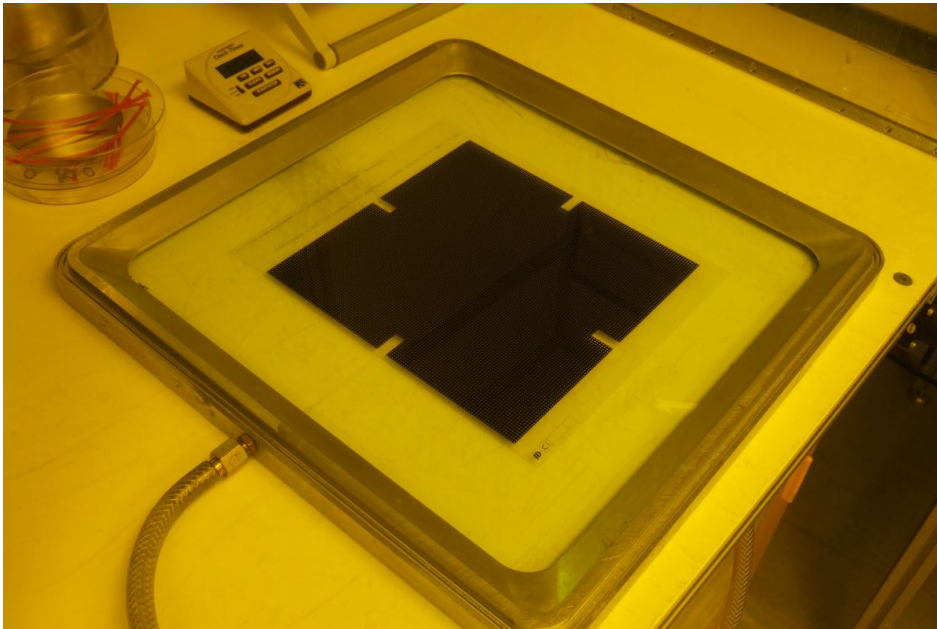


Figure 3.4: Photo mask (black) on the vacuum tray. The four slot like gaps in the photo mask contain alignment marks that will be photolithographed onto the copper and be used to aid alignment of the grids in section 3.3.1

The photo mask is placed onto the glass surface of the vacuum tray (figure 3.4) orientated so that the photo mask appears reversed from the operators perspective. The copper sample is placed photoresist-coated side down onto the photo mask (figure 3.5) taking care that it is centrally placed. The other half of the vacuum tray is placed on top of the sample and air is pumped out from the tray. This ensures good contact between the photo mask and the copper sample. The vacuum tray is then inserted into an exposure box (figure 3.6) containing LEDs (light emitting diodes) emitting UV radiation (peak intensity at 390 nm or 769 THz). The tray, photo mask side up with the photo mask facing the LEDs, is then left to expose for  $\sim 3$  min.

---

<sup>1</sup><http://jdphoto.co.uk>

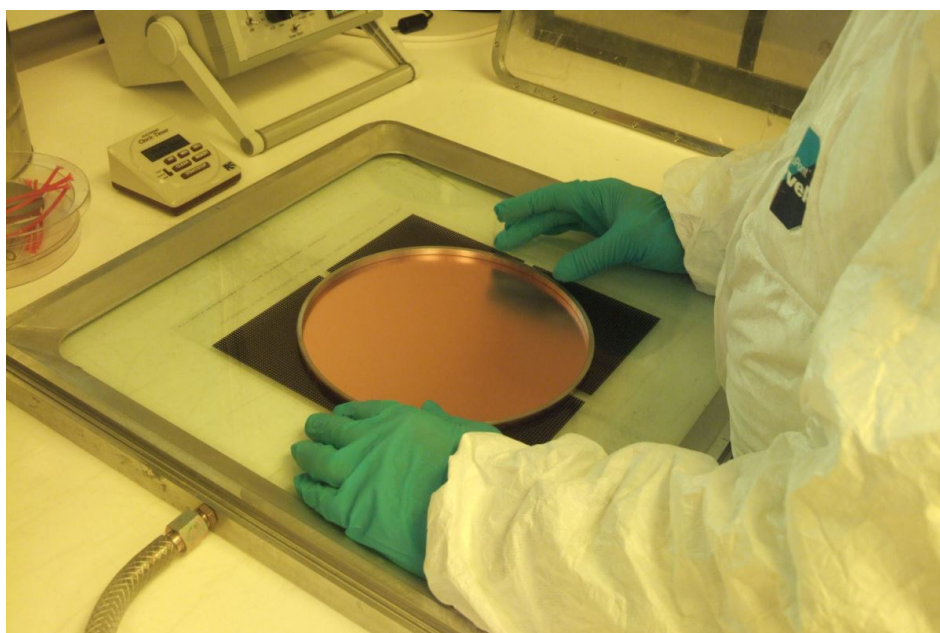


Figure 3.5: Copper sample being aligned by eye to ensure it is centrally placed on top of the photo mask. The tube visible on the bottom left of the photo connects to the vacuum pump.

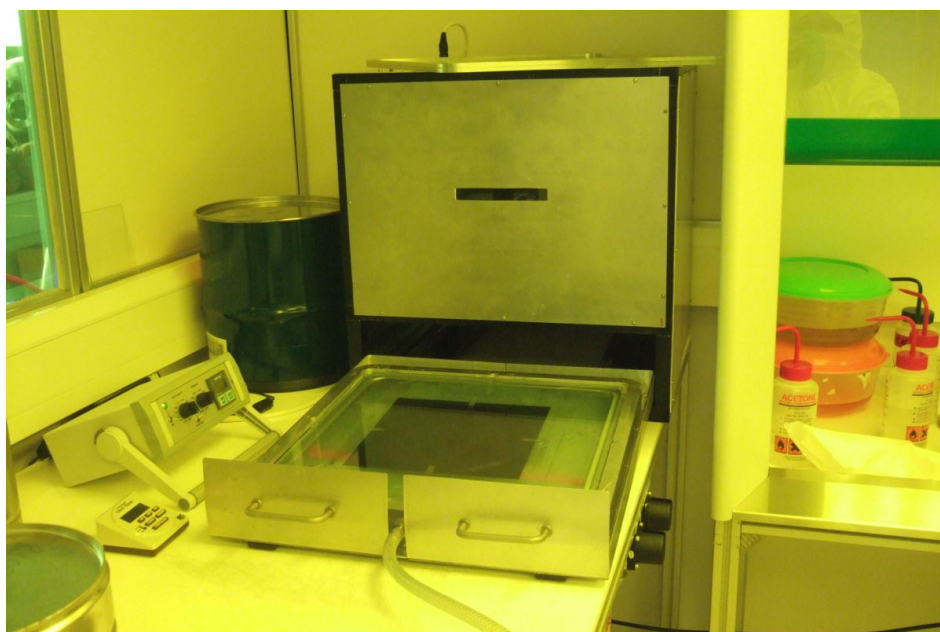


Figure 3.6: Vacuum tray containing the photo mask and sample about to loaded into the exposure box.

### 3.2.1.5 Development & Etching

The sample is removed from the vacuum tray and placed into a developer solution made from potassium hydroxide and potassium chloride for  $\sim 3$  min whilst being swirled around in the solution to ensure all parts of the copper are covered. The developer, after removing the remaining photoresist that was not exposed to the ultraviolet radiation is washed off by immersion in water for  $\sim 20$  s.

The sample is then placed into an etching solution which is contained in a bowl placed above a light box (figure 3.7). The etching solution is a made from 10% ammonium persulphate and 2% sulphuric acid. In this solution, the sample is slowly swirled and swayed around until light can be seen to shine through the gaps left by the copper that has been etched away (figure 3.8). The remaining etching solution is removed by spin drying the sample, a process that requires the sample to be spun at high speed for 20 s.

After this its quality can be inspected either by eye, under a loupe (handleless

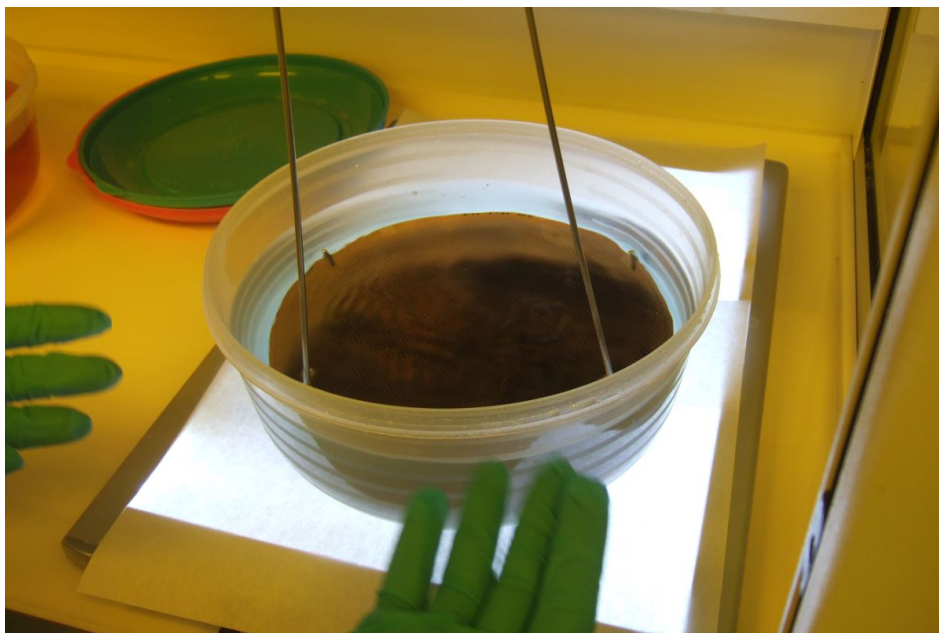


Figure 3.7: Copper coated polypropylene sample in bowl of etching solution above light box. Note how no light passes through the sample as no copper has been etched yet.

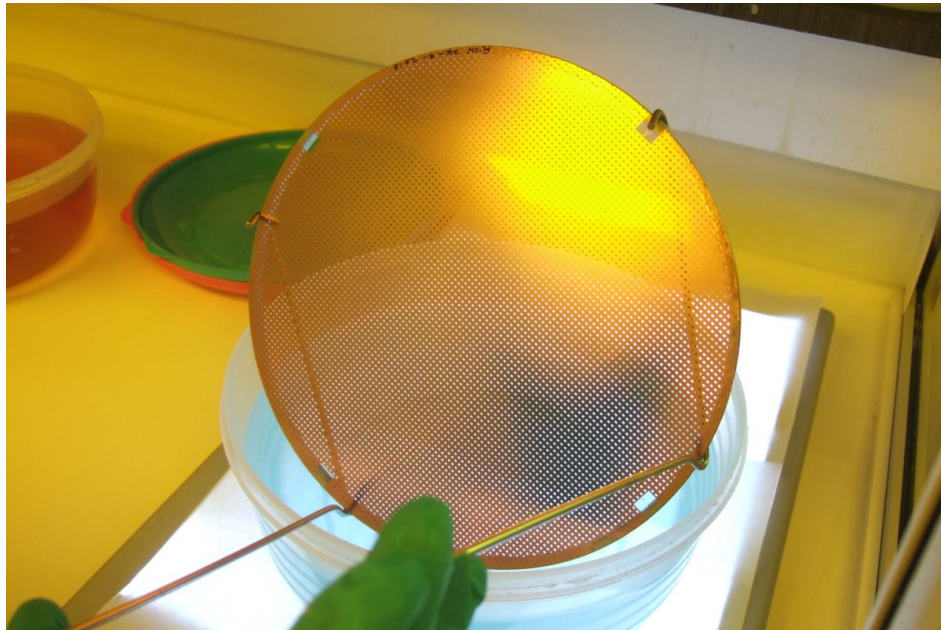


Figure 3.8: Copper sample after etching is complete. Light is now able to pass through the gaps left behind.

magnifying glass) or microscope for defects such as e.g. unsharp edges and curved corners, if these not part of the original design. The grids are then left to air dry in the clean room.

### 3.3 Device Manufacture

#### 3.3.1 Alignment & Stacking

Devices are rarely made from just a single grid but are instead built up layer by layer by careful alignment and stacking of additional grids and extra polypropylene sheets. This and the later described stages were carried out outside the clean room. These stages of the manufacturing for all the devices described in chapter 4 and chapter 5 were carried out by the author. Before starting this step a “recipe” for the device was drawn up. An example of such a recipe can be seen in figure 5.10 on page 150. The recipe provides a cut-through view of the device providing the number of grids, the polypropylene sheets required and their thickness. This recipe

### *3: MANUFACTURING METAMATERIALS*

is then used as a guide during the aligning and stacking stage to ensure each layer is correctly placed.

The copper grids were carefully cut away from the aluminium rings and stored in a plastic tray for later use. Early on in the project, the grids and polypropylene sheets would respectively be aligned and stacked in turn, following the recipe. Later, based on the recipe, the grids were prebonded with polypropylene sheets to reduce the number of individual layers that had to be handled during the alignment stage. Another advantage is that the prebonding makes each layer more rigid and easier to handle. An example of a recipe showing how the layers are defined from the individual copper grids and polypropylene sheets can be seen in figure 4.23 on page 115. The prebonding is carried out by hot pressing, which will be explained later in section 3.3.2. The alignment and stacking was carried out on top of a light box covered in plastic sheeting to protect the light box's surface from possible damage caused by the soldering iron that will be used later. The plastic sheets were cleared of dust and other impurities using an air gun and by wiping the surface with isopropan-2-ol using non-woven wipes (Durx® 670A). Using thin strips of sticky tape, the first grid is stuck down to the plastic sheets to prevent it from moving. The second grid was placed on top and weighed down with a suitably sized cylindrical glass block (figure 3.9). Repositioning of the second grid is done by moving the glass block.

A quick initial alignment was done by matching the circumferences of the two grids and then maximising the light shining through the them (judged by eye), as can be in the series of photos in figures 3.9 to 3.11. To ensure the best performance the alignment of each layer must be accurate. Standard practice makes use of “+”-shaped alignment marks that are generally located at and labelled as the four compass points of the photo mask. These are photolithographed together with the grids (figure 3.12). If required, additional alignment marks can also be placed at other locations. Aligning the grids correctly then becomes a simple case of adjusting the position of the grids until the alignment marks are on top of one



Figure 3.9: Two grids layered on top of one another and held down with a cylindrical glass block. This photo demonstrates a worst case scenario of bad alignment when no light is able to pass through.

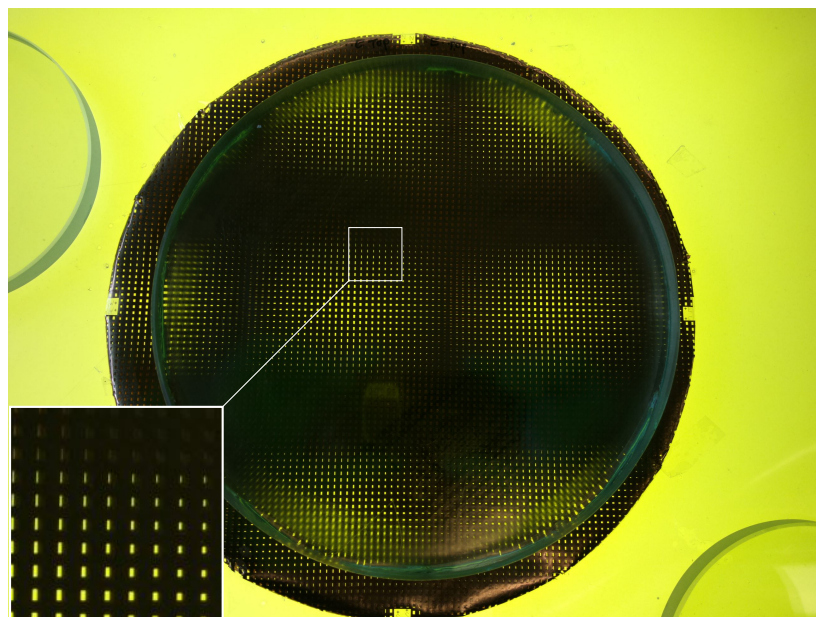


Figure 3.10: Moving the top grid slightly demonstrates how a small change in can increase the light transmitted.

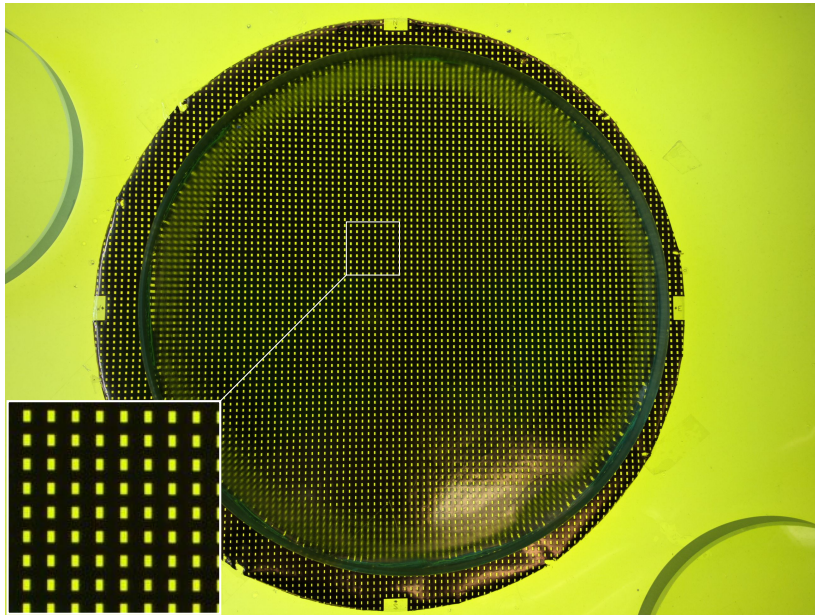


Figure 3.11: When maximally achievable light transmission (as judged by eye) is reached the more arduous alignment process involving a loupe (handleless magnifying glass) begins.

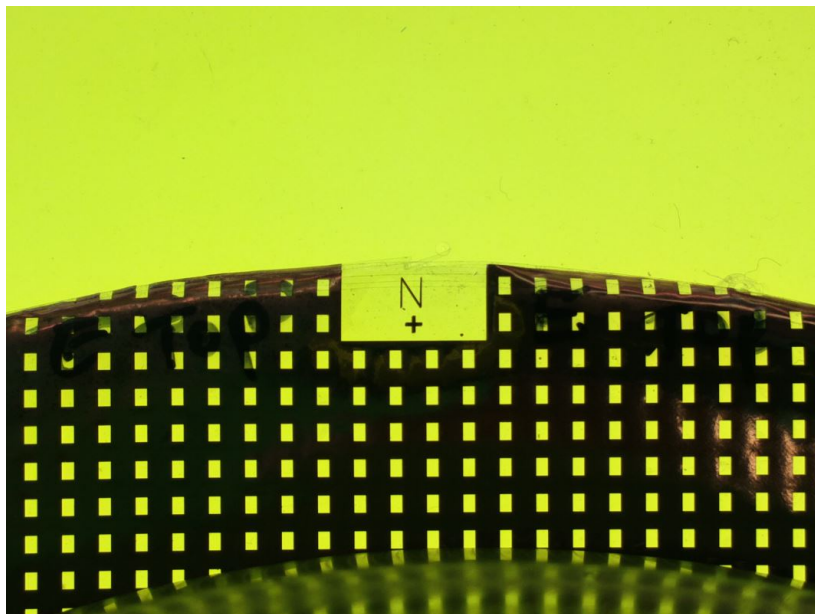


Figure 3.12: An example of an alignment mark.

another. However, in practice difficulties arose once the grids had been cut from their rings. The grids were no longer held taut and a small amount of shrinkage occurred. To give an example, the 21 cm diameter grids used in chapter 4 shrunk by  $\lesssim 1$  mm. This meant that in certain cases only two or three alignment marks could be overlapped perfectly. In this case and in cases where no alignment marks were present, the alignment was carefully inspected by eye at various locations around the grid using a loupe (handleless magnifying glass) until good alignment was achieved in as many places as possible but with emphasis on the central region.

Once alignment is finished, the grids are spot welded together using a soldering iron heated to 230 °C. This involves simply holding the soldering iron on a spot near the edge of the grids and away from the alignment marks until it has melted its way through to the plastic sheeting below. This welding prevents the grids from becoming misaligned later, either when more grids are aligned on top or when they are transported around the lab later on.

The above process is then repeated as many times as is required for the device being constructed. Once complete, preliminary lab measurements can be carried out on the device to ensure good performance before final hot pressing and bonding processes were carried out.

#### 3.3.2 Hot Pressing & Bonding

The bonding process began with placing the spot welded grids between two steel press plates with Teflon (PTFE) sheets separating the polypropylene and the surface of the press plates (figure 3.13). The press plates are held together with screws that are tightened prior to the transporting of the press plates from the workbench to the vacuum oven. Once in the vacuum oven, the screws are loosened to allow the polypropylene to expand when heated. If this step is not carried out, the total force of the expanding polypropylene is strong enough to bend the press plates (V. Haynes, personal communication, 2012). Finally, several weights are

### 3: MANUFACTURING METAMATERIALS

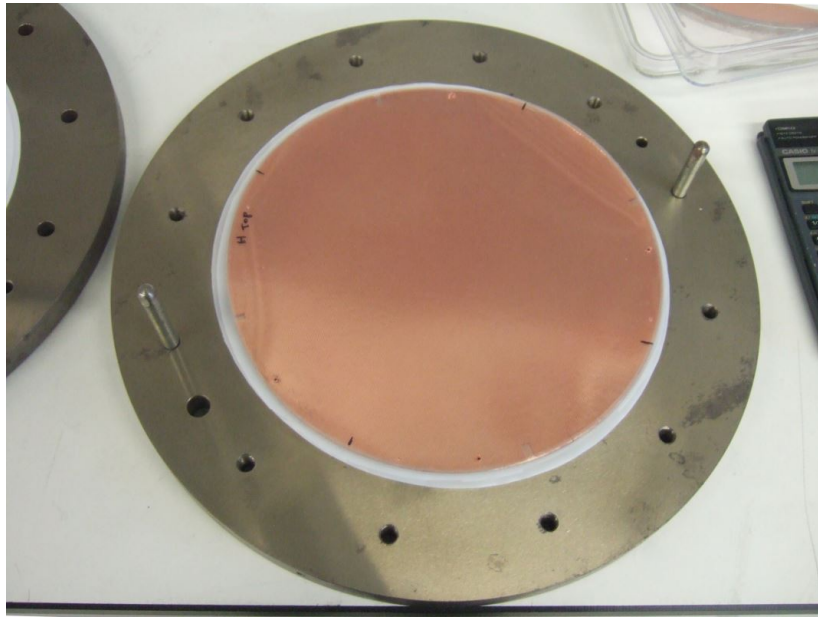


Figure 3.13: Spot welded sample to be bonded resting on teflon sheet and bottom press plate.

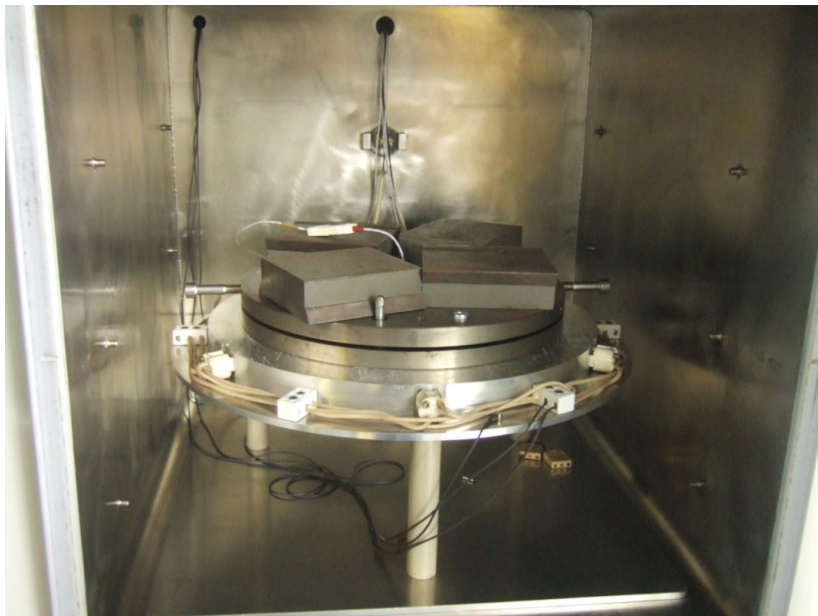


Figure 3.14: The inside of the vacuum oven. The sample is squashed between the two press plates that has the weights on top. The press plates are sat upon a heating element that gains its heat from the ring of halogen lamps inserted around its circumference (visible as white rectangles).

placed uniformly on the top press plate (figure 3.14) to provide more pressure to the grids. The temperature of the oven is monitored and controlled with a computer which records the temperature via a sensor placed in the middle of the top press plate.

Once the door is closed, the vacuum pump is activated to extract the air from within the oven. The press plates are heated conductively from below by a larger plate that is itself heated radiatively by small halogen lamps inserted around its circumference. The entire heating and cooling process can take up to 24 h, depending on the temperature profile chosen. The peak of the temperature profile was 161 °C although in some cases it could go as high as 200 °C.

The author carried out this stage for all the devices described in chapter 4 and chapter 5 except the first version of the Half Wave Plate (HWP).

### 3.4 Alternative Manufacturing Techniques

Other fabrication techniques for metamaterials have been reported in the scientific literature. In the majority of cases they exhibit some form of lithography to obtain the required geometry from the metallic components. Earlier metamaterial designs and the ones made to function at GHz frequencies used readily available printed circuit boards (PCBs) such as FR-4 or GML-1000 that were already laminated on one side with copper. Examples including Shelby et al. (2001b) and Houck et al. (2003) went down this route. In this case the fabrication process follows a similar procedure to the one outlined above apart from the substrate preparation and copper deposition. Even simpler methods were employed by Alici and Ozbay (2008) who used cardboard with aluminium based tape for the substrate and metallic features respectively to create a fishnet based metamaterial (figure 1.10f) that functioned at 21 GHz.

In this project to construct larger devices, individual layers were photolithographed first, then stacked and aligned. An alternative to this procedure is that

of multilayer lithography e.g. Paul et al. (2008). In this case, each subsequent layer is lithographed directly on top of the preceding layer. This requires highly accurate alignment as once the additional layers have been added, they cannot be realigned. In addition, as noted by Valentine et al. (2011), inaccuracies in the alignment of each layer build up as each new layer is added. When high alignment accuracy is possible, complicated metamaterial designs are possible using multilayer photolithography. Moser et al. (2009) created a self-supported metamaterial (which they referred to as a metafoil) where the final metallic structures exist as free standing meanderlines.

In the  $\geq 100$  THz frequency range, microlithography makes ways for nanolithography. This can be carried out in a similar way as the photolithography procedure described above but using beams of electrons to carry out the lithography rather than ultraviolet radiation. Named electron-beam lithography, this also dispenses the mask, with the photoresist instead being slowly etched and developed by an electron beam to create the nano-scaled sized structures required at these frequencies. Again, to construct multilayered structures, the lithography process would have to be carried on top of the previous layer. Alternatively, structures can instead be “milled” in a process known as focused ion beam milling, as used in Valentine et al. (2011). In this process, the desired structural thickness was prefabricated in a metal-dielectric-metal layering fashion. In Valentine et al. (2011)’s case a prism, using a fishnet based metamaterial design, was milled into a 10-layer thick stack of metal-dielectric-metal. With this technique, Valentine et al. were able to create structures with feature sizes as small as 30 nm.

# Chapter 4

## Artificial Dielectrics with Metamaterials

*What it is, is what it is.*

Troy Jamerson, 2007 June

### 4.1 Introduction

As described in chapter 1, metamaterials can be used to mimic the electromagnetic properties of regular materials. In this sense they can be considered “artificial dielectrics”. A large part of the interest generated by them since 2000 was their ability to produce negative refractive indices (NRI) and the possibilities this allowed. One of these is the possibility of the superlensing effect of a slab of material with a refractive index of  $-1$ .

In this chapter, we begin by deriving the equations of the parameter extraction method used to calculate the material parameters from reflection and transmission coefficients. The testing of the coded extraction method is then shown. Later, the process of designing and modelling a W-band (75 GHz to 110 GHz) NRI slab is described. The intended design for the NRI slab required that a modified

material parameter extraction method be developed and this is derived and tested. Finally, the first stages of the manufacturing of the NRI slab are described and lab measurements taken with the reduced structure are shown.

## 4.2 Material Parameter Extraction

To ascertain if a material has certain electromagnetic properties, such as the refractive index,  $n$ , impedance,  $Z$ , as well as the relative permittivity,  $\epsilon_r$  and relative permeability,  $\mu_r$ , a material parameter extraction method is required. The procedure adopted to extract these values are based on the Nicolson-Ross-Weir (NRW) method, detailed in the papers Nicolson and Ross (1970) and Weir (1974). The method uses the amount of radiation reflected from and transmitted through a material to calculate the material parameters. After the demonstration of NRI, Smith et al. (2002) applied this method to the determination of  $n$ ,  $Z$ ,  $\epsilon_r$  and  $\mu_r$  of a composite metamaterial structure. Further refinement of the method was introduced in Chen et al. (2004) and since then it has been the most widely used parameter extraction method for metamaterial researchers.

This method was popular due to its non-destructive nature and its reliance on the reflection and transmission coefficients that can be obtained relatively easily through both simulation and experiment, as opposed to e.g. the phase progression through the material.

The premise of the above methods is now derived.

### 4.2.1 Nicolson-Ross-Weir Method

Simulations and experiment take the form of figure 4.1 and figure 4.2 respectively, where a (meta)material under test (MUT) of (effective) thickness,  $d$ , refractive index,  $n$  and impedance,  $Z$ , normalised to the free space impedance,  $Z_0$ , is illuminated from one side by linearly polarised plane waves. The S-parameters, measured at a distance  $x_1$  and  $x_2$  from the (effective) surface of the (meta)material,

have their reference planes moved to the (effective) entrance and exit surfaces of the MUT.

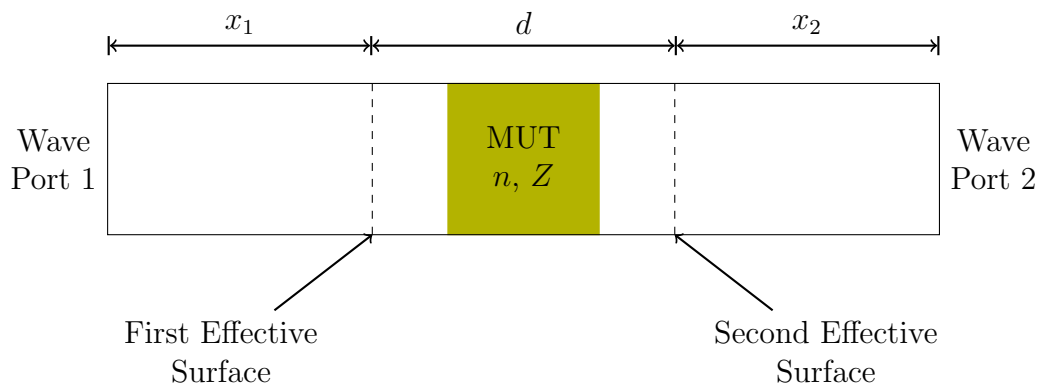


Figure 4.1: Side on view of the parameter extraction setup in HFSS simulations.

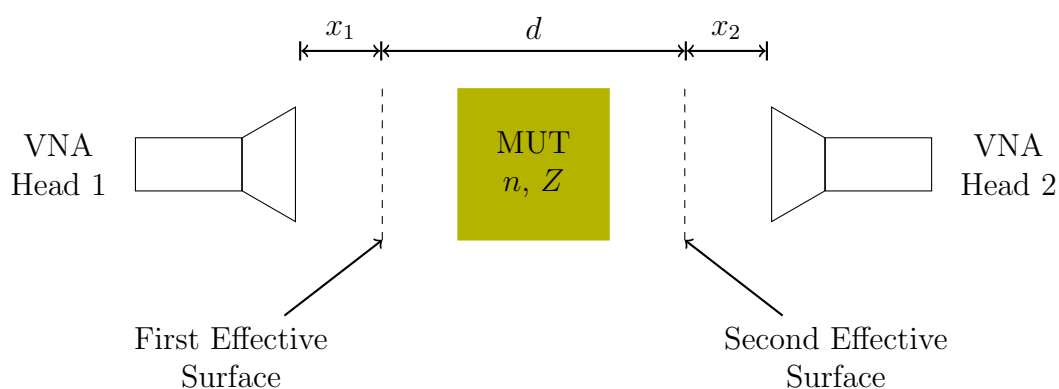


Figure 4.2: Schematic of an experimental equivalent to the parameter extraction setup shown in figure 4.1.

For radiation with  $\exp(+i\omega t)$  time dependence (the opposite of the time dependence used in equation (1.19)), the S-parameters  $S_{11}$  and  $S_{21}$  are given by:

$$S_{11} = \frac{\rho[1 - \exp(2ink_0d)]}{1 - \rho^2 \exp(2ink_0d)} \quad \text{and} \quad (4.1)$$

$$S_{21} = \frac{(1 - \rho^2) \exp(ink_0d)}{1 - \rho^2 \exp(2ink_0d)} \quad (4.2)$$

where  $\rho = (Z - 1)/(Z + 1)$ . Inverting these equations it is possible to obtain  $n$

and  $Z$  via the following equations:

$$\exp(ink_0d) = X \pm i\sqrt{1 - X^2} \quad (4.3a)$$

$$\text{where } X = \frac{1 - S_{11}^2 + S_{21}^2}{2S_{21}} \quad (4.3b)$$

$$Z = \pm \sqrt{\frac{(1 + S_{11})^2 - S_{21}^2}{(1 - S_{11})^2 - S_{21}^2}}. \quad (4.3c)$$

The signs of the square roots are chosen such that  $\text{Re}(Z) > 0$  and  $\text{Im}(n) < 0$ . These signs are chosen to satisfy the requirement that the MUT be a “passive medium” i.e. energy is dissipated to the MUT and not generated by it when radiation is transmitted through it. The refractive index itself is then calculated by rearranging equation (4.3a) to give

$$\text{Re}(n) = \frac{1}{k_0d} \left[ \text{Im} \left( \ln \left( X \pm i\sqrt{1 - X^2} \right) \right) + 2\pi m \right] \quad (4.4a)$$

$$\text{Im}(n) = \frac{1}{k_0d} \left[ \text{Re} \left( \ln \left( X \pm i\sqrt{1 - X^2} \right) \right) \right] \quad (4.4b)$$

where  $m$  is an integer known as the branch index. Whilst the imaginary part of  $n$  is uniquely determined, the same is not true for the real component due to what is known as the branching term,  $2\pi m$ . It arises from the multivalued property of taking a logarithm of a complex number. The correct value of  $m$  can be found by taking measurements of two different thicknesses of the MUT and finding the branch number that results in both thicknesses producing the same calculated value of  $n$ , because  $n$  should not vary with thickness.

This method has three drawbacks. First, the sign of the square roots must be determined in both equations (4.3a) and (4.3c). Secondly, the determination of the  $m$  requires measurements of multiple thicknesses of the MUT to be taken which may be inconvenient when dealing with experimental readings. Picking the correct branch can be difficult when the MUT is thick because as can be seen in equation (4.4a), when  $d$  increases, the spacing between the different branches

of  $\text{Re}(n)$  get smaller. Lastly, with regards to metamaterials, the definition of the effective thickness requires extra care. The effective thickness for regular materials is equal to their physical thickness. For metamaterials different definitions can be chosen ranging from the physical thickness of the unit cells, to a distance based on the periodicity of the unit cells that make up the structure.

### 4.2.2 Robust Parameter Extraction Method

Chen et al. (2004) made some improvements to deal with these problems. The first problem was improved by using an alternative form of equation (4.3a),

$$\exp(ink_0d) = \frac{1 - S_{11} \frac{Z-1}{Z+1}}{S_{21}} \quad (4.5)$$

where the sign of  $\exp(ink_0d)$  can be obtained directly once the sign for  $Z$  has been established. For the “branching problem” Chen et al. (2004) suggested an iterative method based on the Taylor series expansion of  $\exp(ink_0d)$  to calculate the value of  $\text{Re}(n)$  across the frequency. At the initial frequency point,  $f_0$ , possible values of  $m$  are determined via the inequality

$$|\text{Re}(n)\text{Im}(Z)| \geq \text{Im}(n)\text{Re}(Z). \quad (4.6)$$

The author found that the smallest positive value to satisfy the inequality was the correct branch. At the next frequency point,  $f_1$ ,  $\text{Re}(n)$  is found by solving

$$\exp[in(f_1)k_0(f_1)d] = \exp[in(f_0)k_0(f_0)d] \cdot \left[ 1 + \Delta + \frac{\Delta^2}{2} \right] \quad (4.7)$$

where  $\Delta = in(f_1)k_0(f_1)d - in(f_0)k_0(f_0)d$ . The only unknown in this equation is  $n(f_1)$  and can be easily solved from the quadratic equation:

$$n(f_1) = \frac{-b \pm \sqrt{b^2 - 4ac}}{2a} \quad (4.8)$$

where

$$a = -\frac{[k_0(f_1)d]^2}{2} \quad (4.9)$$

$$b = \frac{n(f_0)k_0(f_0)k_0(f_1)d^2}{2} - ik_0(f_1)d \quad (4.10)$$

$$c = 1 + in(f_0)k_0(f_0)d - \frac{[n(f_0)k_0(f_0)]^2d}{2} - \frac{\exp[-in(f_1)k_0(f_1)d]}{\exp[-in(f_0)k_0(f_0)d]}. \quad (4.11)$$

The correct root is found by comparing  $\text{Im}(n)$  calculated via equation (4.8) to that calculated via equation (4.5) and taking the one with the closest value.

According to Chen et al. (2004) the effective entrance and exit surfaces should be defined by the regions where the reflected and transmitted wave fronts are planar. The values of  $S_{11}$  and  $S_{21}$  are dependent on the locations of these surfaces and their values effect the value of  $Z$  via equation (4.3c). To locate these two surfaces Chen et al. (2004) devised an optimisation procedure where the location of the effective surfaces for two metamaterials of different thicknesses is varied. When the calculated impedances,  $Z_1$  and  $Z_2$ , of the first and second metamaterial are equal, the effective surfaces had been found. The cost function used for this optimisation that needed to be minimised was

$$\text{cost} = \frac{1}{N_f} \sum_{i=1}^{N_f} \frac{|Z_1(f_i, x_1, x_2) - Z_2(f_i, x_1, x_2)|}{\max(|Z_1(f_i, x_1, x_2)|, |Z_2(f_i, x_1, x_2)|)} \quad (4.12)$$

where  $N_f$  is the total number of frequency points,  $Z_{1,2}$  are the impedances of the first and second metamaterial calculated once the S-parameters' reference planes had been moved according to  $x_1$  and  $x_2$ .

A finding made by Chen et al. (2004) about the effective surfaces was that for "symmetric one-dimensional" metamaterials the effective entrance and exit surfaces were located in the same place as the physical entrance and exit surfaces. That was the case in the paper because the unit cell design they modelled was based on the SRR and Wire geometry where the periodicity and the physical thickness of the cell in the propagation direction were equal. Extending the idea

to planar metamaterial designs, authors began to use the periodicity to define the effective entrance and exit surfaces meaning that these surfaces would exist a certain distance away from the physical boundaries. In these papers e.g. Vallecchi et al. (2009) and Tung et al. (2010), the transmission and reflection data used to calculate the refractive index are based on simulations of a single unit cell with the periodicity defined by the authors of these papers. It is then supposed that the refractive index behaviour of this single cell is equivalent to that of many cells cascaded by the defined periodicity. In effect, behaving as a bulk material, because a material's parameters are independent of its thickness.

In actual fact, depending on the periodicity, the value of the calculated refractive index can change as more cells are added in cascade. It will continue to change until it “converges”, whereupon the addition of more cells has no further effect on the value. An analogy from Valentine et al. (2011), is that this is akin to the material properties of many layers of graphene converging to match those of graphite. The number of cells required for the convergence depends on the unit cell periodicity.

Work carried out in Zhou et al. (2008, 2009) showed that for “weakly coupled” metamaterials where periodicity of the cascaded unit cells is larger than their physical thickness (figure 4.3a), convergence can be easily achieved. The difference between the calculated refractive indices of one unit cell and two cascaded unit cells decreased as the periodicity was increased. If the periodicity was large enough then the convergence could be reached with only a single unit cell i.e. the calculated  $n$  for a single unit cell is equal to the  $n$  for two cascaded unit cells. “Tightly coupled” metamaterials where the metamaterial cells are in physical contact with one another (figure 4.3b), as was the case of Zhou et al. (2009), required at least three unit cells (or seven layers in the papers nomenclature) to converge. There was a large difference between the value of  $\text{Re}(n)$  calculated from one cell and the converged value (figure 4.4) showing how much of an effect coupling between unit cells can have on the refractive index.

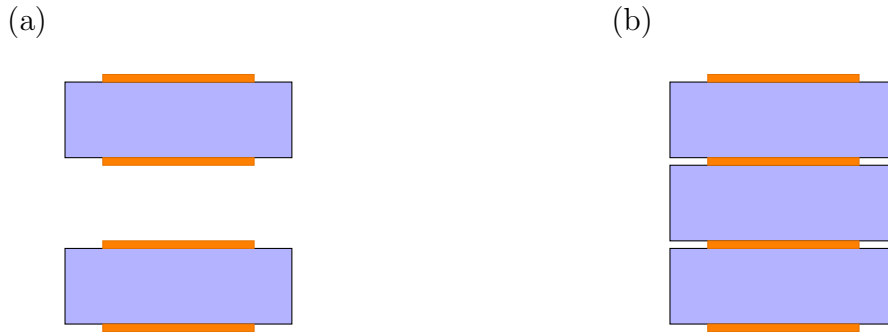


Figure 4.3: (a) Weakly coupled metamaterial setup. (b) Strongly coupled metamaterial setup. The metallic components are coloured orange. The substrate is coloured blue.

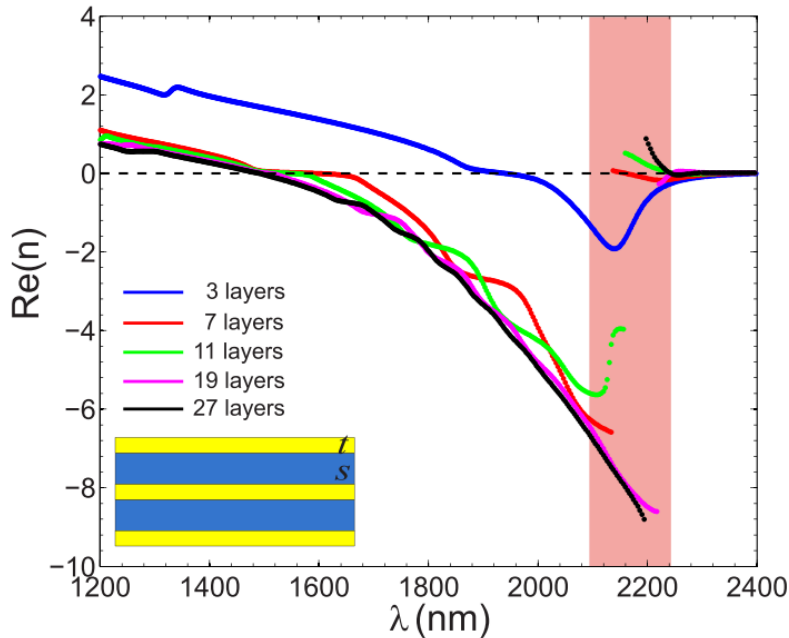


Figure 4.4: Graph taken from Zhou et al. (2009, figure 4) showing the refractive index calculated for different numbers of cascaded “tightly coupled” metamaterial unit cells based on a fishnet design (figure 1.10e). Zhou et al. (2009) uses the nomenclature of layers where each layer of metal and substrate is counted individually, so three layers corresponds with one unit cell in this thesis, seven layers with two unit cells etc. As can be seen, the refractive index for three layers (blue line) differs greatly from that calculated from many cascaded cells. The pink bar marks the location of a discontinuity in  $Re(n)$  the authors observed. Note that the  $x$ -axis is wavelength rather than frequency as in every other graph in this thesis.

Once convergence in the refractive index has been reached, the calculated value of  $n$  becomes a “bulk” material parameter more akin to the refractive indices of regular materials in that its value is independent of the (meta)materials thickness. What this means in practice is that the  $\text{Re}(n)$  calculated from single unit cell data are merely indicative of the bulk properties but should not be assumed to be equal to them. Indeed, as the refractive index calculation relies on the knowledge of the periodicity of the metamaterial cell, when a single unit cell is modelled in isolation, authors are free to specify an effective thickness of their choosing.

### 4.2.3 Testing of Material Parameter Extraction Method

The testing of the extraction method took the form of the author running HFSS simulations of blocks of materials and metamaterial geometries from papers and comparing the results to check whether or not the method the author had codified with MATLAB worked.

From the HFSS materials library, silicon and water were chosen. Author defined materials such as polypropylene and what will be referred to as the Imaginary Negative Material (INM) were also included. The material properties for these material are given in table 4.1. The blocks of material simulated had side lengths of 5 mm and had thicknesses,  $d$ , of 0.8 mm, 2 mm and 3 mm in the  $z$ -direction. The wave port and PEPH setup with symmetry boundaries, as described in section 2.2.2 and section 2.2.3, were used as the excitation and boundary conditions. The port distance,  $d_{\text{port}}$ , was 5 mm (figure 4.5). An interpolating frequency sweep was made from 10 GHz to 60 GHz with solution frequency set to 48 GHz.

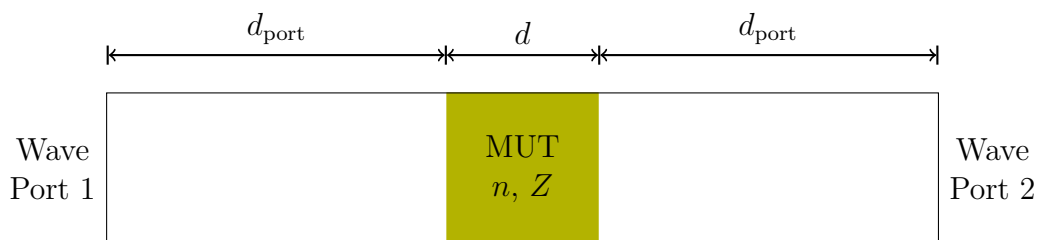


Figure 4.5: Schematic of the HFSS setup for the parameter extraction test.

Table 4.1: Material properties of the blocks simulated in HFSS to test the material parameter extraction method. The values for silicon and water (distilled) were from HFSS’s internal library of material parameters. Polypropylene (PP) was taken from Lamb (1996). Imaginary Negative Material (INM) was created for this project.

Material	Relative Permittivity, $\epsilon_r$	Dielectric Loss Tangent, $\delta$	Bulk Conductivity, $\sigma$	Relative Permeability, $\mu_r$	Refractive Index, $n$
Silicon	11.9	0	0	1	3.45
Water	81	0	0.0002	0.999 991	9.00
PP	2.2551	0.0007	0	1	1.50
INM	-2	0	0	-3	-2.45

During this testing phase, certain issues arose. The primary being the different time dependencies used for the radiation in Chen et al. (2004) and HFSS. The former used  $\exp(-i\omega t)$  whilst the latter used  $\exp(+i\omega t)$ . The most obvious discrepancy this caused was the incorrect signs of the final values of  $n$ . Other differences that were later corrected for included the reversal of the inequality used to choose the correct branch as well as the quadratic equation that needed solving in the iterative step. The equations shown in sections 4.2.1 and 4.2.2 have this taken into account.

#### 4.2.3.1 Effective Surface

First the section of the code that dealt with finding the effective surfaces was tested. The expected result was that the values of  $x_1$  and  $x_2$  would equal  $d_{\text{port}}$  i.e. the reference planes had been moved to the blocks surfaces hence equating the effective thickness to the physical thickness. The differential evolution (Storn and Price 1997) method implemented in MATLAB using code written by Markus Buehren<sup>1</sup> was used to optimise the values of  $x_1$  and  $x_2$  to minimise the value of the cost function shown in equation (4.12).

<sup>1</sup><http://www.mathworks.com/matlabcentral/fileexchange/18593>

Table 4.2: The final values of  $x_1$  and  $x_2$  from the optimisation. All the values are very close to the expected value of  $d_{\text{port}}$  or 5 mm.

MUT One	MUT Two	$x_1$ [mm]	$x_2$ [mm]	Minimised Cost
0.8 mm Silicon	3 mm Silicon	4.999 94	4.999 93	0.008 332
2 mm Silicon	3 mm Silicon	4.999 98	4.999 98	0.007 908
0.8 mm H2O	3 mm H2O	4.999 93	4.999 95	0.014 238
2 mm H2O	3 mm H2O	4.999 96	4.999 94	0.014 479
0.8 mm PP	3 mm PP	5.000 1	5.000 06	0.000 387
2 mm PP	3 mm PP	5.000 05	5.000 14	0.000 855
0.8 mm INM	3 mm INM	4.997 03	4.999 7	0.003 687
2 mm INM	3 mm INM	4.997 2	5.000 06	0.005 022

The final results are shown in table 4.2 and it can be seen that the optimised distances the S-parameters' reference planes were moved by are very close to 5 mm. The surface plot in figure 4.6 shows the variation of the cost function (equation (4.12)) between the different deembd distances for 2 mm and 3 mm of water. The minimum cost is located where  $x_1$  and  $x_2$  take the value of  $d_{\text{port}}$ , 5 mm.

Cost Function of 2 mm and 3 mm of Water

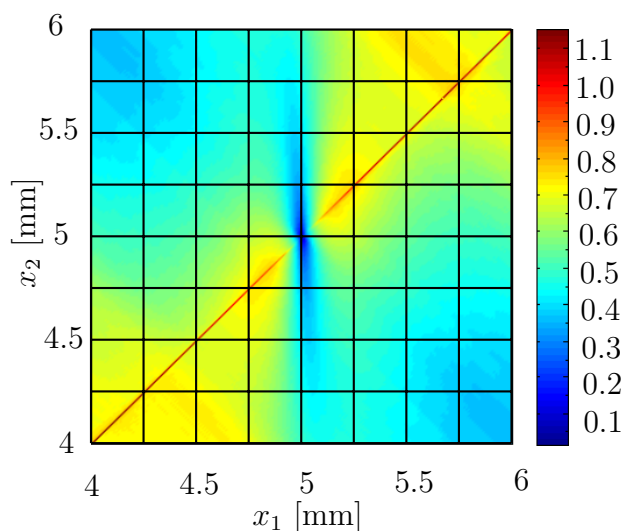


Figure 4.6: Surface plot of the cost function, equation (4.12), between 2 mm and 3 mm thick blocks of water. The minimum cost is located at  $x_1 = x_2 = d_{\text{port}} = 5$  mm. Values of  $x_{1,2}$  greater than 5 mm correspond to a reference plane *inside* the block of water.

### 4.2.3.2 Refractive Index

The S-parameters' reference planes were moved to the blocks' surfaces, based on the results from section 4.2.3.1. The values of  $n$ ,  $\varepsilon_r$  and  $\mu_r$  were subsequently calculated and compared to the input parameters in table 4.1. An initial branch number of  $m = 0$  was chosen at 10 GHz, at the start of the iterative sweep. This seemed a reasonable assumption given that the thicknesses of the blocks were all less than the wavelength of the starting frequency. Indeed, this assumption was sufficient for all samples except the 2.0 mm and 3.0 mm thick blocks of water where the initial branch number was  $m = 1$ . The calculated refractive indices of the 0.8 mm, 2.0 mm and 3.0 mm thick blocks of silicon are shown in figure 4.7. The lines of the real and imaginary parts for all three thicknesses overlap as expected and they do so at 3.45. Similarly, the calculated  $n$ ,  $\varepsilon_r$  and  $\mu_r$  of the 0.8 mm test materials, are shown in figures 4.8 to 4.10, all agree with the values from table 4.1.

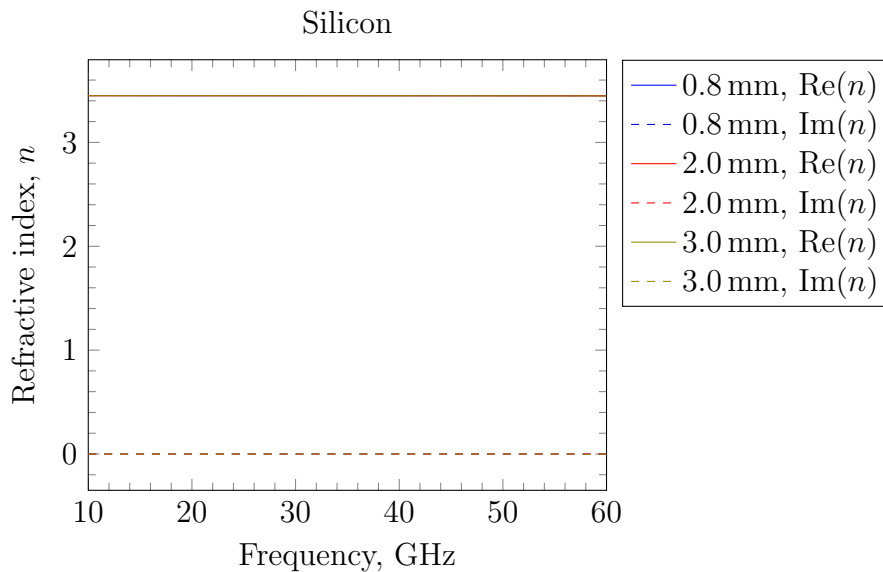


Figure 4.7: Calculated values of silicon's refractive index based on  $S_{11}$  and  $S_{21}$  data from HFSS simulations. The lines overlap, as expected, indicating that the coded algorithm works.

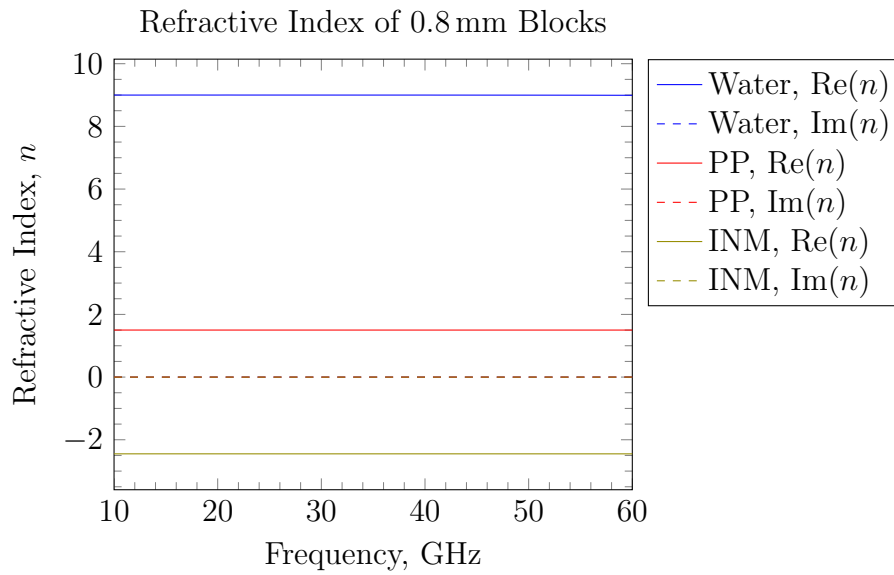


Figure 4.8: The calculated refractive index,  $n$ , of the 0.8 mm blocks of water, polypropylene (PP) and imaginary negative material (INM).

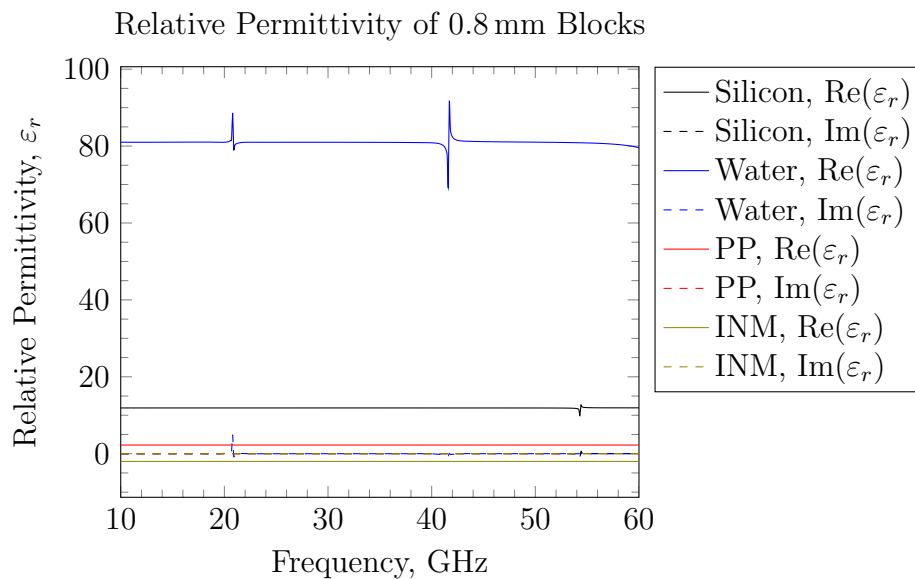


Figure 4.9: The calculated relative permittivity,  $\epsilon_r$ , of the 0.8 mm blocks of silicon, water, polypropylene (PP) and imaginary negative material (INM).

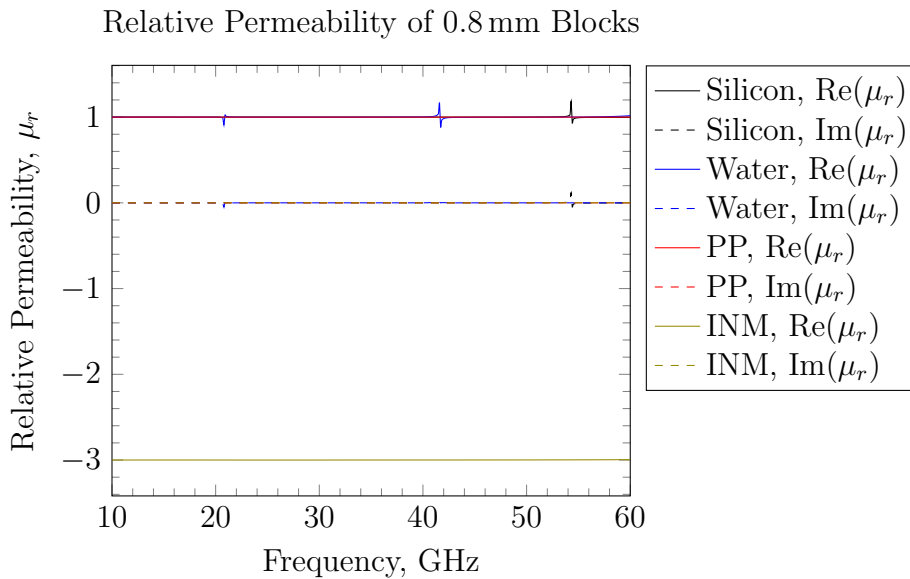


Figure 4.10: The calculated relative permeability,  $\mu_r$ , of the 0.8 mm blocks of silicon, water, polypropylene (PP) and imaginary negative material (INM).

### 4.3 Negative Refractive Index Slab

The work that went into designing and manufacturing a photolithographed W-band negative refractive index slab is described within this section.

#### 4.3.1 NRI Block Design & Modelling

From the available literature it was noticed that the fishnet geometry (figure 1.10e and figure 1.10f) was a popular geometry to use for designing and creating bulk planar negative refractive index metamaterials. Examples of its use have been reported at radio (e.g. Alici and Ozbay (2008); Zaoui et al. (2012)) as well as infrared (e.g. Zhou et al. (2009); Valentine et al. (2011)) frequencies. In papers relating to the construction of NRI blocks at radio frequencies, the construction of the blocks consist of individual layers made of metallic fishnet grids and dielectric substrate. These layers are then separated by air gaps.

It was decided that the design of this project's NRI block would be "embedded" within polypropylene as opposed to creating an air gap structure. The advantages

of going down such a route includes the structural stability provided to the grids by restricting their ability to move and become misaligned after bonding. In addition to embedding, the block would be “sandwiched” between polypropylene sheets to create a slab. This step improves the impedance matching between the NRI block and the air, improving overall transmission. The result of these two design choices means that no copper grids are exposed to air in the final structure, eliminating the possibility of the copper becoming oxidised and effecting the final performance of the device.

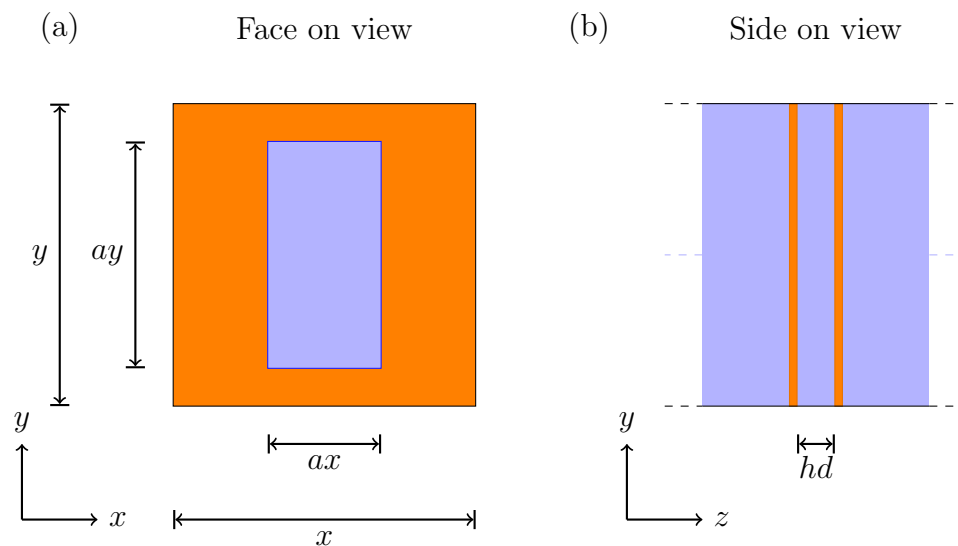


Figure 4.11: (a) Face on view of this fishnet design’s unit cell. (b) Side view. The dashed lines are to indicate that that polypropylene substrate continues on to the sides because the fishnet was designed and optimised within an infinite medium of polypropylene. The dimensions are listed in the main text. Copper is coloured orange and the polypropylene is coloured blue.

The fishnet design used in this project was inspired by one used in Mary et al. (2008) whose unit cell is shown in figure 4.11. The paper describes a theoretical study of a simplified fishnet design consisting of fishnet grids made from a Perfect Electric Conductor (PEC) separated by a vacuum gap of the same thickness as the fishnet grid. The author adapted the design by: 1) Scaling the dimensions so it would function within the W-band, 2) Replacing the PEC (infinite conductivity)

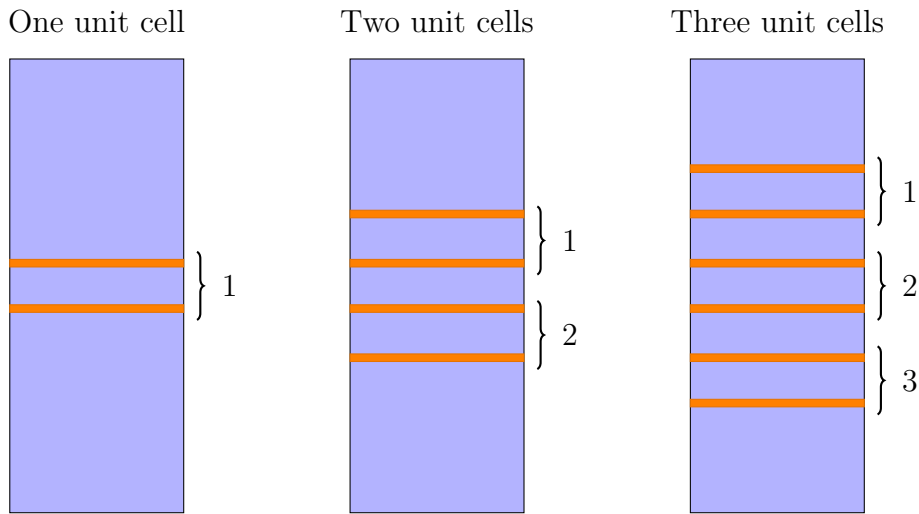


Figure 4.12: Side on view drawing to show how the embedded unit cells are arranged when cascaded. Each unit cell is composed of a pair of grids as denoted by the braces. The orange represents the metallic grids and the blue is the dielectric within which the grids are embedded.

with copper (finite conductivity:  $58 \times 10^6 \text{ S m}^{-1}$ ), 3) Reducing the thickness of the metal fishnets from the scaled value of  $134 \mu\text{m}$  to  $2 \mu\text{m}$  and 4) Replacing the vacuum with polypropylene. HFSS simulations were set up with one, two, six and seven unit cells with the air box volume filled with polypropylene. This was done to ensure that the calculated refractive index did indeed converge as more unit cells were cascaded and also give a better idea as to where the  $n = -1$  region was located so that further optimisation could be carried out accordingly. The simulation with six cascaded unit cells was done because it was expected that with this many cells, convergence should have been reached. The further simulation with seven cascaded unit cells served as a check to confirm convergence of the calculated refractive index. Using the same nomenclature used in figure 4.11 the initial W-band design had dimensions of:  $x = y = 1.78 \mu\text{m}$ ,  $ax = 600 \mu\text{m}$ ,  $ay = 890 \mu\text{m}$  and  $hd = 94 \mu\text{m}$  and produced a negative refractive index of  $-1$  at  $100 \text{ GHz}$  for radiation polarised along the  $x$ -axis. The calculated  $\text{Re}(n)$ 's and  $\text{Im}(n)$ 's are shown in figures 4.13 and 4.14 respectively. It is clear that as more cells

### 4.3: NEGATIVE REFRACTIVE INDEX SLAB

are added, the refractive indices converge upon a unique value at each frequency point and much like the findings of Zhou et al. (2009) shown in figure 4.4, it demonstrates the large difference that can occur between the calculated refractive index for a single unit cell and several unit cells. The physical thickness (defined as the distance between the outward facing copper surfaces of the outermost grids) was used in the calculations of  $n$  as the location of reference planes that minimised equation (4.12) corresponded very closely to this value. For example, in an optimisation between six and seven unit cells the values of  $x_1$  and  $x_2$  were  $-3.11 \times 10^{-7}$  and 0 respectively. The thicknesses of one, two, six and seven unit cells were respectively: 98  $\mu\text{m}$ , 294  $\mu\text{m}$ , 1078  $\mu\text{m}$  and 1274  $\mu\text{m}$ . Given these results, the physical thickness was used for the rest of this part of the project to calculate the refractive index of the fishnet grids.

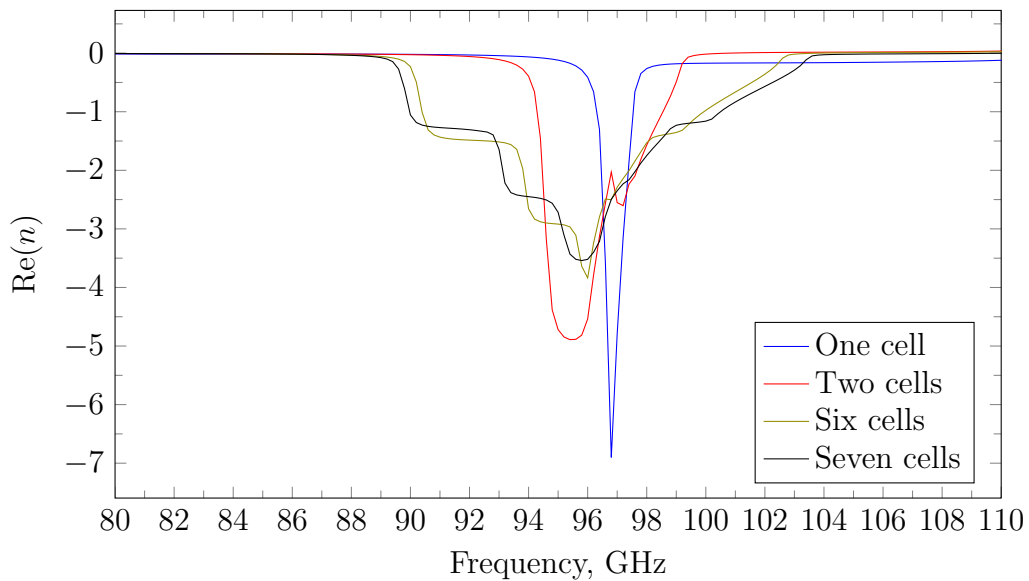


Figure 4.13: Convergence of  $\text{Re}(n)$  of the first fishnet design.

Owing to the nature of the negative index slab, to observe superlensing at mm-wavelengths with the available equipment would require a slab  $\sim 1$  mm thick and placement of horns very close to slabs surface which requires high accuracy. To make such readings easier it was decided that the fishnet geometry should be scaled up in size to reduce the frequency where  $n = -1$  occurs. This resulted in a

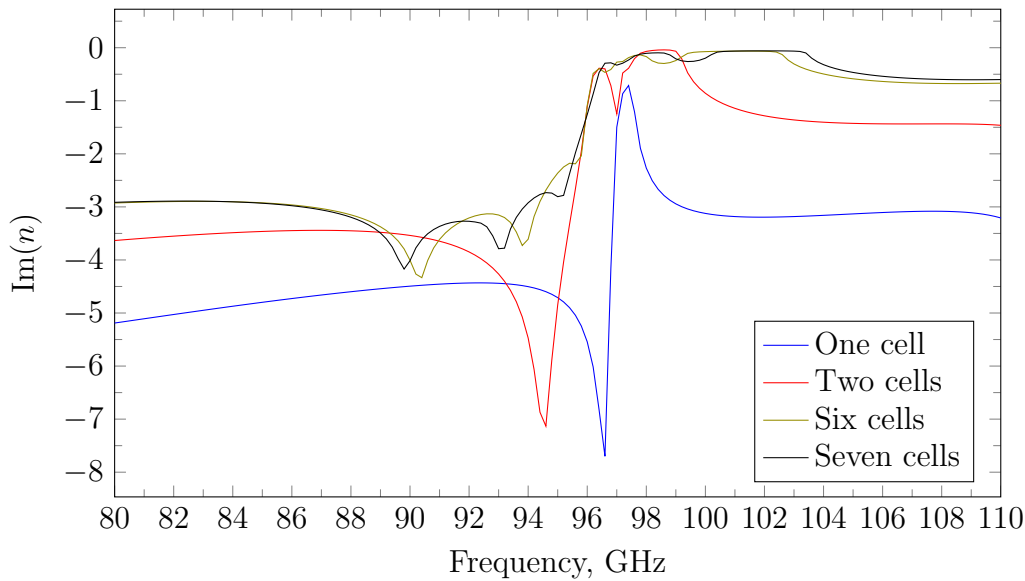


Figure 4.14:  $\text{Im}(n)$  of the first fishnet design with various numbers of cascaded unit cells.

second version of the fishnet design, whose dimensions were reached by multiplying the sizes of the original grid by a factor, equal to the ratio between the original  $94\ \mu\text{m}$  substrate thickness to the next largest available thickness,  $114\ \mu\text{m}$ . The final dimensions of the fishnet grid became:  $x = y = 2160\ \mu\text{m}$ ,  $ax = 728\ \mu\text{m}$ ,  $ay = 1080\ \mu\text{m}$  and  $hd = 114\ \mu\text{m}$ .

The plots of  $\text{Re}(n)$  and  $\text{Im}(n)$  against frequency reported in figures 4.15 and 4.16 respectively show that, as before,  $\text{Re}(n)$  converges as more cells are added. To emphasise this a HFSS simulation of 21 cascaded cells was carried out as well. This also served as a precursor to the modelling of a negative index slab of the same thickness. Using the twenty-one unit cell data,  $n_x = -1$  at 82 GHz. The physical thicknesses of the one, two, six, seven and twenty-one cells in the HFSS model were respectively:  $118\ \mu\text{m}$ ,  $354\ \mu\text{m}$ ,  $1298\ \mu\text{m}$ ,  $1534\ \mu\text{m}$  and  $4838\ \mu\text{m}$ . At this point it was noticed there was an error in the CAD model of the cascaded unit cells in HFSS that resulted in every other gap between the fishnet grids being  $2\ \mu\text{m}$  larger than they were meant to be. The intended thicknesses of the two, six, seven and twenty-one unit cells were:  $350\ \mu\text{m}$ ,  $1278\ \mu\text{m}$ ,  $1510\ \mu\text{m}$  and  $4758\ \mu\text{m}$ . Given the

relatively small increase this had on the intended total physical thickness ( $\sim 1\%$ ) the effects were not deemed substantial enough to invalidate the previously stated findings. Subsequent modelling of the twenty-one unit cell had this error corrected.

The transmitted intensities,  $|S_{21}|^2$ , of the  $x$  polarised radiation is shown in figure 4.17. As more cells are added the transmission exhibits more resonances and the overall peak transmission is reduced. At the lower end of the frequency sweep below 79 GHz, the transmitted intensities are practically zero.

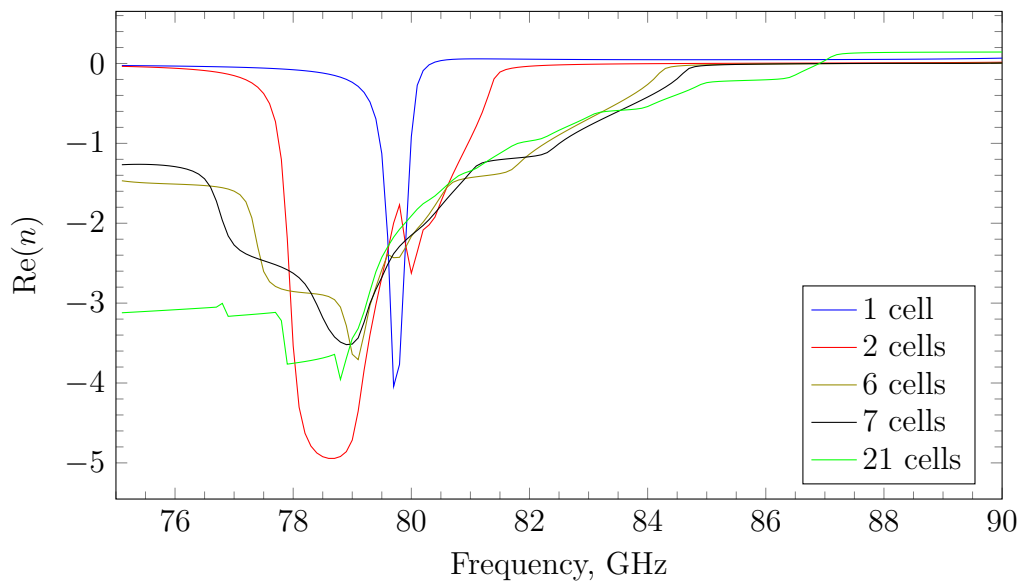


Figure 4.15: Convergence of  $\text{Re}(n)$  of the second fishnet design.

The reflected intensities,  $|S_{11}|^2$ , and absorption,  $1 - |S_{11}|^2 - |S_{21}|^2$ , are shown in figure 4.18 and figure 4.19 respectively. It is seen that the high reflections are the cause for the low transmission below 79 GHz.

Satisfied that the twenty-one cell model could produce a negative refractive index, work began on optimising the thicknesses of the polypropylene that would be used to sandwich the NRI block to create a slab. The need for having an extra thickness of polypropylene covering the outer faces is discussed at the beginning of section 4.3.1. Before this could be done however, a modification to the parameter extraction method was required.

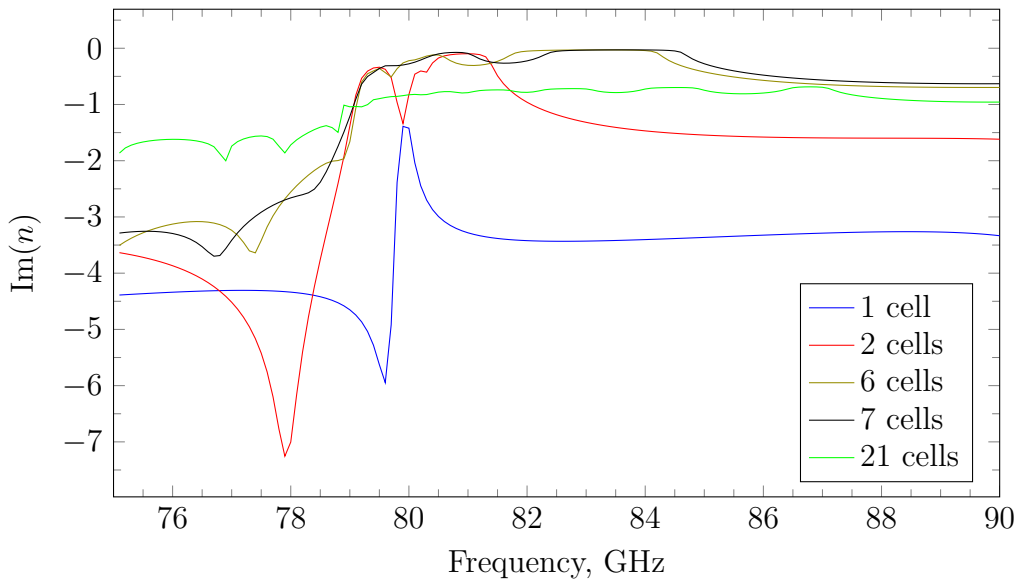


Figure 4.16:  $\text{Im}(n)$  of the second fishnet design with various numbers of cascaded unit cells.

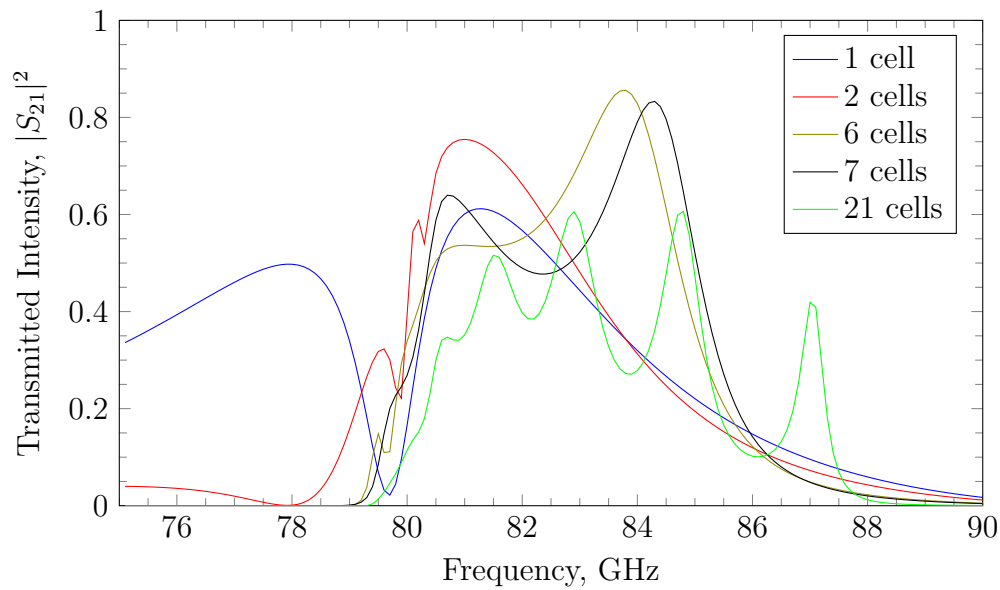


Figure 4.17: The transmitted intensity of the second fishnet design.

### 4.3.2 Modified Parameter Extraction Method

The parameter extraction method from section 4.2.1 only handles the case where the MUT is within an infinite uniform medium such as air and the S-parameters are measured from this medium. In this case however, the metamaterial is embedded

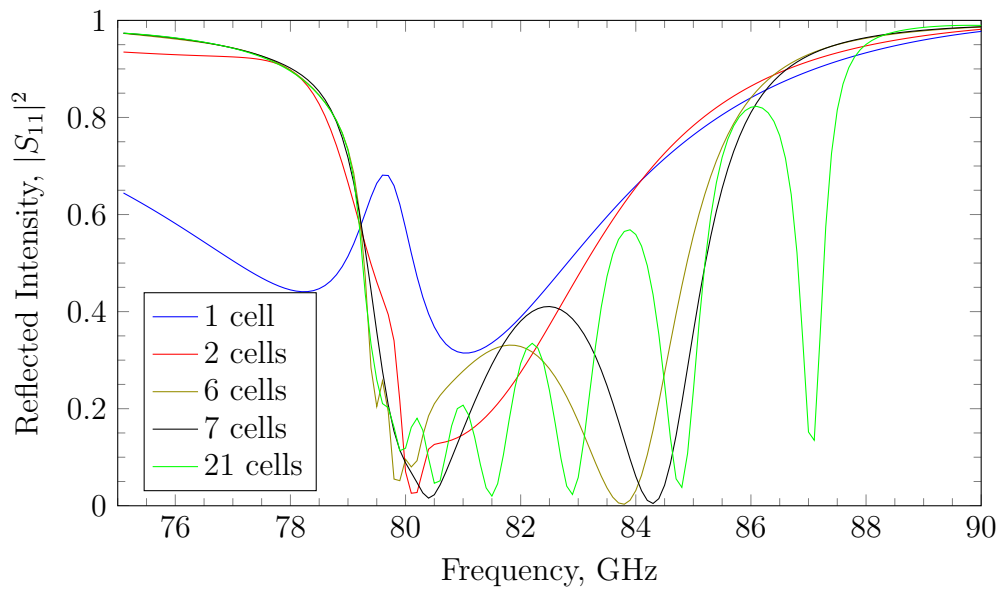


Figure 4.18: The reflected intensity of the second fishnet design.

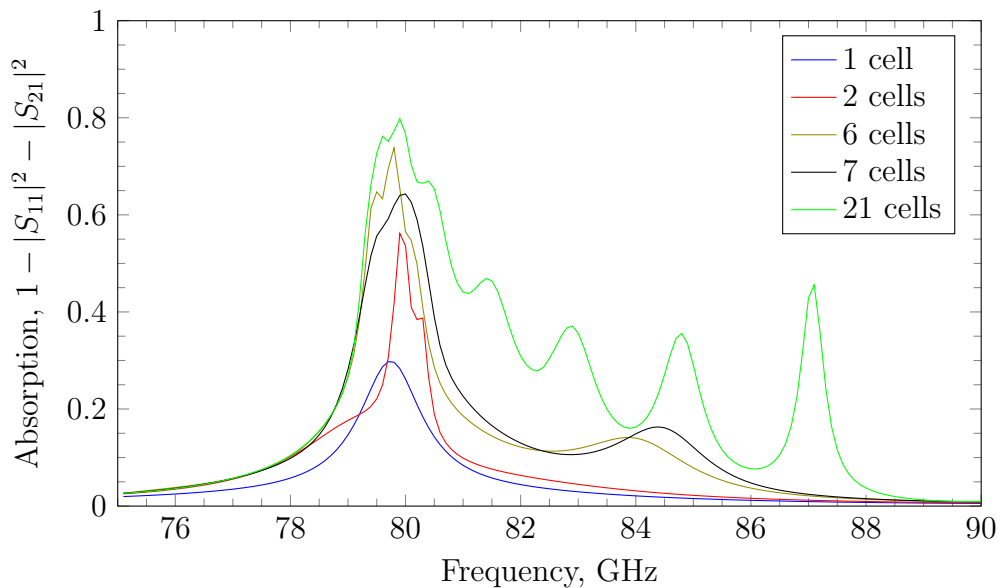


Figure 4.19: The absorption of the second fishnet design.

within a finite thickness of polypropylene, as drawn in figure 4.20. To use the retrieved  $S_{11}$  and  $S_{21}$  measured in air with such a slab would provide an average refractive index of the slab as a whole, whereas we require the refractive index of the block embedded within the polypropylene. Therefore, a modified parameter extraction was derived by the author to be able to extract the refractive index of

just the metamaterial when it is placed within a finite thickness of polypropylene from the S-parameters measured in air.

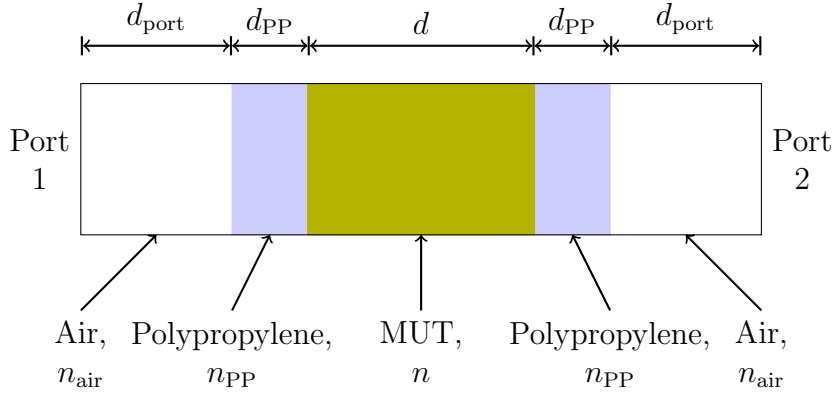


Figure 4.20: Schematic of the modified parameter extraction setup.

To proceed,  $S_{11}$  and  $S_{21}$ , for the above setup shown in figure 4.20 were calculated using the TL matrices discussed in section 2.4. The resulting TL matrix equation took the form

$$\begin{bmatrix} E_{1+} \\ E_{1-} \end{bmatrix} = M_1 \cdot P_1 \cdot M_2 \cdot P_2 \cdot M_3 \cdot P_1 \cdot M_4 \begin{bmatrix} E_{2+} \\ E_{2-} \end{bmatrix}, \quad (4.13)$$

where the matrices  $M_1$ ,  $P_1$  etc. are given in table 4.3 along with a description of their role in equation (4.13). The Fresnel coefficients used in equations (4.15) to (4.20) shown in table 4.3 are equal to

$$\begin{aligned} \rho_1 &= \frac{1 - n_{PP}}{1 + n_{PP}} & \tau_1 &= 1 + \rho_1 \\ \rho_2 &= \frac{Z - Z_0}{Z + Z_0} & \tau_2 &= 1 + \rho_2 \\ \rho_3 &= -\rho_2 & \tau_3 &= 1 + \rho_3 \\ \rho_4 &= -\rho_1 & \tau_4 &= 1 + \rho_4 \end{aligned}. \quad (4.14)$$

The resulting derivations and simplifications (especially of equations (4.22) and (4.23)) proved too difficult to be done correctly by hand. Instead, Mathemat-

Table 4.3: The matrices used in equation (4.13). The Fresnel coefficients are defined in the main text in equation (4.14).

Matrix		Description
	$M_1 = \frac{1}{\tau_1} \begin{bmatrix} 1 & \rho_1 \\ \rho_1 & 1 \end{bmatrix} \quad (4.15)$	$M_1$ is the matching matrix going from air to polypropylene.
	$P_1 = \begin{bmatrix} \exp(in_{PP}k_0d_{PP}) & 0 \\ 0 & \exp(-in_{PP}k_0d_{PP}) \end{bmatrix} \quad (4.16)$	$P_1$ is the propagation matrix through the outer polypropylene layers.
	$M_2 = \frac{1}{\tau_2} \begin{bmatrix} 1 & \rho_2 \\ \rho_2 & 1 \end{bmatrix} \quad (4.17)$	$M_2$ is the matching matrix between the polypropylene and the MUT.
	$P_2 = \begin{bmatrix} \exp(ink_0d) & 0 \\ 0 & \exp(-ink_0d) \end{bmatrix} \quad (4.18)$	$P_2$ is the propagation matrix for the MUT.
	$M_3 = \frac{1}{\tau_3} \begin{bmatrix} 1 & \rho_3 \\ \rho_3 & 1 \end{bmatrix} \quad (4.19)$	$M_3$ is the matching matrix between the MUT and the polypropylene.
	$M_4 = \frac{1}{\tau_4} \begin{bmatrix} 1 & \rho_4 \\ \rho_4 & 1 \end{bmatrix} \quad (4.20)$	$M_4$ is the matching matrix going from polypropylene back to air.

$\text{ica}^2$  was used instead to continue on. Using it,  $S_{11}$  and  $S_{21}$  were found to be equal to

$$S_{11} = \frac{E_{1-}}{E_{1+}} = \frac{A}{\exp(i2nk_0d) (\text{eip}^2 + \rho_1\rho_2)^2 - (\text{eip}^2\rho_2 + \rho_1)^2} \quad (4.21a)$$

$$S_{21} = \frac{E_{2+}}{E_{1+}} = \frac{\exp(ink_0d)\text{eip}^2(\rho_1 - 1)(\rho_1 + 1)(\rho_2 - 1)(\rho_2 + 1)}{\exp(i2nk_0d) (\text{eip}^2 + \rho_1\rho_2)^2 - (\text{eip}^2\rho_2 + \rho_1)^2} \quad (4.21b)$$

where

<sup>2</sup><https://www.wolfram.com/mathematica/>

$$A = \rho_1 \left[ \exp(i2nk_0d) (\text{eip}^4 + \rho_2^2) + \text{eip}^4 (-\rho_2^2) - 1 \right] \\ + (\exp(i2nk_0d) - 1) \text{eip}^2 \rho_1^2 \rho_2 + (\exp(i2nk_0d) - 1) \text{eip}^2 \rho_2 \quad (4.21c)$$

and

$$\text{eip} = \exp(in_{\text{PP}}k_0d_{\text{PP}}). \quad (4.21d)$$

These two equations were then solved for  $\exp(ink_0d)$  and  $Z$  and simplified, again, using Mathematica. For the impedance this results in

$$Z = \frac{\sqrt{B}}{n_{\text{PP}}C} \quad (4.22a)$$

where

$$B = [\text{eip}^4 ((n_{\text{PP}}S_{11} + n_{\text{PP}} + S_{11} - 1)^2 - (n_{\text{PP}} + 1)^2 S_{21}^2) \\ - ((n_{\text{PP}} - 1)S_{11} + n_{\text{PP}} + 1)^2 + (n_{\text{PP}} - 1)^2 S_{21}^2]^2 \\ - 64\text{eip}^4 n_{\text{PP}}^2 S_{21}^2 \quad (4.22b)$$

and

$$C = (\text{eip}^2(n_{\text{PP}}S_{11} + n_{\text{PP}} + S_{11} - 1) - n_{\text{PP}}(S_{11} + 1) + S_{11} - 1)^2 \\ - S_{21}^2 (\text{eip}^2(n_{\text{PP}} + 1) - n_{\text{PP}} + 1)^2. \quad (4.22c)$$

For the  $\exp(ink_0d)$  we obtain

$$\exp(ink_0d) = \frac{1}{8\text{eip}^2 n_{\text{PP}} S_{21}} \left[ - (\text{eip}^4 - 1) n_{\text{PP}}^2 (S_{11} - S_{21} + 1)(S_{11} + S_{21} + 1) \right. \\ - \left[ (\text{eip}^4 ((n_{\text{PP}}S_{11} + n_{\text{PP}} + S_{11} - 1)^2 - (n_{\text{PP}} + 1)^2 S_{21}^2) \right. \\ - \left. \left. ((n_{\text{PP}} - 1)S_{11} + n_{\text{PP}} + 1)^2 + (n_{\text{PP}} - 1)^2 S_{21}^2)^2 - 64\text{eip}^4 n_{\text{PP}}^2 S_{21}^2 \right]^{1/2} \right. \\ \left. + 2 (\text{eip}^4 + 1) n_{\text{PP}} (S_{11}^2 - S_{21}^2 - 1) + (\text{eip}^4 - 1) ((S_{11} - 1)^2 - S_{21}^2) \right] \quad (4.23)$$

from which  $n$  can be calculated.

To test the final equations, a HFSS simulation was set up with 3 mm of silicon

( $n_{\text{Si}} = 3.45$ ) with 1.426 mm of polypropylene on each side and 5 mm of vacuum separating the polypropylene and the wave ports (figure 4.20). The thickness of polypropylene was chosen to be equal to  $\lambda_{\text{PP}}/4$  at the centre of the frequency sweep, 35 GHz.  $\lambda_{\text{PP}}$  is the wavelength of radiation within polypropylene and is equal to the free space wavelength,  $\lambda_0$ , divided by the  $n_{\text{PP}}$ . An interpolating frequency sweep was then made from 10 GHz to 60 GHz, with the solution frequency set at 48 GHz. After moving the S-parameters' reference planes to the polypropylene surface, the  $S_{11}$  and  $S_{21}$  were extracted, used in the equation (4.23) and the results compared to the expected value of  $n = 3.45$ . As can be seen in figure 4.21 the output refractive index did indeed equal 3.45 across the entire band, as expected.

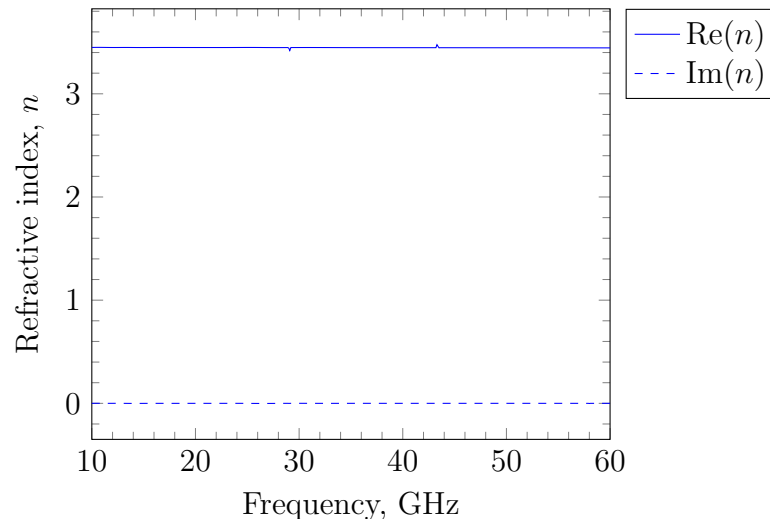


Figure 4.21: The value of  $n$  for a 3 mm block of silicon with a 1.426 mm coat of polypropylene calculated from the embedded parameter extraction equations, equation (4.23).

### 4.3.3 NRI Slab Design

With the working modified parameter extraction code, a HFSS model consisting of the twenty-one unit cell was created with a  $\lambda_{\text{PP}}/4$  coating of polypropylene on the outer surfaces. The frequency chosen was 82 GHz, where  $n = -1$  is achieved, resulting in a thickness of 608  $\mu\text{m}$  for  $d_{\text{PP}}$  using the nomenclature defined in

#### 4: ARTIFICIAL DIELECTRICS WITH METAMATERIALS

figure 4.20. To create a twenty-one cell slab would have required forty-two copper fishnet grids. This was an impractical amount of grids to manufacture so a plan was made to make a thinner fishnet structure using fewer grid. From this, smaller grids could be cut, and then stacked on top of one another to create the final twenty-one cell structure. From a sample made on a 21 cm ring, seven 6 cm diameter circles could be cut. This is shown in figure 4.22. A three unit cell structure made up of six 21 cm diameter grids would be created. From this seven 6 cm diameter circles would be cut and these would be layered on top of one another to form a final twenty-one cell structure. 6 cm was deemed a suitable size that would allow the least amount of grids to be used to create a final structure large enough to be experimented with. It also ensured that there was a suitably large enough space between the circles to allow them to be cut, either mechanically or with a high powered laser.

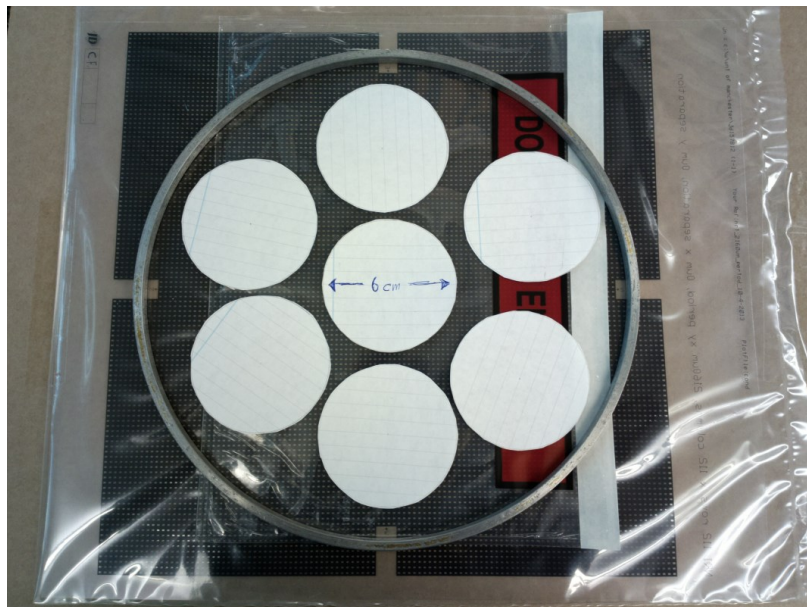


Figure 4.22: 21 cm aluminium ring on top of the photo mask (sealed in plastic to prevent damage) for the fishnet grids. Seven 6 cm paper circles are arranged within the ring to demonstrate how seven smaller circles could be cut from a larger 21 cm sample.

#### 4.3.4 Manufacture

A recipe was made for the three cell structure and is shown in figure 4.23. The recipe called for the copper fishnet grids to be on 38  $\mu\text{m}$  polypropylene substrates with additional 38  $\mu\text{m}$  polypropylene spacer to provide the 114  $\mu\text{m}$  separation between the grids. The recipe was divided into six layers, denoted by the dashed red lines in figure 4.23. Each grid was photolithographed as described in section 3.2.1 and each one was hot pressed with the requisite number and arrangement of polypropylene spacers required to create each layer. An issue that arose after the layers were hot pressed was that layers A and F would curl up as shown in figure 4.24, with the polypropylene side inward. This occurred because these layers had bare copper on one side of a thin 76  $\mu\text{m}$  substrate. The curling effect was not as pronounced with the layers B through E as they had polypropylene on both sides of the copper grids.

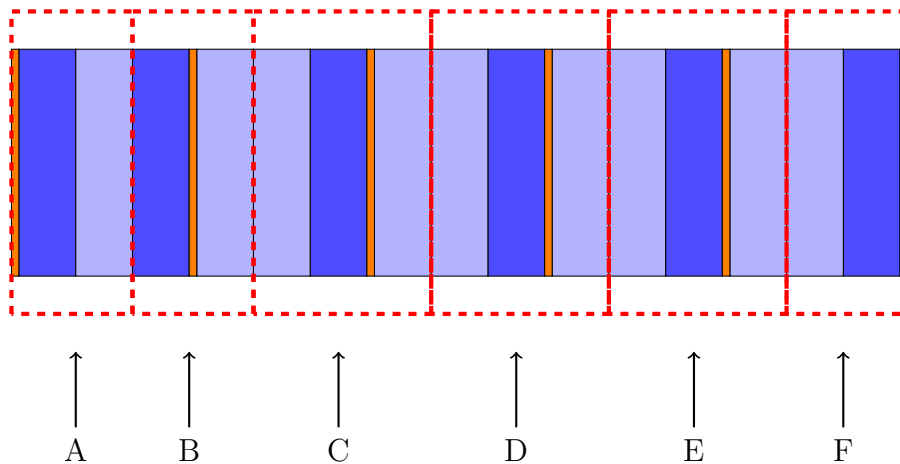


Figure 4.23: Recipe for the three unit cell structure consisting of six fishnet grids. The copper is represent by orange, the polypropylene substrate associated with the copper is dark blue and the polypropylene spacers are light blue. Both the substrates and the spacers are 38  $\mu\text{m}$  thick. The dashed red outline denote how the individual polypropylene sheets were divided into layers A to F before alignment.

Transmission readings of each layer were then taken using a vector network analyser (VNA) along the grids  $x$ - and  $y$ -axes using a set up that will be described in section 4.3.5. The results were compared to HFSS simulations of the layers to

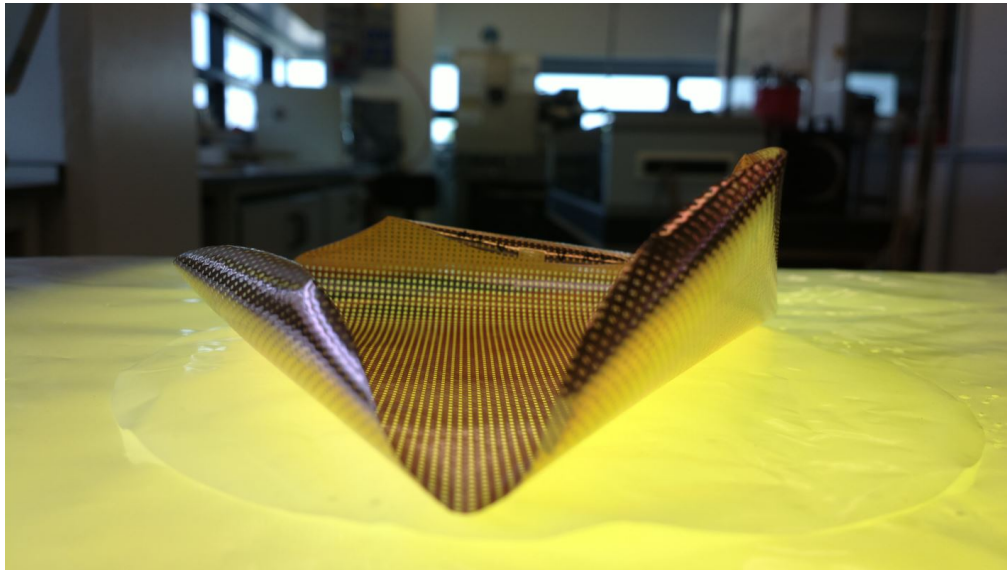


Figure 4.24: Layer A copper side down on top of a light box before initial alignment. The curling effect is evident.

assess the performance of the layers and detect any possible defects before they were aligned and hot pressed to form the final structure. All layers performed admirably showing good match in both transmitted intensity,  $|S_{21}|^2$ , and transmitted phase,  $\arg(S_{21})$ . Layer C is show as an example in figure 4.25 and figure 4.26.

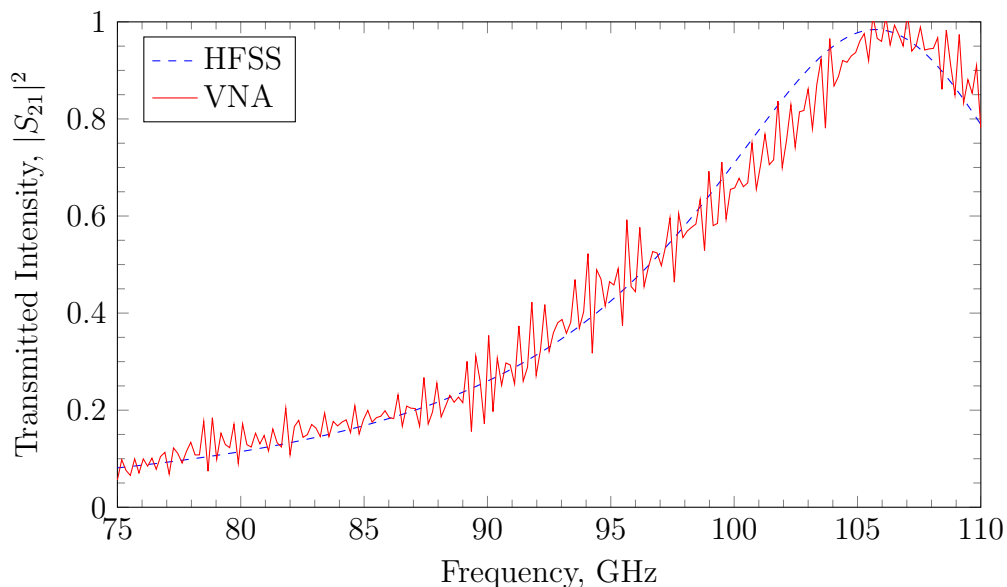


Figure 4.25: Transmitted intensity,  $|S_{21}|^2$  of Layer C as simulated by HFSS (dashed) and experimentally measured by the VNA (solid).

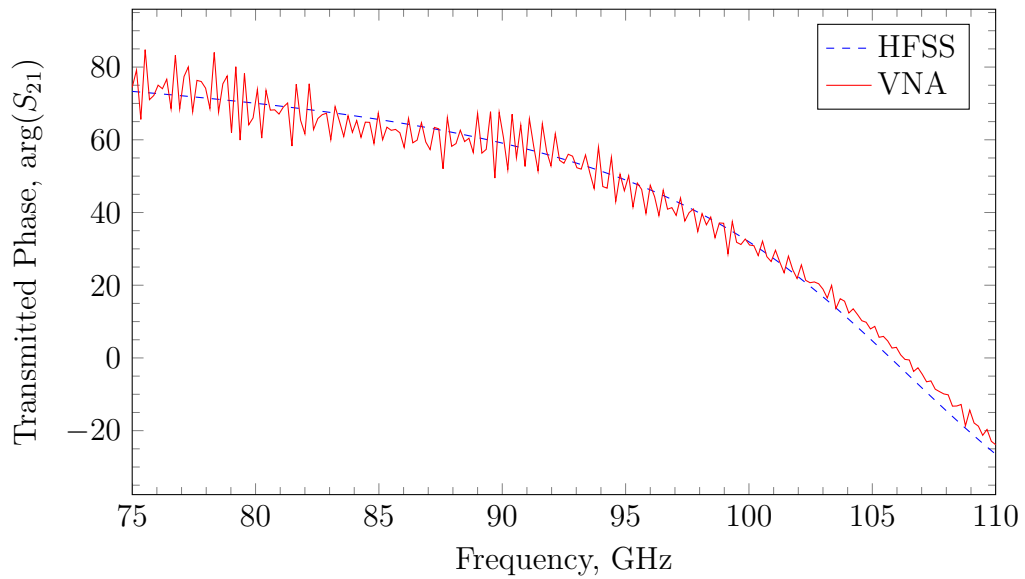


Figure 4.26: Transmitted phase,  $\arg(S_{21})$ , of Layer C as simulated by HFSS (dashed) and experimentally measured by the VNA (solid).

Layers A to F were aligned and spot welded together as described in section 3.3.1. The alignment was difficult despite the existence of alignment marks at the grids' compass points. In this case only two of the alignment marks between each layer could actually be aligned. The standard procedure would then be to assess the alignment in other locations on the grid. However, because the fishnet design is mostly copper, most of the light from the light box is blocked, so the only other detail visible through the loupe were the rectangular holes in the fishnet. After spot welding, transmission readings were taken along the  $x$ - and  $y$ -axes prior to the hot pressing to ensure the structure performed as required. As will be described later in section 4.3.6 the transmission readings for the spot welded layers were not good and steps were taken to identify the cause. In the end, layers D, E and F and layers A, B and C were separately hot pressed to form what will be referred to as layers DEF and ABC. These two layers were then hot pressed together to form the final three cell structure after further transmission readings of layers DEF and ABC. The hot pressing step was carried as described in section 3.3.2 but with a temperature of 200 °C for 22 h.

### 4.3.5 Measurements

Transmission readings were taken with with a Rohde & Schwarz<sup>3</sup> ZVA40 Vector Network Analyser (VNA) attached to ZVA-Z110 frequency converter with WR-10 heads and corrugated W-band horns. The set up, shown in figure 4.27 and figure 4.28, allows the MUT, placed between the horns, to be illuminated by a portion of the Gaussian beam. The corrugated horns are placed so that they are off-axis to one another in such a way that the line connecting the centre of the two horns perpendicularly bisect the MUT. This is done so that standing waves between the horns and the MUT are reduced as the reflections from the MUT will not travel back to the horn. The requirement that the line connecting the horns' centres bisect the MUT perpendicularly is to ensure that the MUT is tested with radiation at normal incidence, as this is what was simulated in HFSS.

To take the transmission data, a reading is first taken when no MUT is present within the set up and this VNA data is normalised so that 0 dB corresponds to perfect transmission. Subsequent transmission readings of MUTs taken are then relative to this.

Reflection readings were taken with the VNA as before but with a different arrangement (figure 4.29 and figure 4.30). The frequency converters, WR-10 heads and horns are placed on the same side of the MUT. The horns are placed side by side pointing directly at the MUT. Eccosorb with a small hole cut into it is placed in front of the MUT so that only reflections from a small area of the MUT would be measured. In this setup the VNA is set to take  $S_{21}$  readings as before but because of the arrangement with the radiation from the horns being emitted and received in the same locale it is effectively measuring the reflection coefficient. To take the reflection data, the readings are normalised to a metal plate that is used as a perfect reflector so that 0 dB corresponds to perfect reflection. Subsequent reflection readings of MUTs are now relative to this.

---

<sup>3</sup><http://www.rohde-schwarz.co.uk>

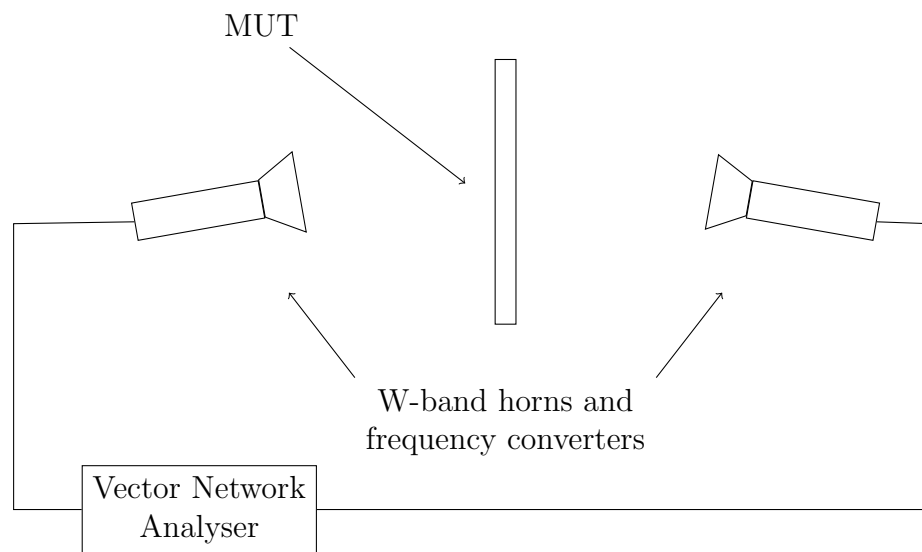


Figure 4.27: Diagram of the experimental setup used for the transmission readings of the individual layers and the combined layers.

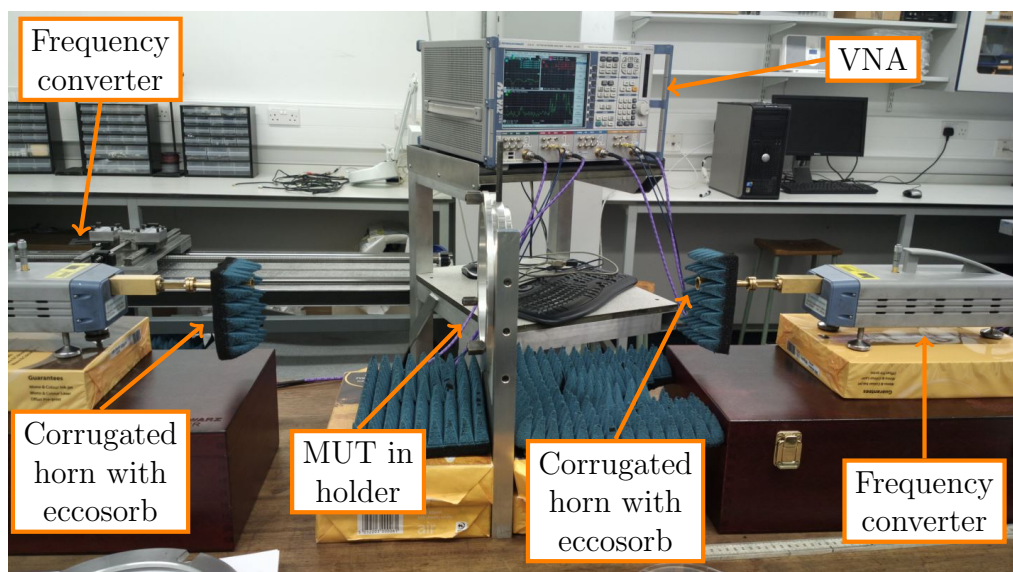


Figure 4.28: Annotated photo of an experimental set up for transmission readings of individual layers and the combined layers.

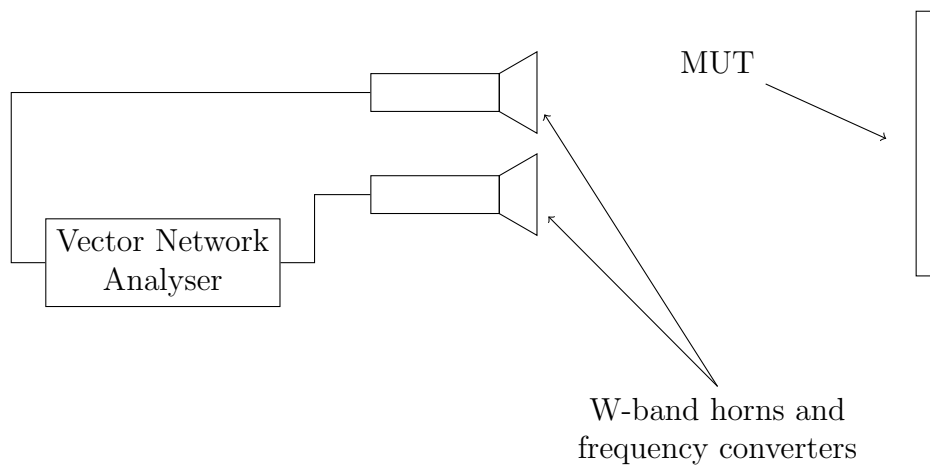


Figure 4.29: Diagram of the experimental setup used for the reflection readings of the hot pressed layers.

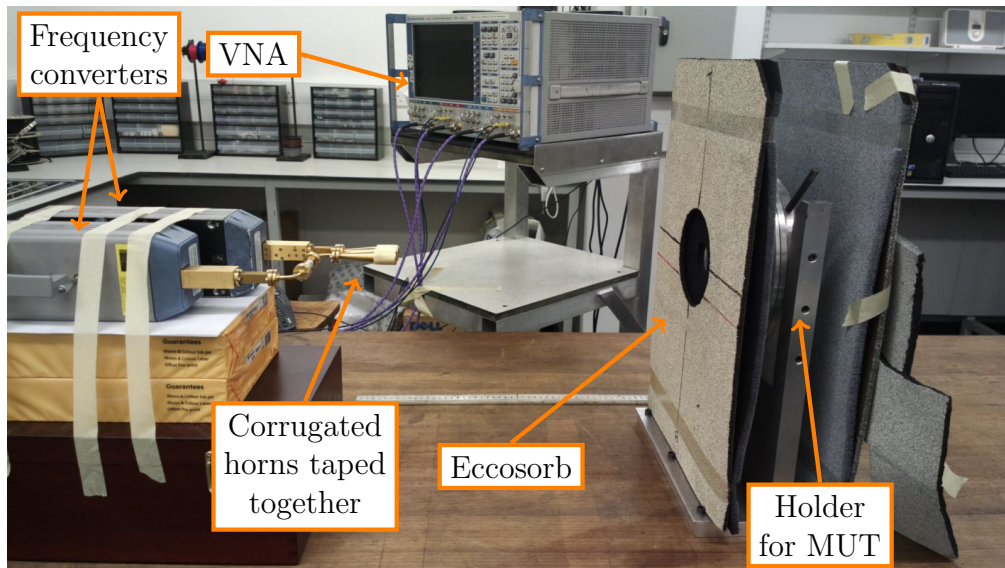


Figure 4.30: Annotated photo of an experimental set up for reflection readings of individual layers and the combined layers.

### 4.3.6 Results

As mentioned in section 4.3.4 transmission readings were taken of the spot welded layers prior to their hot pressing. This initial reading was done to test the performance of the stacked layers and identify any possible problems e.g. with their alignment. This test is important because the bonding of the layers via hot pressing

is irreversible and problems not caught before that stage of the manufacture would result in the waste of many grids and the man-hours of work spent manufacturing them. However, it must be stressed that the spot welded grids are *not* expected to work at their anticipated performance as predicted by modelling and simulation. This is due to the air gaps that exist between the layers of the spot welded structure. Despite this performance approaching that of the final hot pressed structure can be observed at this early stage though (G. Pisano, personal communication, 2012).

The results for the  $x$ -polarised transmitted intensity and phase of the spot welded layers ABCDEF are shown in figures 4.31 to 4.32. As can be seen, the results between the experimental readings do not match at all with the HFSS simulation. The transmitted intensity measured by the VNA readings is very low and the  $y$ -axis on the graph in figure 4.31 is expressed in decibels (dB) so it would be visible. Similar discrepancy is seen in the  $y$ -polarised readings. The spot welded layers seemed to be acting as a mirror, reflecting all incident radiation. The main culprit for the difference was thought to be the air gaps introduced primarily by the outermost layers, A and F, whose tendency to curl up gave the outer surfaces a rather wrinkled appearance (figure 4.33).

To solve this problem, it was decided that two taut polypropylene sheets mounted on aluminium rings could be used to sandwich the layers together, thereby attempting to remove the air gaps and produce better contact between the individual layers. Two 47  $\mu\text{m}$  polypropylene sheets were mounted and prepared (as described in section 3.2.1.1) onto 12 cm diameter rings. Transmission readings were taken once again with the spot welded layers sandwiched between the two. The transmitted intensity readings are shown in figure 4.34 and apart from the region between 98.5 GHz to 110 GHz, there was still very little match between experiment and the HFSS simulations that also took into account the two 47  $\mu\text{m}$  polypropylene sheets.

Following on from this result, the structure was taken apart layer by layer,

#### 4: ARTIFICIAL DIELECTRICS WITH METAMATERIALS

beginning with layer A, with transmission readings taking place after each new layer had been removed. These readings were also done using the polypropylene sheets to sandwich the layers. These readings were carried out in this way to eliminate the possibility that there was one or more grids that were causing the

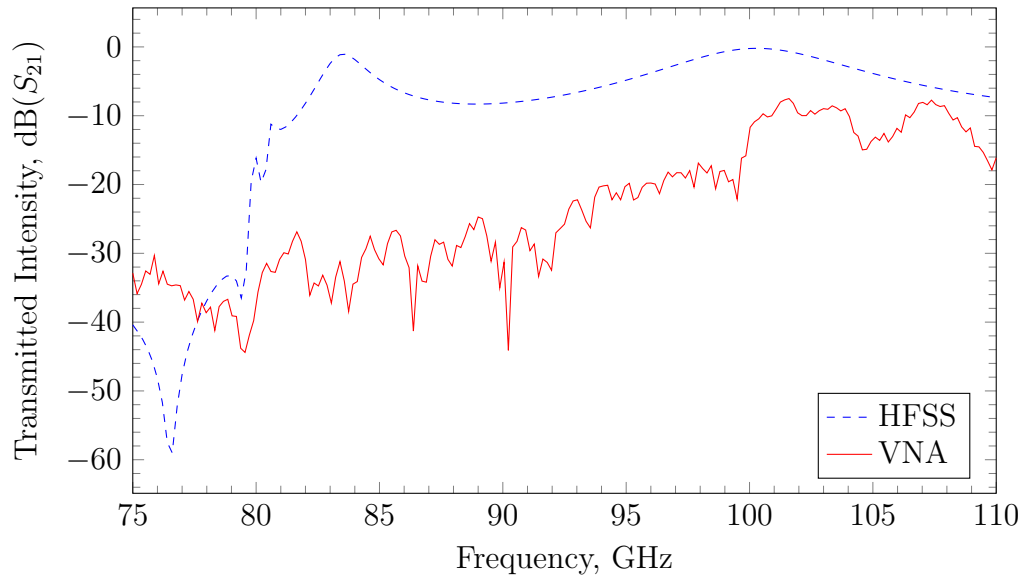


Figure 4.31: Transmitted intensity,  $\text{dB}(S_{21})$ , readings taken along the  $x$ -axis for the spot welded layers ABCDEF.

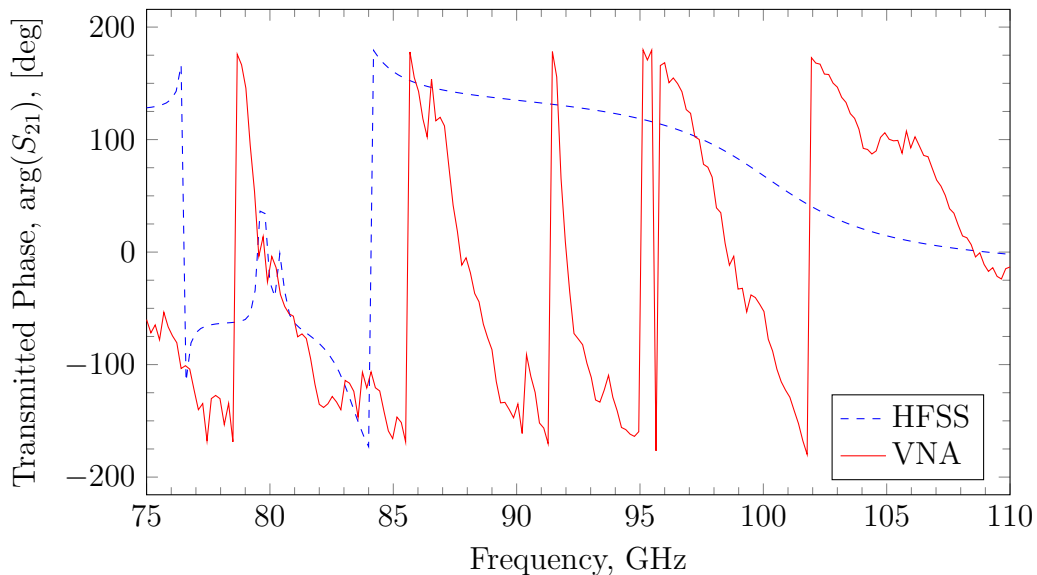


Figure 4.32: Transmitted phase,  $\text{arg}(S_{21})$ , readings taken along the  $x$ -axis for the spot welded layers ABCDEF.



Figure 4.33: Layer A side of the spot welded layers ABCDEF.

discrepancy. Basically, if the measured data began to match the simulation data after a particular layer was removed, then we would know that it was that layer (and possible other layers removed prior) that were causing problems. As it turned out, the match between the measured and simulated transmitted intensity readings did not improve much even when only two spot welded layers, EF, remained. The transmitted phase however showed trend toward overlapping the simulation data. As an example the  $|S_{21}|^2$  and  $\arg(S_{21})$  readings of the spot welded layers DEF are shown in figure 4.36 and figure 4.37 respectively.

Finally, it was decided that layers D, E and F should be realigned and hot pressed to test its performance under a more ideal manufactured state. Transmission readings were taken without the  $47\ \mu\text{m}$  polypropylene sheets as there was no need for them. The results are shown in figure 4.38 and figure 4.39 and it can be seen that experimental data and simulated data showed very good concurrence now that the layers were properly bonded.

Subsequently, layers A, B and C were aligned and hot pressed as well. Then the combined layers ABC and DEF were aligned and hot pressed to form the final three unit cell structure. Once again, transmission readings were taken and

the results for the  $x$ -axis readings are shown in figure 4.40 and figure 4.41. The readings of  $|S_{21}|^2$  that exceed 1 in figure 4.40 are possibly due to calibration errors.

The transmitted intensity has good correspondence between the measured and

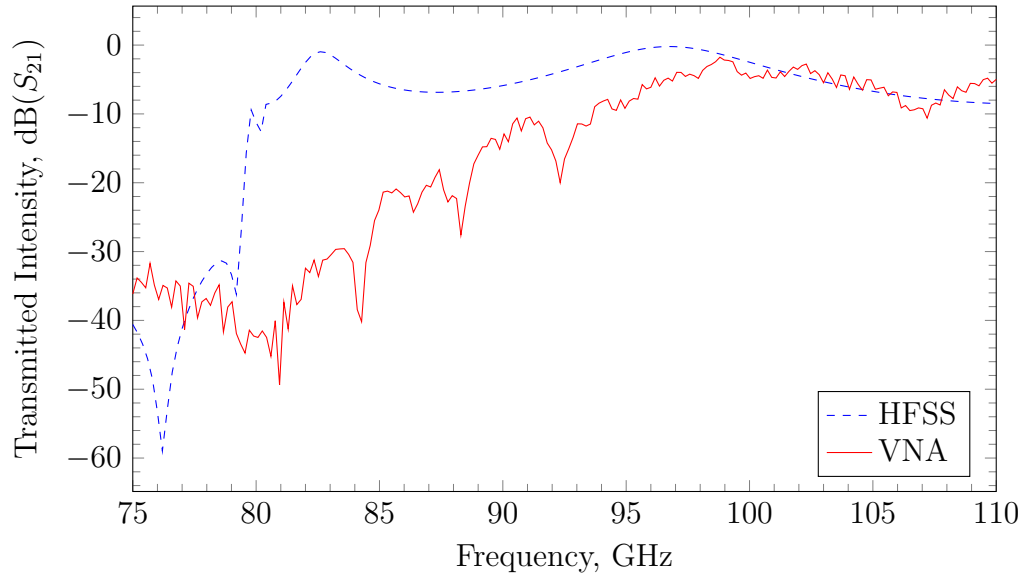


Figure 4.34: Trasmitted intensity,  $\text{dB}(S_{21})$ , readings taken along the  $x$ -axis for the spot welded layers ABCDEF sandwiched between two  $47 \mu\text{m}$  polypropylene sheets.

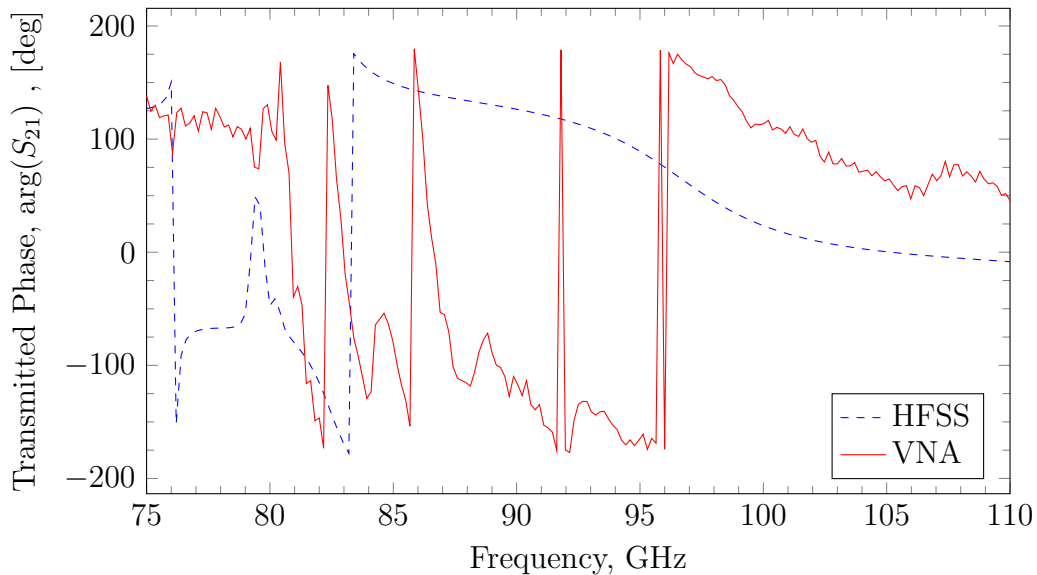


Figure 4.35: Trasmitted phase,  $\text{arg}(S_{21})$ , readings taken along the  $x$ -axis for the spot welded layers ABCDEF sandwiched between two  $47 \mu\text{m}$  polypropylene sheets.

modelled data with only a small blue shifting of the peak that was simulated to occur at 102 GHz. The overlap between the model and simulation in the the phase

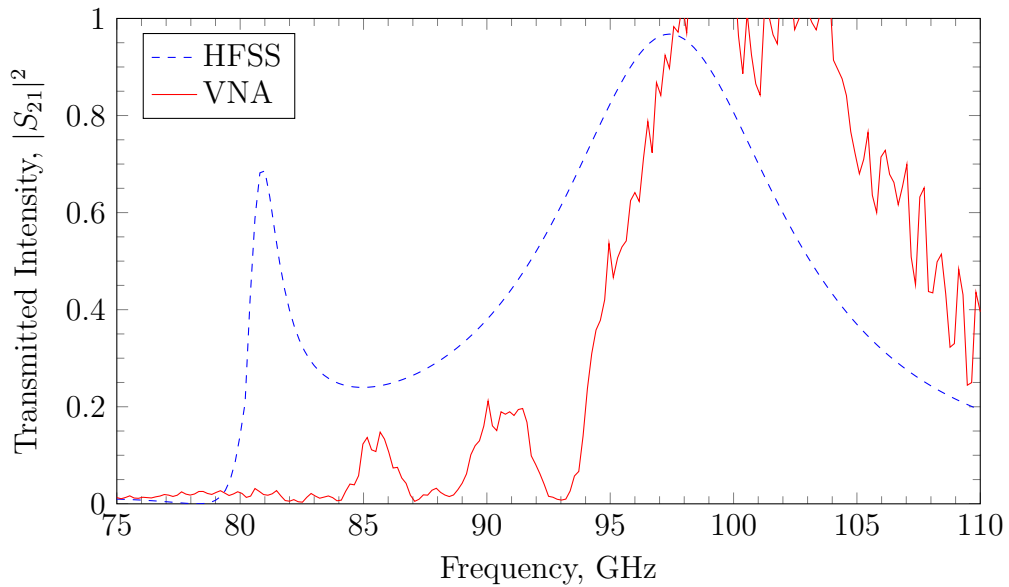


Figure 4.36: Transmitted intensity,  $|S_{21}|^2$ , readings taken along the  $x$ -axis of the spot welded layers DEF sandwiched between two  $47\ \mu\text{m}$  polypropylene sheets to squash the layers together and ensure more thorough contact between the layers.

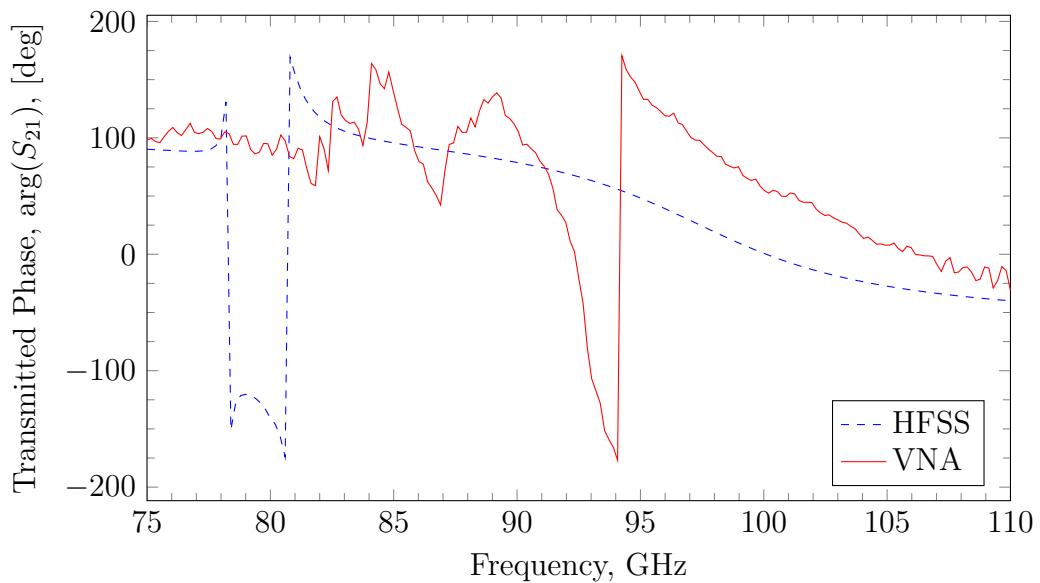


Figure 4.37: Transmitted phase,  $\arg(S_{21})$ , readings taken along the  $x$ -axis of the spot welded layers DEF sandwiched between two  $47\ \mu\text{m}$  polypropylene sheets.

#### 4: ARTIFICIAL DIELECTRICS WITH METAMATERIALS

readings is very good between 82 GHz to 110 GHz. Below this the experimental transmitted phase wraps around  $360^\circ$  three times and shows a less good match with the HFSS model. However in the region 75 GHz to 82 GHz the transmitted

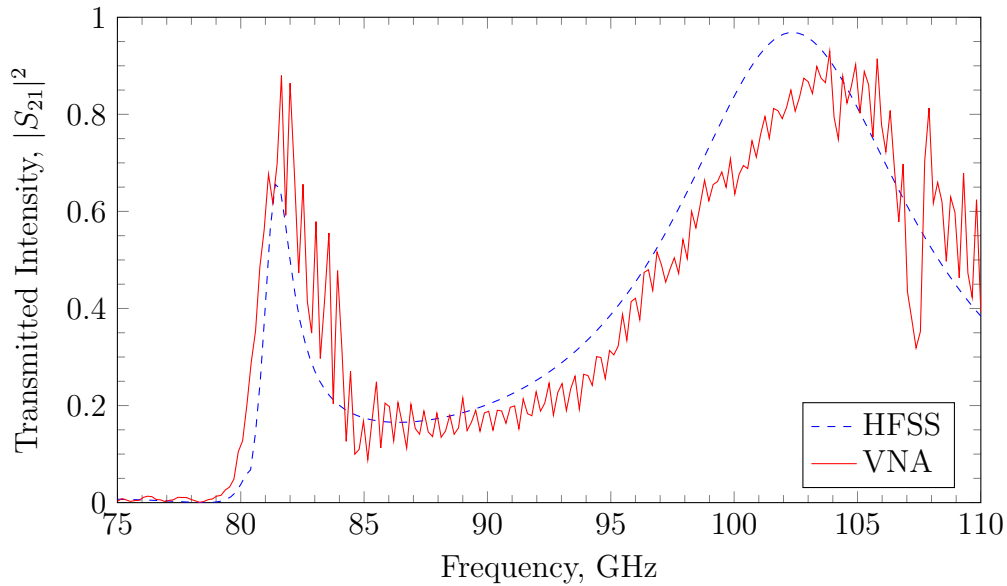


Figure 4.38: Transmitted intensity,  $|S_{21}|^2$ , readings taken along the  $x$ -axis of the hot pressed layers DEF.

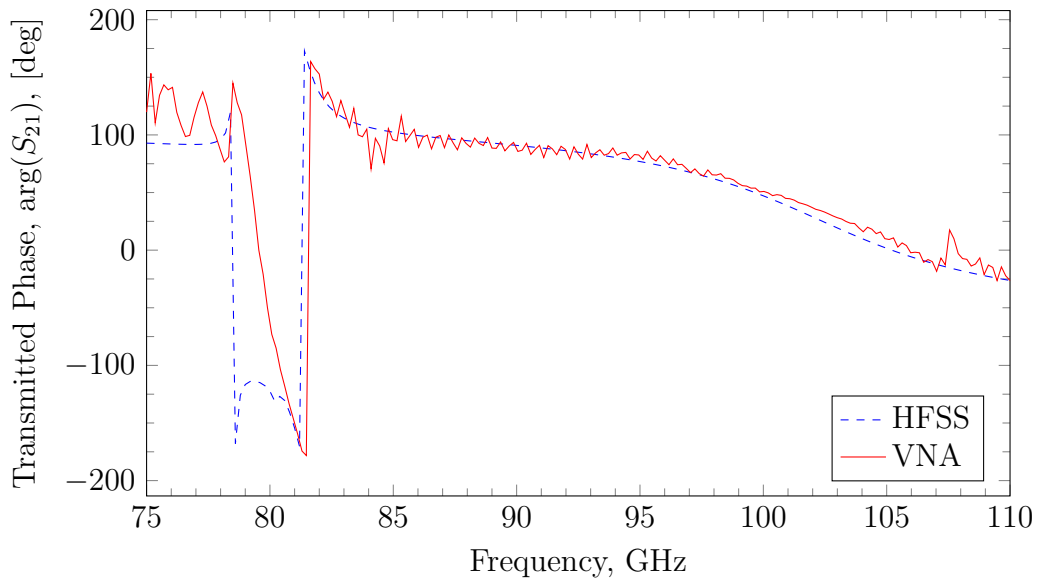


Figure 4.39: Transmitted phase,  $\arg(S_{21})$ , readings taken along the  $x$ -axis of the hot pressed layers DEF.

intensity goes to zero, meaning that phase becomes undefined and difficult to measure so noisy readings here are expected.

The reflection measurements for the  $x$  polarisation are shown in figure 4.42 and

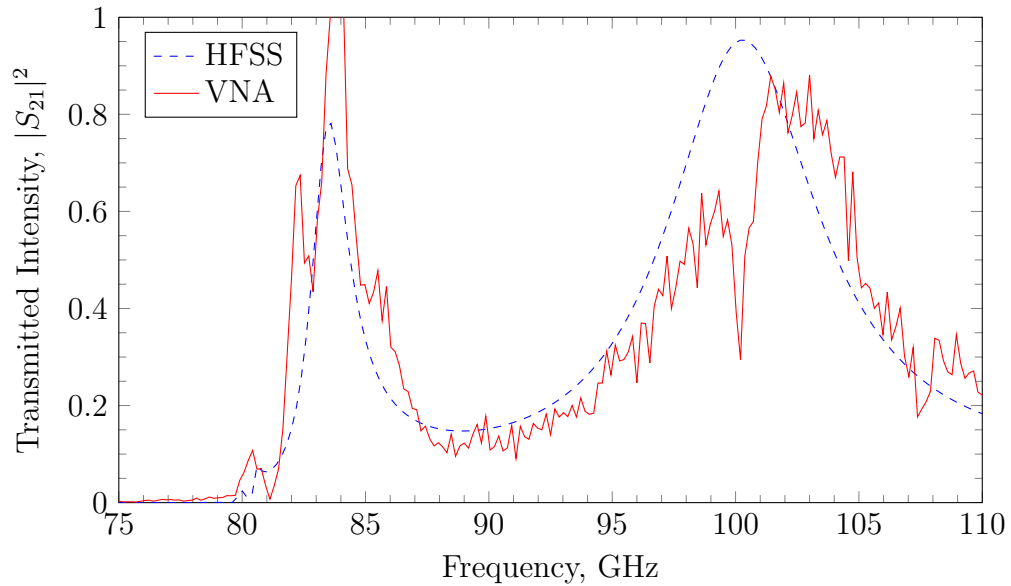


Figure 4.40: Transmitted intensity,  $|S_{21}|^2$ , readings taken along the  $x$ -axis of the hot pressed layers ABCDEF.

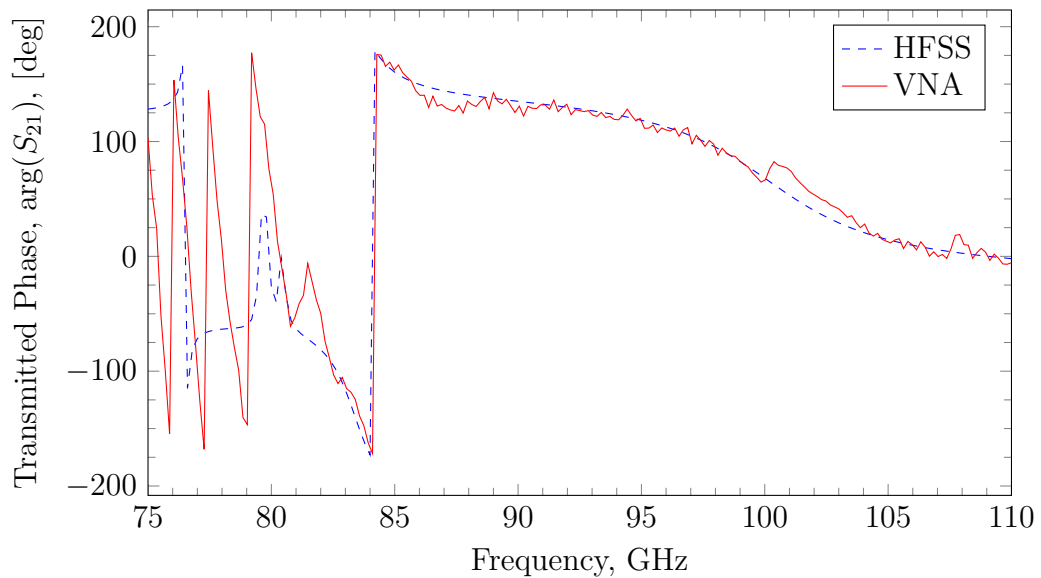


Figure 4.41: Transmitted phase,  $\arg(S_{21})$ , readings taken along the  $x$ -axis of the hot pressed layers ABCDEF.

figure 4.43. In the reflected intensity measurements, the measured and simulated data match very well with each other, barring the deviations that occur from standing waves and possible surface imperfections on the grids. The reflected phase, shown in figure 4.43 had its reference plane corrected due to the different thicknesses of the reflector and the MUT. A close match is seen between the measured and simulated data here too.

With the transmission and reflection data in hand, the calculation of the refractive index was then carried out using the robust parameter extraction method described in section 4.2.2. Equation (4.23) of the modified method described in section 4.3.2 was not required because layers ABCDEF were not sandwiched between two layers of polypropylene. The reference planes of the both of these data needed to be moved so as to correspond to the physical thickness of the layers ABCDEF. A problem that arose with the calculation was the noise in the values of  $\arg(S_{21})$  below  $\sim 82$  GHz. The jumps of  $360^\circ$  caused the iterative step of the parameter extraction method to force the calculated value of the refractive index to  $> 30$ . A solution to combat this was made by using the frequency point 81.2 GHz of the VNA data as the starting point for the refractive index calculation. This point was chosen because below it the values of  $\arg(S_{21})$  from the VNA no longer align with the simulation and due to the small value of the magnitude of  $S_{21}$  at these points, are most likely unreliable. The results are shown in figure 4.44 and figure 4.45. An alternative approach that wasn't carried out due to time constraints was the rewriting of the iterative step of the parameter extraction code so that it began from the high end of the frequency scale and iterated downward.

The measured real part of the refractive index (figure 4.44) follows a similar path to that calculated from the HFSS simulation although it appears to be blue shifted by  $\sim 4$  GHz. NRI band is seen to exist between 82.2 GHz to 101.6 GHz, a fractional bandwidth of 21 %. This band could be wider, but given the noisy  $\arg(S_{21})$  data caused by low value of  $|S_{21}|^2$  this is hard to determine.  $n = -1$  is achieved around 90 GHz compared to the HFSS simulation which predicted a

### 4.3: NEGATIVE REFRACTIVE INDEX SLAB

value of 86.5 GHz. A good match is also seen between the measured and simulated values of the imaginary component of the refractive index.

At this point, work on creating the twenty-one unit cell slab was halted due to time constraints.

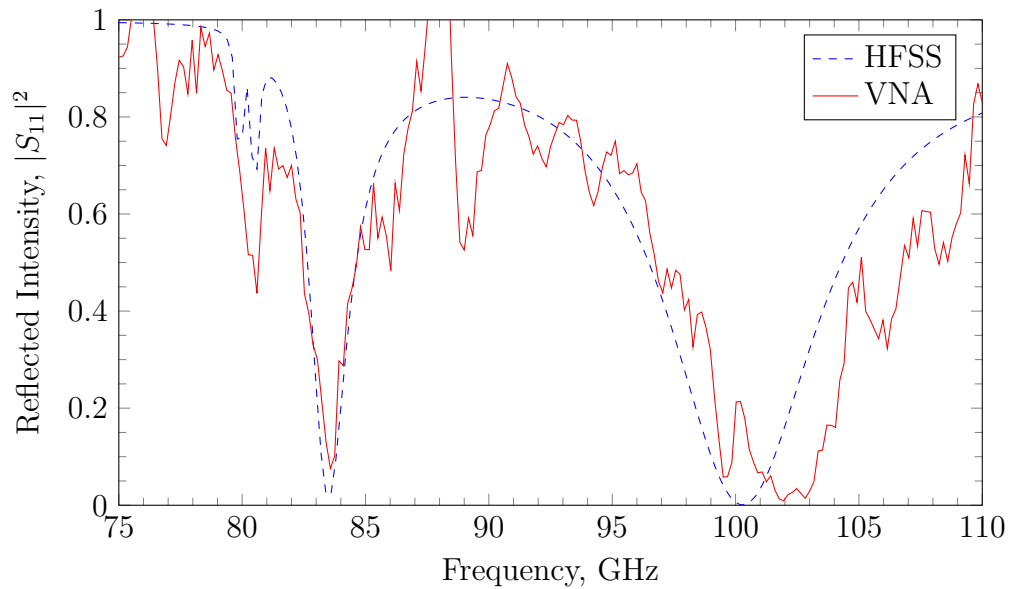


Figure 4.42: Reflected intensity,  $|S_{11}|^2$ , readings taken along the  $x$ -axis of the hot pressed layers ABCDEF.

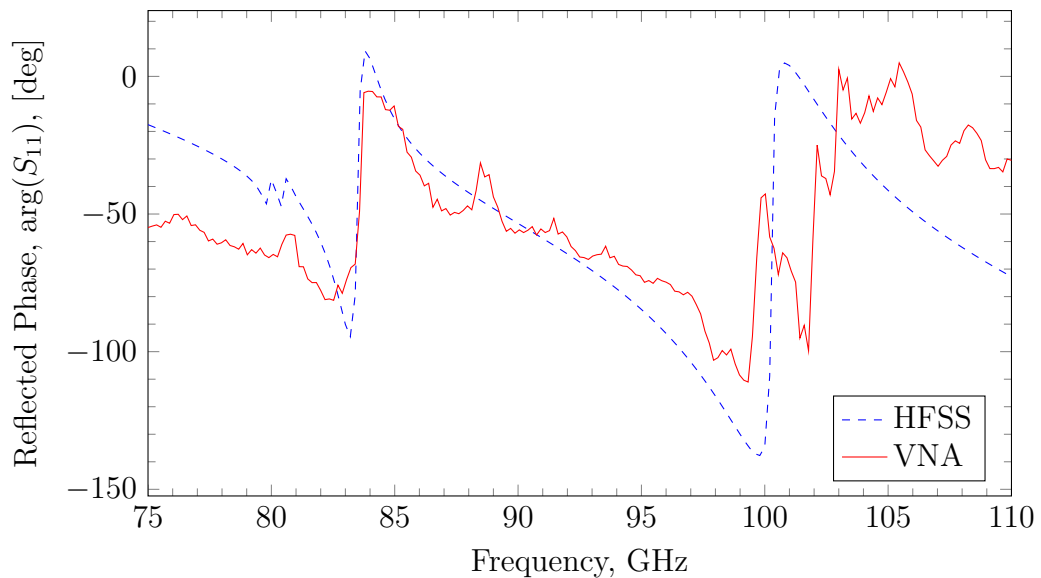


Figure 4.43: Reflected phase,  $\arg(S_{11})$ , readings taken along the  $x$ -axis of the hot pressed layers ABCDEF.

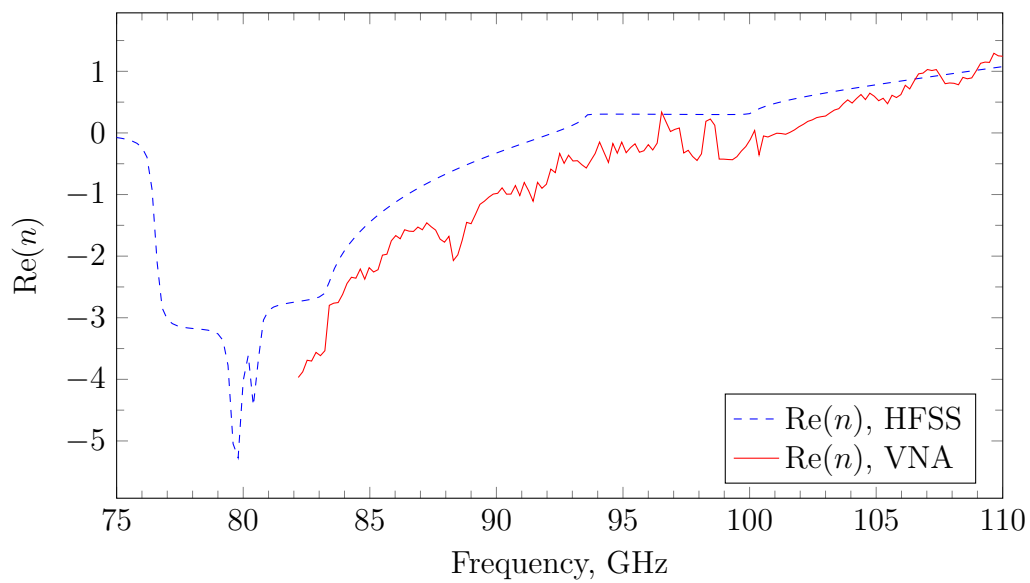


Figure 4.44: The real part of the refractive index,  $\text{Re}(n)$ , of the negative index block.

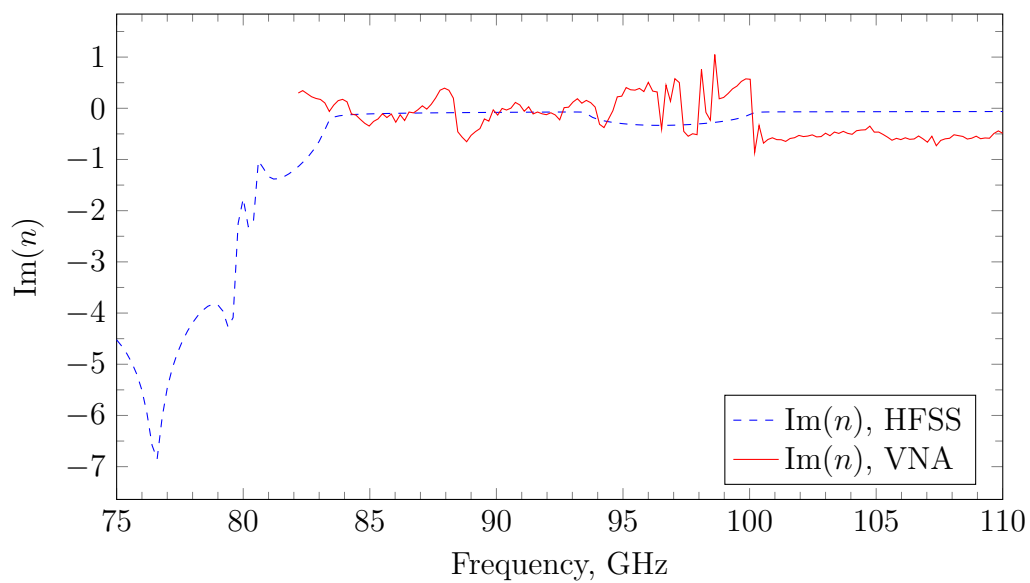


Figure 4.45: The imaginary part of the refractive index,  $\text{Im}(n)$ , of the negative index block.

## 4.4 Conclusions

In this chapter, a working three unit cell thick, negative refractive index metamaterial block that functioned in the W-band was designed, manufactured and tested. The geometry used was based on a fishnet design presented in Mary et al. (2008). The manufactured device was able to produce a value of  $n = -1$  at about 90 GHz compared to simulated values of 86.5 GHz.

Due to time constraints, the full twenty-one cell slab was not created from this initial three unit cell thick block. However, we see from the presented measurements that with just three unit cells, a negative refractive band could be created with this fishnet design. It is expected that should a thicker structure be created, the NRI band will remain allowing for further studies, such as observing superlensing.



# Chapter 5

## Highly Birefringent Artificial Dielectrics

*Were you expecting an exploding pen? We don't really go in for that any more.*

Q, 2012 October

### 5.1 Introduction

Early on in the development of negative refractive index (NRI) metamaterial, much work was put into envisaging uses for and creating metamaterials that were isotropic in their behaviour. For certain applications such as invisibility cloaks, polarisation independence is paramount. However, in certain cases having different electromagnetic responses to radiation depending on their polarisation is advantageous. Such materials are called birefringent.

In this chapter we begin by introducing the concept of birefringence. Then a brief description of previous attempts at creating highly birefringent but narrow-band wave plates is given. A method to increase the usable bandwidth is discussed, along with a description of its implementation. Finally, the design, optimisation and manufacturing process, as well as a comparison between measured and mod-

elled data for an air gap half wave plate and a polypropylene embedded quarter wave plate are given.

## 5.2 Birefringence

Not all materials have an isotropic electromagnetic behaviour that can be described by a single value of  $\varepsilon_r$  and  $\mu_r$ . Generally these two quantities are represented as a  $3 \times 3$  tensor with the diagonal elements describing the electromagnetic behaviour along the  $\hat{x}$ -,  $\hat{y}$ - and  $\hat{z}$ -axes (assuming a Cartesian coordinate system). Materials with unequal diagonal components of  $\varepsilon_r$  and  $\mu_r$  are called birefringent. Such behaviour arises in materials with an anisotropic crystalline structure.

Radiation propagating through a birefringent material will find its polarisation state altered as it travels. The reason can be easily seen when the radiation's  $\mathbf{E}$ -field is decomposed into its two orthogonally polarised components,  $E_x$  and  $E_y$ . Upon entering the birefringent material, each polarisation experiences a different refractive index, subject to the values that the diagonal components of  $\varepsilon_r$  and  $\mu_r$  take. This causes each polarisation component to travel at different speeds.

A uniaxially birefringent material is one where two of the diagonal elements of the tensor are equal, whilst the third is different. In such a material a single "optic axis" may be defined. A birefringent material's optic axis defines a direction in which light rays experience no birefringent effects. Cutting the material so that the optic axis is parallel to the surfaces i.e. light rays travel perpendicular to the optic axis, results in the creation of a wave plate (wave retarder). These are devices used to change the polarisation state of radiation.

The differential phase shift,  $\Delta\phi$ , between the radiation's orthogonal components produced by the wave plate is given by

$$\Delta\phi = \frac{2\pi df}{c_0} \cdot \Delta n \quad (5.1)$$

where  $d$  is the thickness of the wave plate,  $f$  is the frequency of the radiation,  $c_0$  is the free space speed of light and  $\Delta n$  is the difference between the refractive indices along the wave plates orthogonal axes i.e. the birefringence.

In the mm wavelength / THz frequency range there's a shortage of available birefringent materials that can be used to construct wave plates. With the ability to design for certain electromagnetic properties, metamaterials are an ideal substitute. Depending on how the metamaterial wave plate is constructed, the end result can be thinner, less massive, built to larger dimensions and ideally have a better electromagnetic response than is possible with natural birefringent materials. The advantages of some of these possibilities were described in section 1.5.2.

## 5.3 Highly Birefringent Metamaterials

### 5.3.1 Narrowband Implementations

Most of the proposed applications of metamaterials, after the demonstration of NRI in Shelby et al. (2001a), focussed on applications that required an isotropic response to electromagnetic radiation. Two papers, Imhof and Zengerle (2007) and Weis et al. (2009), were the first to design NRI metamaterials that intentionally had birefringent behaviour, which could be used to build wave plates. The former paper used pairs of crosses (figure 1.10d) with arms of different lengths to create a Quarter Wave Plate (QWP) that had a NRI in both arms. The latter paper used a metamaterial geometry that could achieve both NRI and PRI allowing the design of compact QWPs and Half Wave Plates (HWPs). Weis et al.'s geometry was based on the cut wire pair design (figure 1.10a), itself related to the single-layered capacitive grids described in e.g. Ulrich (1967).

As noted by the authors in the aforementioned papers, the usable bandwidth of the resulting wave plate is very narrow. Here we use a strict definition for the usable bandwidth: It is the region where the phase difference varies by only  $\pm 2\%$  of the required value. For a QWP it is the region where  $\Delta\phi = (90 \pm 2)^\circ$  and for

a HWP it is where  $\Delta\phi = (180 \pm 3)^\circ$ . Using this definition, Imhof and Zengerle (2007)'s QWP achieved a fractional bandwidth of 0.9 % and Weis et al. (2009)'s QWP and HWP achieved 0.5 %. These narrow bandwidths are a consequence of the large change in the NRI value in the vicinity of the metamaterial's resonant frequency.

### 5.3.2 Increasing the Bandwidth with the Pancharatnam Method

A technique referred to as the Pancharatnam method was used to increase the usable bandwidth. The method was described in two papers, Pancharatnam (1955a,b), the former for a circular polariser and the latter for a QWP. The QWP was constructed by the stacking of consecutive wave plates, each with their optic axes rotated through an angle. The method has been used successfully with wave plates constructed out of birefringent materials (Title 1975; Hanany et al. 2005), as well as their waveguide (Pisano et al. 2011, 2012a) and microstrip (Ladu and Pisano 2013) equivalents.

In the single wave plate case, assuming a thickness  $d$  and birefringence  $\Delta n$ , the required value  $\Delta\phi$  can only be achieved at a single frequency,  $f$ . At frequencies below and above  $f$ , the phase difference will be less than or greater than the required  $\Delta\phi$ , given the linear relationship between  $\Delta\phi$  and  $f$  as seen in equation (5.1). By using  $N$  wave plates, each rotated by specific angles,  $\Delta\phi$  can be reached at  $N$  different frequencies. Cascading these wave plates will then produce a broader frequency range where  $\Delta\phi$  is reached.

The formalism used in Pancharatnam's papers was derived via geometric calculations based on the Poincarè sphere. Briefly, the Poincarè sphere is a way to picture changes in polarisation by mapping polarisation states to points on a sphere as shown in figure 5.1. Linear polarisation states are represented along the equator. Left and right circular polarisation is represented at the north and

south poles respectively. The various elliptical polarisation states exist at the intermediate latitudes.

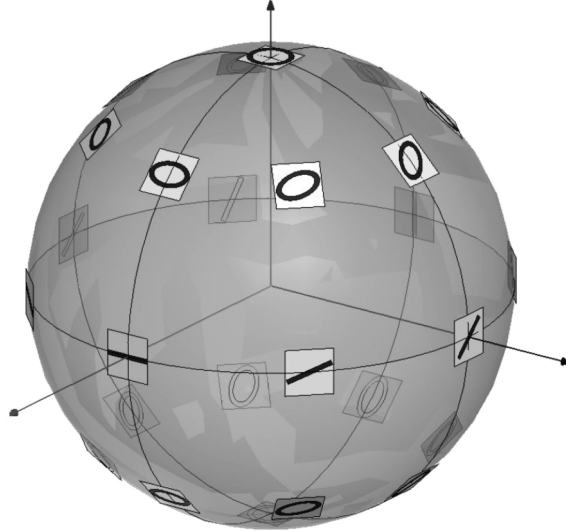


Figure 5.1: The arrangement of the polarisation states on the surface of the Poincarè sphere. Image taken from Savini et al. (2006, Figure 1).

When linearly polarised radiation of frequency,  $f$ , passes through a wave plate, it experiences a differential phase shift of  $\theta$ . Correspondingly the radiation's location on the Poincarè sphere is translated by an angle  $\theta$ . The inclination of the rotation is related to the angle between the radiation's polarisation angle and the wave plate's optic axis. Frequencies below and above  $f$  are also rotated but through differing amounts, based on the frequency dependence of the birefringence. The result is that a single point representing the initial polarisation state becomes a spread of points with each point representing the new polarisation state for each frequency. By combining a number of wave plates rotated through different angles, the spread can be brought back to a single point. By deriving an expression that described the path of a polarisation state around the Poincarè sphere caused by three plates, Pancharatnam was able to solve a simultaneous set of equations to retrieve the required rotation angles of each plate. This ensured that the final polarisation state was equal at three different frequencies of his choosing.

The method was extended in Adachi and Kennaugh (1960) to include the effect of reflections from the interfaces between the wave plates. This was achieved by using a transfer matrix approach akin to the Transmission Line (TL) approach detailed in section 2.3. It is this formalism that the author's work is based upon.

### 5.3.3 TL Modelling of the Pancharatnam Method

The propagation of the two polarisations can be treated independently. To handle them simultaneously with the Transmission Line (TL) method required an extension to the existing matrices shown in section 2.3. The  $2 \times 1$  column matrices containing the field quantities for the  $x$  and  $y$  polarised fields are vertically concatenated into  $4 \times 1$  column matrices. The appropriate alterations to the  $2 \times 2$  propagation and matching matrices into  $4 \times 4$  matrices are now shown. Representing the original propagation matrix equation (2.4) for  $x$  and  $y$  polarisations with  $P_{x,y}$ , it now takes the form

$$\begin{bmatrix} E_x \\ H_y \\ E_y \\ -H_x \end{bmatrix}_i = \begin{bmatrix} P_x & 0 \\ 0 & P_y \end{bmatrix} \begin{bmatrix} E_x \\ H_y \\ E_y \\ -H_x \end{bmatrix}_t \quad (5.2)$$

where,  $0$ , is a  $2 \times 2$  zero matrix. Similarly, the matching matrix (equation (2.5)) is given by

$$\begin{bmatrix} E_x \\ H_y \\ E_y \\ -H_x \end{bmatrix}_i = \begin{bmatrix} M & 0 \\ 0 & M \end{bmatrix} \begin{bmatrix} E_x \\ H_y \\ E_y \\ -H_x \end{bmatrix}_t \quad (5.3)$$

where  $M$  represents the original  $2 \times 2$  matching matrix equation (2.5). For the wave plates the  $ABCD$  matrix of equation (2.1) becomes

$$\begin{bmatrix} E_x \\ H_y \\ E_y \\ -H_x \end{bmatrix}_i = \begin{bmatrix} W_x & 0 \\ 0 & W_y \end{bmatrix} \begin{bmatrix} E_x \\ H_y \\ E_y \\ -H_x \end{bmatrix}_t \quad (5.4)$$

where the  $W$  represent the original  $ABCD$  matrix and the subscripts denote which polarisations they are related to.

The wave plates' rotations and the subsequent transformations of the polarisations are obtained by placing equation (5.4) between a modified rotation matrix,  $\Theta$ , and its inverse,  $\Theta'$ . This modified rotation matrix is created by multiplying the elements of the standard 2D rotation matrix by a  $2 \times 2$  identity matrix,  $I$ , to produce:

$$\Theta = \begin{bmatrix} I \cos \theta & -I \sin \theta \\ I \sin \theta & I \cos \theta \end{bmatrix} \quad (5.5)$$

where  $\theta$  is the angle by which the wave plate's optic axis is rotated by. The inverse,  $\Theta'$ , is equal to

$$\Theta' = \begin{bmatrix} I \cos \theta & I \sin \theta \\ -I \sin \theta & I \cos \theta \end{bmatrix}. \quad (5.6)$$

The input polarisations are aligned to the  $x$ - and  $y$ -axes. The role of  $\Theta$  is to transform the polarisations so that they are aligned with the rotated  $x$ - and  $y$ -axes of the wave plate.  $\Theta'$  then transforms the polarisations back to their original alignment. Cascading the appropriate matrices one after the other allows for the modelling of a Pancharatnam type wave plate. So for example, to model two identical metamaterial wave plates rotated by,  $\theta_1$  and  $\theta_2$  respectively, separated

## 5: HIGHLY BIREFRINGENT ARTIFICIAL DIELECTRICS

by an air gap, the previous equations would yield:

$$\begin{bmatrix} E_x \\ H_y \\ E_y \\ -H_x \end{bmatrix}_i = \Theta_1 \begin{bmatrix} W_x & 0 \\ 0 & W_y \end{bmatrix} \Theta'_1 \begin{bmatrix} P_{\text{air}} & 0 \\ 0 & P_{\text{air}} \end{bmatrix} \Theta_2 \begin{bmatrix} W_x & 0 \\ 0 & W_y \end{bmatrix} \Theta'_2 \begin{bmatrix} E_x \\ H_y \\ E_y \\ -H_x \end{bmatrix}_t. \quad (5.7)$$

To obtain the reflection and transmission coefficients the  $E$  and  $H$  field quantities are replaced by their equivalent representations using incident, reflected and transmitted  $E$  field quantities. The incident and transmitted field quantities become

$$E_{xi} = E_x^i + E_x^r \quad (5.8a)$$

$$H_{xi} = H_x^i - H_x^r = Y(E_x^i - E_x^r) \quad (5.8b)$$

$$E_{yi} = E_y^i + E_y^r \quad (5.8c)$$

$$H_{yi} = H_y^i - H_y^r = Y(E_y^i - E_y^r) \quad (5.8d)$$

and

$$E_{xt} = E_x^t \quad (5.9a)$$

$$H_{xt} = H_x^t = Y E_x^t \quad (5.9b)$$

$$E_{yt} = E_y^t \quad (5.9c)$$

$$H_{yt} = H_y^t = Y E_y^t \quad (5.9d)$$

where  $Y = Y_0 n_{\text{env}}$  and  $n_{\text{env}}$  is the refractive index of the media surrounding the wave plate. Multiplying the  $4 \times 4$  matrices together and representing the resulting

matrix as  $Q$ , results in

$$\begin{bmatrix} E_x^i + E_x^r \\ Y(E_x^i - E_x^r) \\ E_y^i + E_y^r \\ Y(E_y^i - E_y^r) \end{bmatrix} = \begin{bmatrix} Q_{11} & Q_{12} & Q_{13} & Q_{14} \\ Q_{21} & Q_{22} & Q_{23} & Q_{24} \\ Q_{31} & Q_{32} & Q_{33} & Q_{34} \\ Q_{41} & Q_{42} & Q_{43} & Q_{44} \end{bmatrix} \begin{bmatrix} E_x^t \\ Y E_x^t \\ E_y^t \\ Y E_y^t \end{bmatrix}. \quad (5.10)$$

Multiplying out the matrix elements gives four linear equations:

$$E_x^i + E_x^r = (Q_{11} + YQ_{12})E_x^t + (Q_{13} + YQ_{14})E_y^t \quad (5.11a)$$

$$Y(E_x^i - E_x^r) = (Q_{21} + YQ_{22})E_x^t + (Q_{23} + YQ_{24})E_y^t \quad (5.11b)$$

$$E_y^i + E_y^r = (Q_{31} + YQ_{32})E_x^t + (Q_{33} + YQ_{34})E_y^t \quad (5.11c)$$

$$Y(E_y^i - E_y^r) = (Q_{41} + YQ_{42})E_x^t + (Q_{43} + YQ_{44})E_y^t \quad (5.11d)$$

that can be solved for  $E_{x,y}^r$  and  $E_{x,y}^t$ . The solutions can then be recast into matrix form:

$$2 \begin{bmatrix} E_x^i \\ E_y^i \end{bmatrix} = \begin{bmatrix} aT & bT \\ cT & dT \end{bmatrix} \begin{bmatrix} E_x^t \\ E_y^t \end{bmatrix} \quad (5.12)$$

and

$$2 \begin{bmatrix} E_x^r \\ E_y^r \end{bmatrix} = \begin{bmatrix} aR & bR \\ cR & dR \end{bmatrix} \begin{bmatrix} E_x^t \\ E_y^t \end{bmatrix} \quad (5.13)$$

where the matrix elements are defined as

$$aT = Q_{11} + YQ_{12} + ZQ_{21} + Q_{22} \quad (5.14a)$$

$$bT = Q_{13} + YQ_{14} + ZQ_{23} + Q_{24} \quad (5.14b)$$

$$cT = Q_{31} + YQ_{32} + ZQ_{41} + Q_{42} \quad (5.14c)$$

$$dT = Q_{33} + YQ_{34} + ZQ_{43} + Q_{44} \quad (5.14d)$$

and

$$aR = Q_{11} + YQ_{12} - ZQ_{21} - Q_{22} \quad (5.15a)$$

$$bR = Q_{13} + YQ_{14} - ZQ_{23} - Q_{24} \quad (5.15b)$$

$$cR = Q_{31} + YQ_{32} - ZQ_{41} - Q_{42} \quad (5.15c)$$

$$dR = Q_{33} + YQ_{34} - ZQ_{43} - Q_{44}. \quad (5.15d)$$

The final values of the reflection and transmission coefficients,  $S_{11}$  and  $S_{21}$ , for the  $x$ - and  $y$ -polarisations are given by  $E^r/E^i$  and  $E^t/E^i$  respectively by multiplying out the matrix elements of:

$$\begin{bmatrix} E_x^t \\ E_y^t \end{bmatrix} = 2 \begin{bmatrix} aT & bT \\ cT & dT \end{bmatrix}^{-1} \begin{bmatrix} E_x^i \\ E_y^i \end{bmatrix} \quad (5.16)$$

and

$$\begin{bmatrix} E_x^r \\ E_y^r \end{bmatrix} = \frac{1}{2} \begin{bmatrix} aR & bR \\ cR & dR \end{bmatrix} \begin{bmatrix} E_x^t \\ E_y^t \end{bmatrix} = \begin{bmatrix} aR & bR \\ cR & dR \end{bmatrix} \begin{bmatrix} aT & bT \\ cT & dT \end{bmatrix}^{-1} \begin{bmatrix} E_x^i \\ E_y^i \end{bmatrix}. \quad (5.17)$$

When solving the above matrix equations, each input polarisation,  $E_x^i$  and  $E_y^i$ , must be handled individually, e.g. to obtain  $E_x^t/E_x^i$ ,  $E_y^i$  is set to zero. For completeness the equations for the co-polarisations are shown:

$$\frac{E_x^t}{E_x^i} = \frac{2dT}{\Delta T} \quad (5.18)$$

$$\frac{E_x^r}{E_x^i} = \frac{bRcT - aRdT}{\Delta T} \quad (5.19)$$

$$\frac{E_y^t}{E_y^i} = \frac{2aT}{\Delta T} \quad (5.20)$$

$$\frac{E_y^r}{E_y^i} = \frac{aRdT - bRcT}{\Delta T}, \quad (5.21)$$

where  $\Delta T = aTdT - bTcT$ . Cross polarisations e.g.  $E_x^t/E_y^i$  can similarly be

calculated.

## 5.4 Air Gap Half Wave Plates

### 5.4.1 Theory & Application

Half Wave Plates (HWP) impart a phase difference of  $180^\circ$  between the two orthogonal polarisations of the incident radiation. Linearly polarised radiation that is incident on a HWP will have its polarisation angle rotated by  $2\theta$  where  $\theta$  is the angle between the radiation's polarisation angle and the HWP's optic axis, transforming it into the radiation's cross polarised form. Rotating HWPs are used as polarisation modulators. By placing a linearly polarised detector behind a HWP rotating at frequency,  $f$ , the detector becomes sensitive to different polarisation angles, with the detected intensity of any polarised signal varying with at a frequency of  $4f$ . Unpolarised radiation is unaffected by the HWP and the intensity of the signal detected from an unpolarised source remains constant. This allows for the distinguishing of polarised and unpolarised sources.

### 5.4.2 Design

To create the high birefringences described in section 5.3.1, we first looked the Vallecchi et al. (2009)'s Jerusalem Cross Pair (JCP) geometry. This design can be seen in figure 1.10b on page 50 and figure 2.1 on page 58. The Jerusalem cross is isotropic, displaying NRI behaviour for any incident polarisation. To make its unit cell birefringent, one of its arms was removed leaving behind a design referred to by Zhou et al. (2006) as a "dog bone" due to its shape (figure 5.2). The dog bone pair only displays NRI behaviour for radiation polarised along its central bar (the  $x$ -axis in figure 5.2). Radiation polarised along the orthogonal axis will only experience a PRI for the same frequency range.

A study was made to see whether a single unit cell consisting of this geometry

## 5: HIGHLY BIREFRINGENT ARTIFICIAL DIELECTRICS

could create a phase difference,  $\Delta\phi$ , of  $180^\circ$ . This was found to be possible if a triplet of dog bones were used in a single unit cell, with two dog bones on the outer surfaces of the substrate and the third embedded within it (figure 5.2). The design is referred to as a Dog Bone Triplet (DBT).

Using HFSS, optimisations were made that varied the dimensions of the copper dog bones and the thickness of the polypropylene substrate. The optimisations goals were set to achieve a  $\Delta\phi = \arg(S_{21}^x) - \arg(S_{21}^y) = -180^\circ$  with a transmitted intensity,  $|S_{21}|^2 \geq 0.8$ , along both axes at 92.5 GHz, the centre of the W-band (75 GHz to 110 GHz). The final design is shown in figure 5.2 with the dimensions noted in the caption.

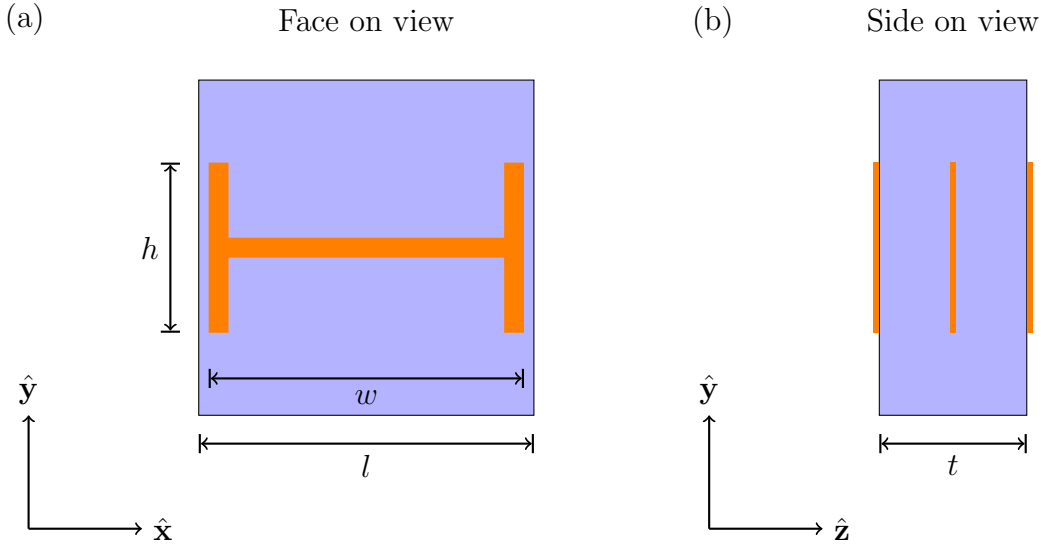


Figure 5.2: Schematic of Dog Bone Triplet (DBT) cell. The copper is coloured orange and the polypropylene is blue. The dimensions are:  $h = 300 \mu\text{m}$ ,  $w = 556 \mu\text{m}$  and  $l = 591 \mu\text{m}$ . The first version of the design used  $t = 260 \mu\text{m}$ . The second version used  $t = 264 \mu\text{m}$ . The copper tracks are  $35 \mu\text{m}$  wide and  $2 \mu\text{m}$  thick.

A frequency sweep of this single unit cell over the W-band showed that at 92.5 GHz the transmitted intensity along both the  $x$ - and  $y$ -axes were above 0.8 (figure 5.3). The phase difference crossed  $-180^\circ$  at 92.95 GHz (figure 5.4). Using  $\Delta\phi = (-180 \pm 3)^\circ$ , to define the usable bandwidth a wave plate made of a single DBT had a fractional bandwidth of only 0.3% between 92.8 GHz to 93.1 GHz. In

this region, the mean transmitted intensities along the  $x$ - and  $y$ -axes were 0.81 and 0.84 respectively. It can be seen from figure 5.4 that the very narrow bandwidth is caused by the steep gradient of the phase difference. The steep gradient arises from the resonance experienced by  $x$ -polarised radiation, the same that cause the NRI band. Using the physical thickness of the unit cell to provide an indicative value (last paragraph of section 4.2.2) of the refractive indices,  $n_x$  and  $n_y$ , for the  $x$ - and  $y$ -polarised radiations respectively we find that a NRI is created above 89.6 GHz for  $x$ -polarised radiation (figure 5.5). The calculated value of  $\text{Re}(n_x)$  remains negative as the frequency increases. However,  $|S_{21}|^2$  decreases sharply too, going below 0.01 or  $-20$  dB, above 100 GHz. Therefore  $\text{Re}(n_x)$  cannot be said to be accurate in these regions.  $\text{Re}(n_y)$  is constant at 1.7 across the whole W-band (figure 5.6).

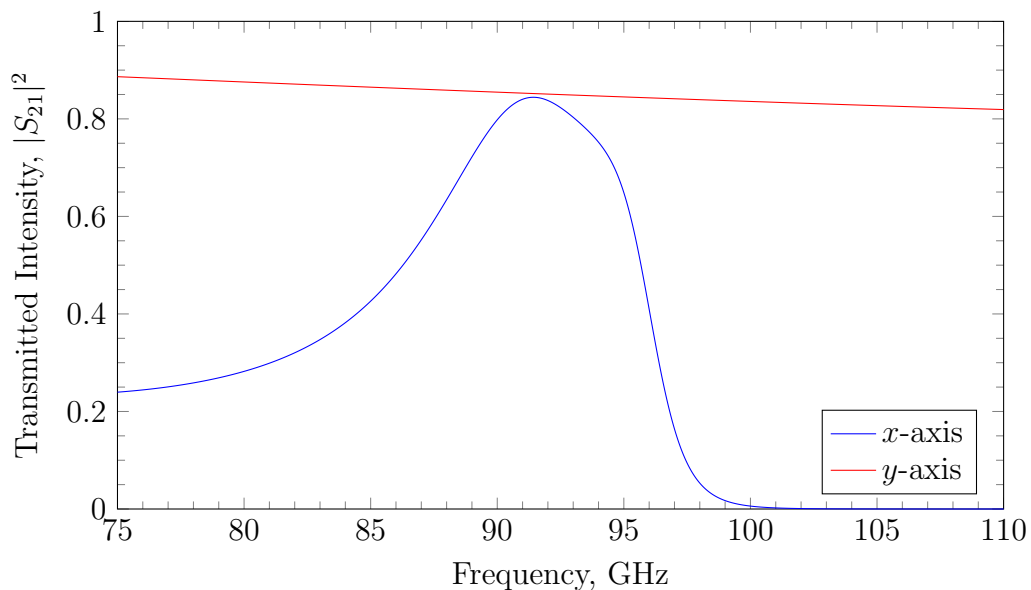


Figure 5.3: HFSS simulated transmitted intensity,  $|S_{21}|^2$ , of  $x$ - and  $y$ - polarised radiation after passing through a single Dog Bone Triplet (DBT).

To extend the usable bandwidth, the Pancharatnam method described in section 5.3.2 was applied using three DBT-HWPs separated by air gaps (figure 5.7). The differential evolution code (Storn and Price 1997) was used to optimise the rotation angles of the three plates as well as the thickness of the air gaps between

## 5: HIGHLY BIREFRINGENT ARTIFICIAL DIELECTRICS

them. The goal was to maximise the bandwidth where  $\Delta\phi = (-180 \pm 3)^\circ$  and do so in a way that  $|S_{21}|^2$  along the  $x$ - and  $y$ -axes were equal to each other. Using the nomenclature of figure 5.7 the final results came to require the three HWPs

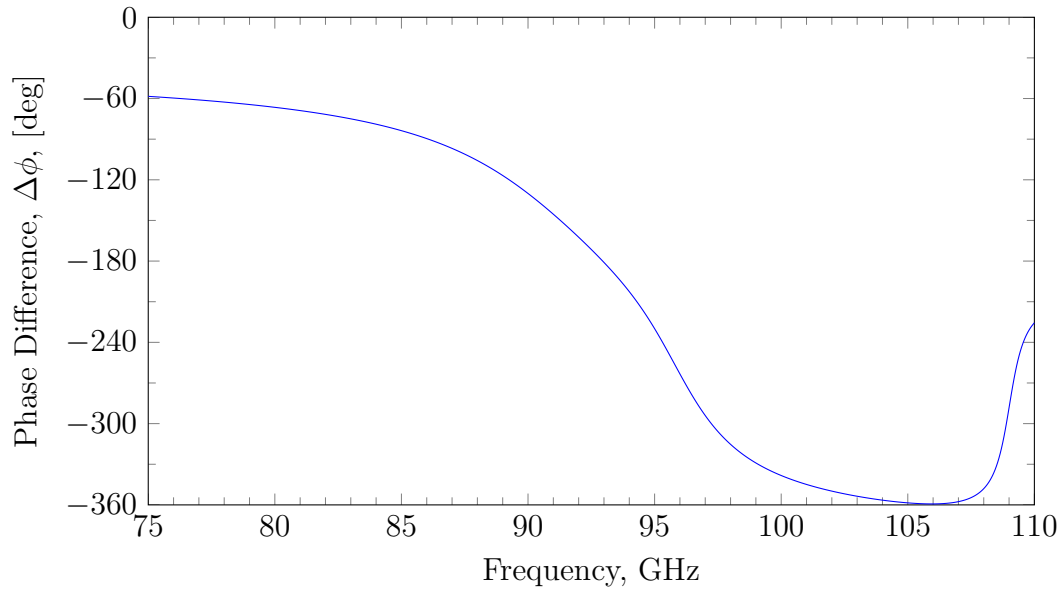


Figure 5.4: HFSS simulated phase difference,  $\Delta\phi$ , between the  $x$ - and  $y$ - polarised radiation after passing through a single Dog Bone Triplet (DBT).

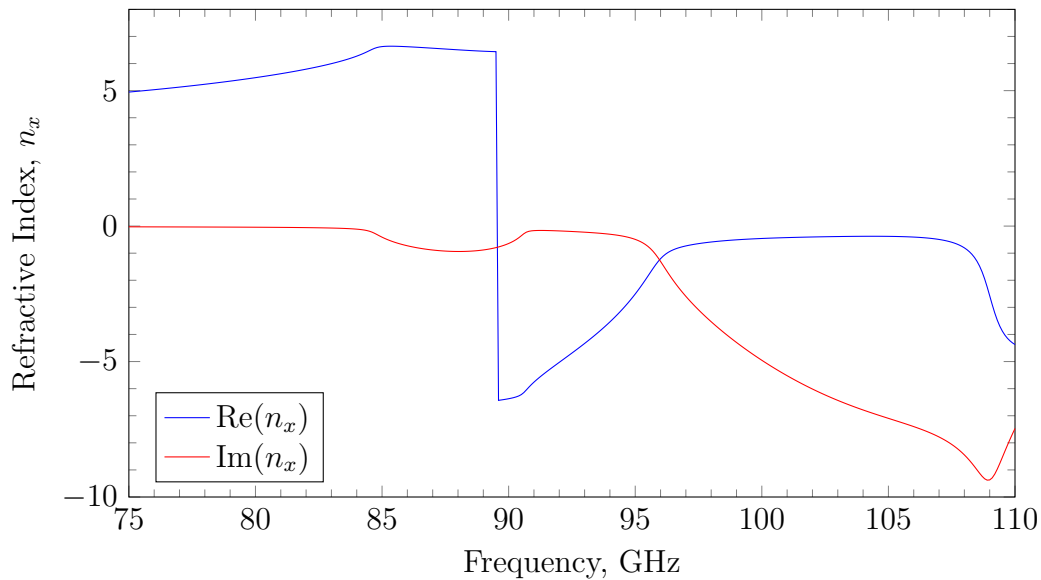


Figure 5.5: The refractive indices along the  $x$ -axis calculated from HFSS simulation data of a single Dog Bone Triplet (DBT).

to be rotated by angles  $\theta_1 = 30^\circ$  and  $\theta_2 = -29^\circ$ , each separated by an air gap,  $d_1 = 1.3$  mm.

With these optimised results, the TL based code predicted an increase in the usable fractional bandwidth from the 0.3% of a single HWP to 6.6% corresponding to a frequency range from 88.8 GHz to 94.9 GHz (figure 5.9). This is an increase of 22 times and shows that despite the phase difference's initially

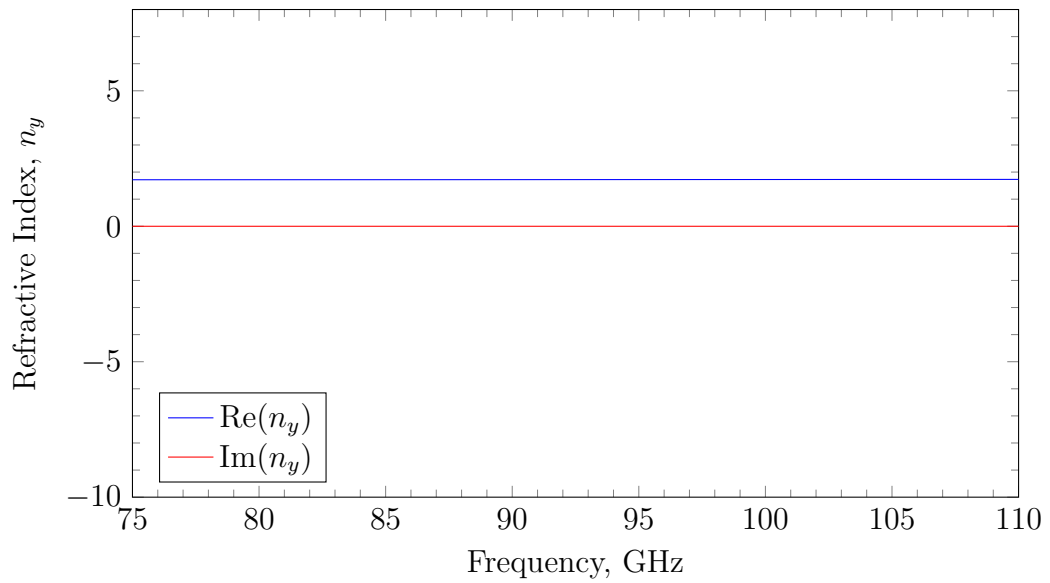


Figure 5.6: The refractive indices along the  $y$ -axis calculated from HFSS simulation data of a single Dog Bone Triplet (DBT).

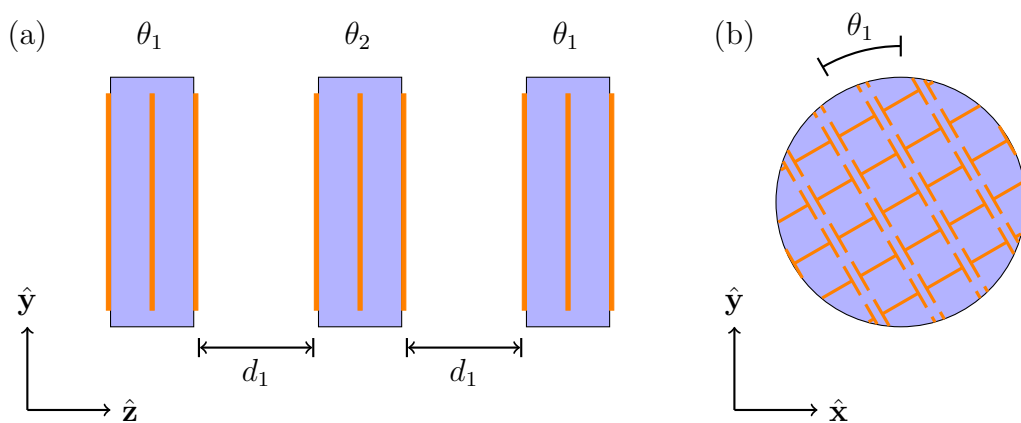


Figure 5.7: (a) Side on schematic of the Pancharatnam half wave plate. (b) Face on view.

steep gradient, the Pancharatnam method is still applicable. Within this band the transmitted intensities along the  $x$ - and  $y$ -axes show similar values to each other, varying between 0.36 and 0.72 along the  $x$ -axis and 0.36 and 0.73 along the  $y$ -axis (figure 5.8).

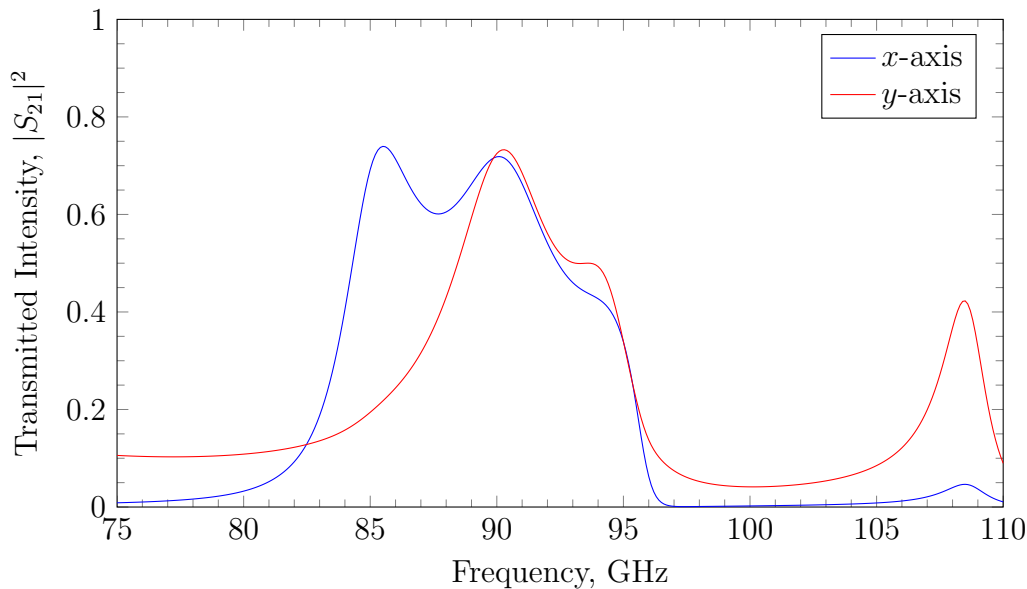


Figure 5.8: Transmitted intensity,  $|S_{21}|^2$ , of Pancharatnam based Half Wave Plate (HWP) (figure 5.7) calculated with the TL based code.

### 5.4.3 Manufacture

The manufacture of the grids took place as described in section 3.2.1 using 9.2 cm diameter samples. The original grid “recipe” (figure 5.10a) called for a substrate thickness of 260  $\mu\text{m}$ . This could be constructed with three grids on a 65  $\mu\text{m}$  substrate and one additional 65  $\mu\text{m}$  polypropylene substrate spacer. The preparation of the copper coated 65  $\mu\text{m}$  thick sheets proved to be troublesome. During the annealing stage in the fan oven (section 3.2.1.1), the polypropylene substrates became bumpy due to an unoptimised temperature profile for that particular substrate thickness (M. W. Ng, personal communications, 2011). For this reason the grid recipe was updated and a second recipe was made that used 47  $\mu\text{m}$  substrate for the grids and 38  $\mu\text{m}$  polypropylene spacers to create a substrate

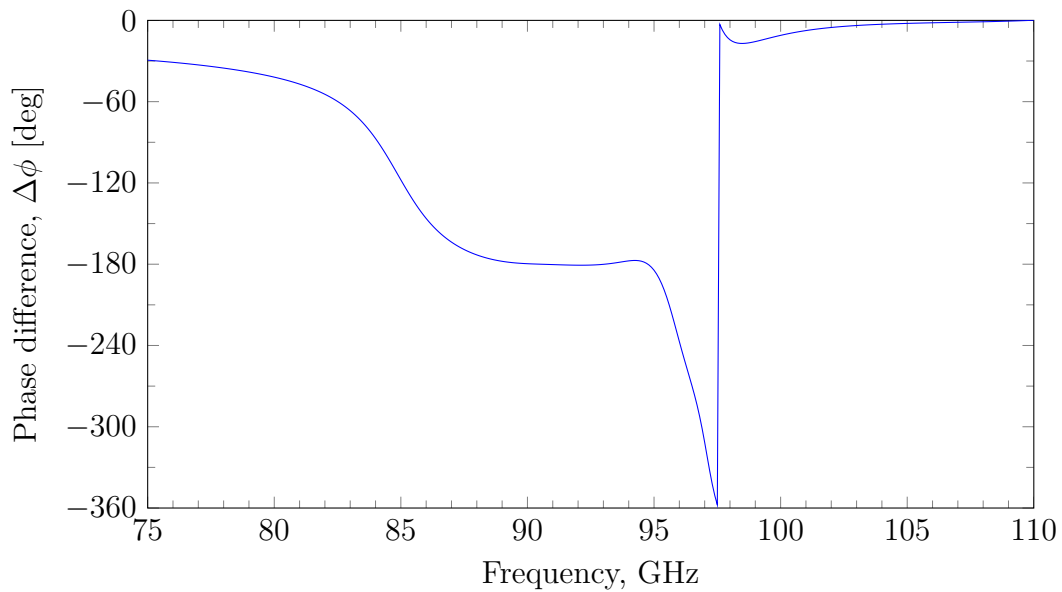


Figure 5.9: Transmitted phase difference,  $\Delta\phi$ , of Pancharatnam based Half Wave Plate (HWP) (figure 5.7) calculated with the TL based code.

thickness of  $264\ \mu\text{m}$  (figure 5.10b). When making the second version, a batch of sixteen DBT grids were made. From these, the best nine were picked based on VNA transmission measurements

The alignment of the grids followed a procedure similar to that described in section 3.3.1. The alignment was assessed with a linen loupe at various points across the grids area. Alignment was made more difficult due to the parallax effect caused by the  $130\ \mu\text{m}$  separation between the grids and hand held nature of the loupe to keep it parallel to the grid's surface and at the correct distance to focus them. An attempt to combat this issue was made by using two smaller glass blocks stacked on top of one another to rest the loupe horizontally at an appropriate height.

The  $1.3\ \text{mm}$  air gaps were created by mounting the bonded HWPs onto  $9.2\ \text{cm}$  diameter aluminium rings of the same thickness as described in mounting portion of section 3.2.1.1. The excess grids were cut away. The angles  $30^\circ$  and  $-29^\circ$  were marked with ink onto the edge of the grids and the circumference of the aluminium rings. These markings would later be used to aid in the alignment of the three

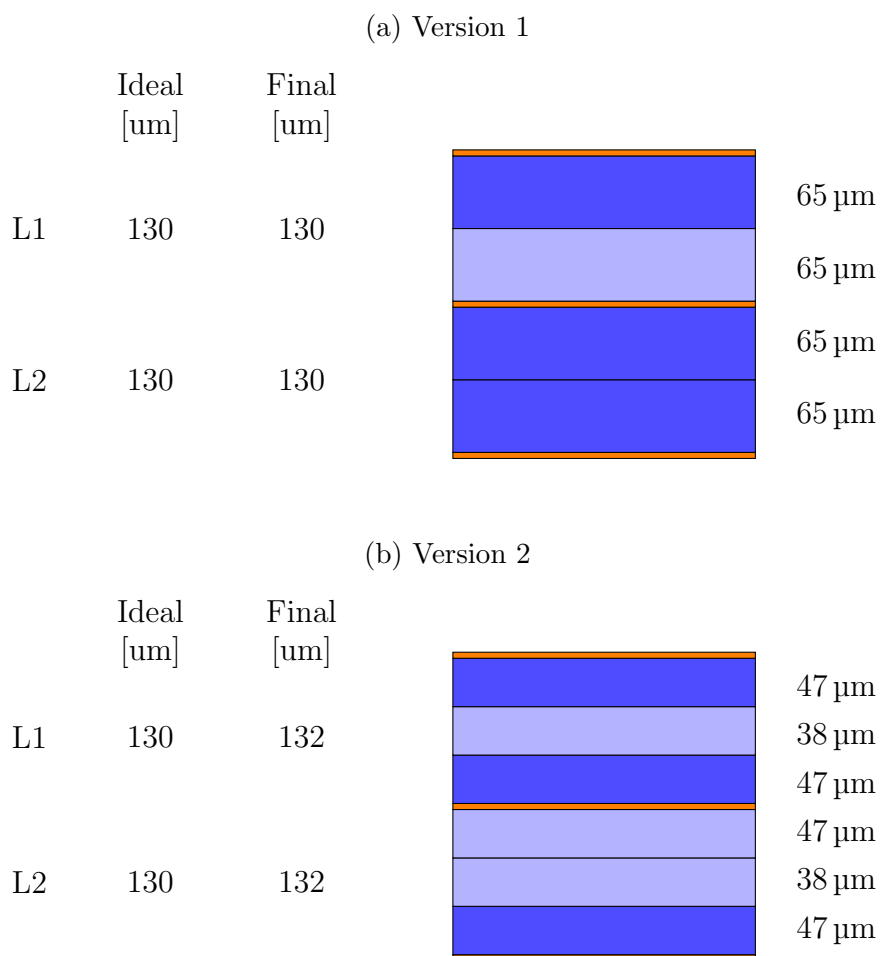


Figure 5.10: The recipes for the Dog Bone Triplet Half Wave Plates (DBT-HWPs). In the above drawings the copper is represented by orange and their associated polypropylene substrate by dark blue. Plain polypropylene spacers are coloured light blue. The ideal and final columns indicate the ideal thickness of the polypropylene between the copper and the closest possible thickness achievable with the available polypropylene sheets. The thickness of the separate polypropylene sheets are noted to the right of the drawing.

DBT-HWPs when the full HWP was constructed.

#### 5.4.4 Measurements

The 9.2 cm diameter rings were smaller than the standard 12 cm and 21 cm rings used by the Technology Group, so a special holder was manufactured to mount the three DBT-HWPs together. The experimental set up for the transmission

readings, shown in figure 5.11, is similar to one described in section 4.3.5 for the NRI slab.

The off-axis set up was utilised for these transmission measurements. Cross polarisation is a valid concern when using this set up to obtain transmission data, where accurate readings in two polarisations are required. However, if the horns are set up so that there is a mirror symmetry between them i.e. 1) they are at the same height, 2) they have the same off-axis angle and 3) their polarisations are the same, then no cross polarisation effects should occur. The symmetry ensures that the wave plate is illuminated by equivalent sections of the Gaussian shaped beams emitted from the horns, hence eliminating cross polarisation.

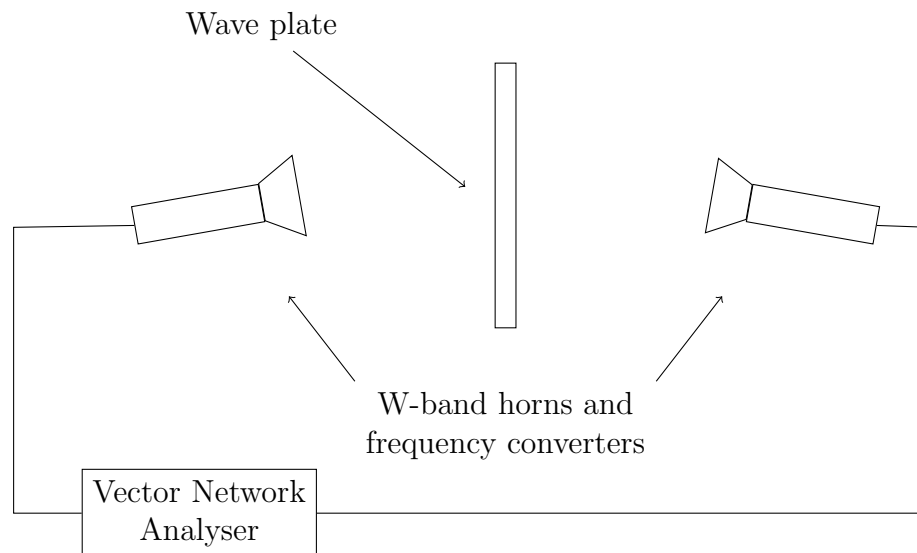


Figure 5.11: Schematic outline of the experimental set up.

### 5.4.5 Results

The experimental results from the first version of the Pancharatnam based HWP are displayed in figure 5.12 and figure 5.13 as solid lines against the expected results from the TL based model shown as dashed lines. The transmitted intensity readings in figure 5.12 show a good agreement along both axes with the model, albeit with a small red shift of  $\sim 1$  GHz. The transmission along the  $y$ -axis also

## 5: HIGHLY BIREFRINGENT ARTIFICIAL DIELECTRICS

falls off faster than expected above 93 GHz. The phase difference (figure 5.13) also shows a good agreement between the modelled and experimental data, between 75 GHz to 87 GHz. Above this, the experimental data diverges from the model and flattens out at  $-150^\circ$  between 87 GHz to 93.5 GHz, a fractional bandwidth of 7.7%.

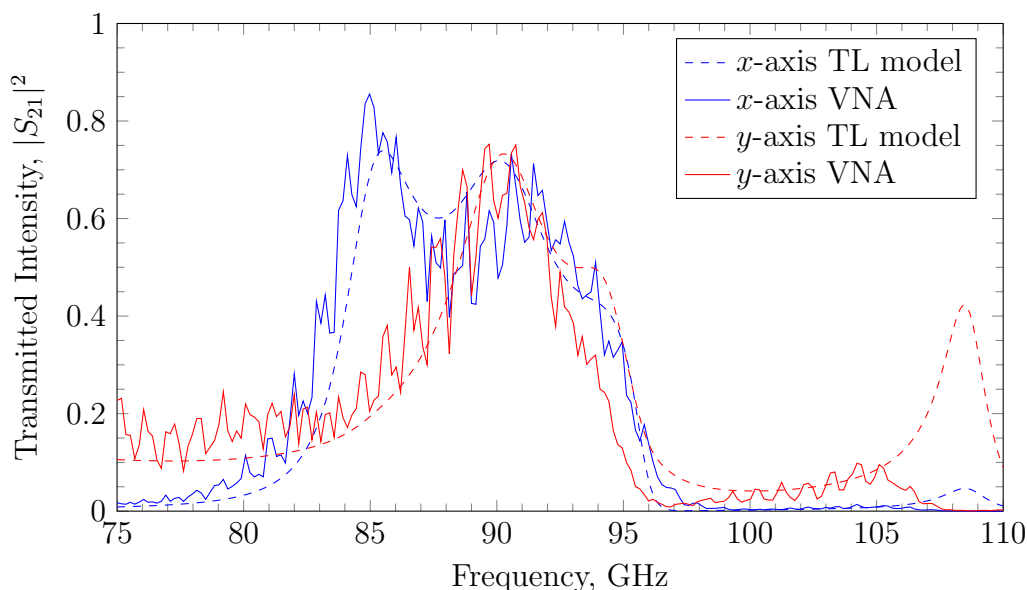


Figure 5.12: The expected and experimental transmitted intensities,  $|S_{21}|^2$ , as modelled by the TL based code (dashed lines) and from the VNA readings (solid lines) respectively.

The cause for this discrepancy was due to the poor performance of the individual DBT-HWPs, itself caused by poor alignment of the Dog Bone grids (figure 5.14). When transmission readings were taken of the individual plates it was seen that all three DBT-HWPs underperformed by varying amounts. While HFSS simulations predicted a phase difference of  $-181^\circ$  at 93 GHz the three wave plates produced phase differences of  $-164^\circ$ ,  $-175^\circ$  and  $-124^\circ$ . When placed together according to the required recipe the flat region also shifted up as a result. As shown in figure 5.15 the phase differences of DBT-HWP 1 and 2 closely follow the expected dashed curve of the HFSS simulation but flatten off above 97 GHz. DBT-HWP 3 performs the worst and does not match with the HFSS simulation above  $\sim 85$  GHz.

The data shown in figure 5.15 is from time gated readings, hence their smoother appearance than in graphs such as figure 5.13. It is also the source of the oscillations above 105 GHz due to the time gate chosen.

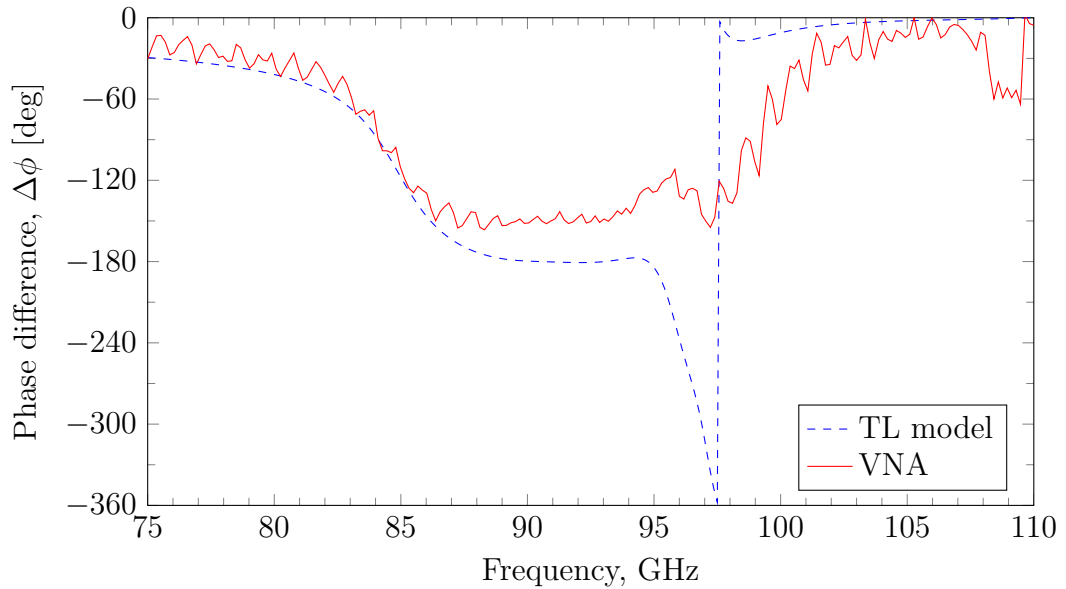


Figure 5.13: The differential phase,  $\Delta\phi$ , between the transmitted radiation's  $x$ - and  $y$ -axes.

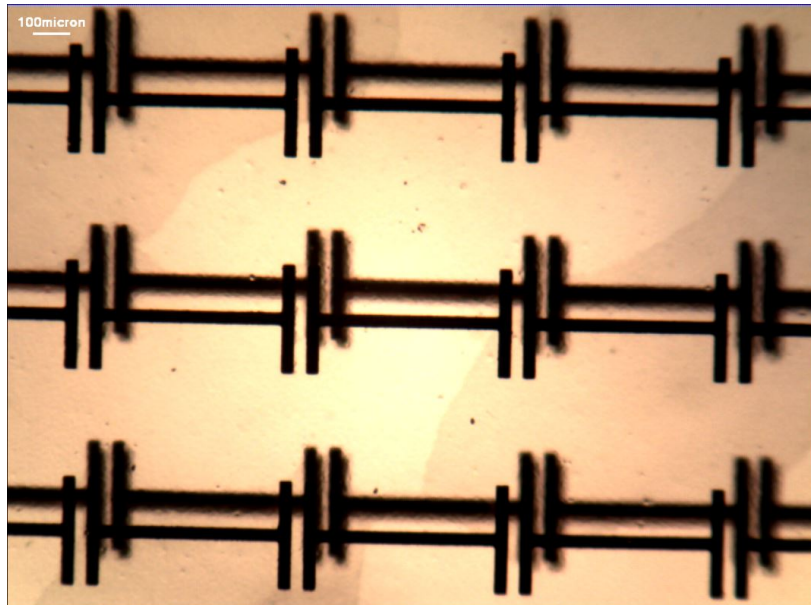


Figure 5.14: An example of the misalignment between the individual layers that make up the Dog Bone Triplets (DBT).

5: HIGHLY BIREFRINGENT ARTIFICIAL DIELECTRICS

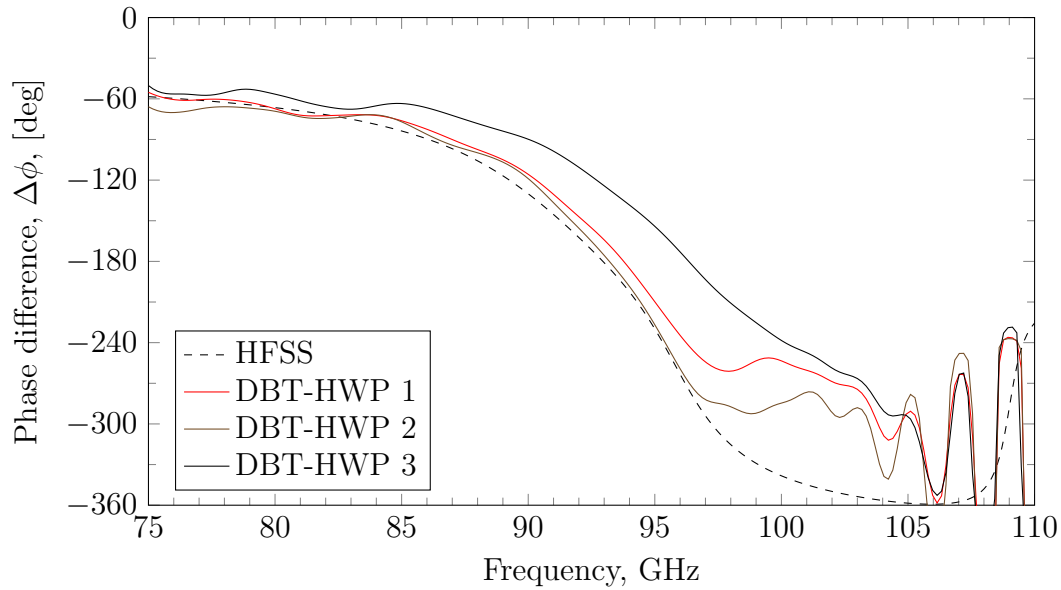


Figure 5.15: The measured transmitted phase differences (solid lines) of the individual DBT-HWPs that made the first version of the Pancharatnam based HWP compared to the expected result as simulated by HFSS (dashed).

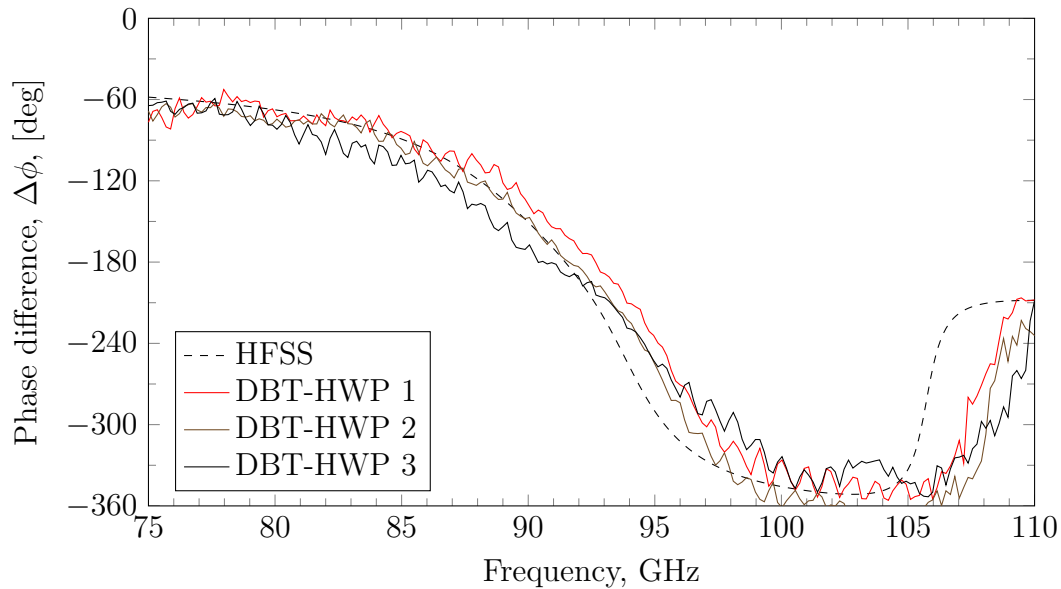


Figure 5.16: The measured transmitted phase differences (solid lines) of the individual DBT-HWPs that made the second version of the Half Wave Plate (HWP) compared to the expected result as simulated by HFSS (dashed).

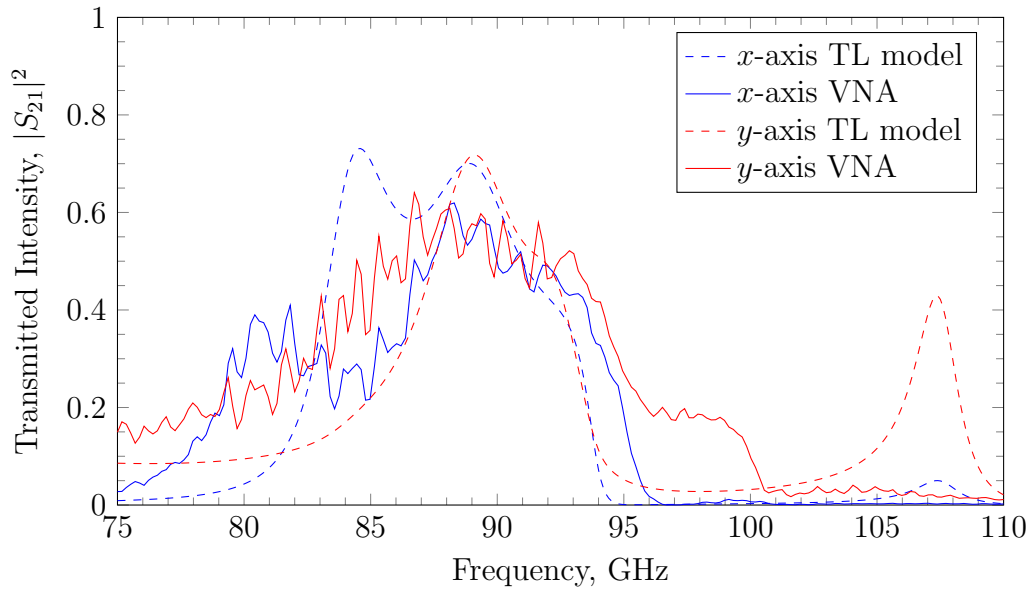


Figure 5.17: The experimental and expected transmitted intensities,  $|S_{21}|^2$ , as modelled by the TL based code (dashed lines) and from the VNA readings (solid lines) respectively of the second version of the Half Wave Plate (HWP).

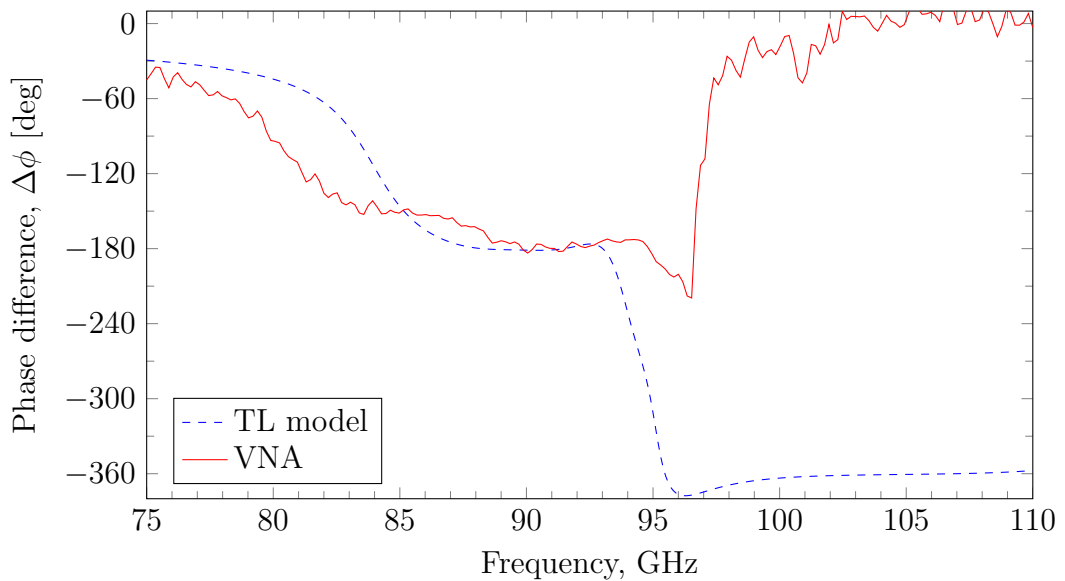


Figure 5.18: The differential phase,  $\Delta\phi$ , between the transmitted radiation's  $x$ - and  $y$ -axes of the second version of the Half Wave Plate (HWP).

As mentioned, a second version of the HWP was produced. For this version, the performance of the individual DBT-HWP's was measured before the full HWP was assembled. Figure 5.16 shows the results and it can be seen that the performance is much improved. Transmission measurements with the full HWP show less agreement in terms of the transmitted intensity readings (figure 5.17) with the experimental results appearing to be flatter with lower peak transmission values and broader pass band. *However*, the phase difference readings (figure 5.18) on the other hand have improved greatly when compared to the first version. A flattening of the phase difference at  $(-180 \pm 3)^\circ$  is observed for 3.1% between 89.86 GHz to 92.68 GHz.

## 5.5 Embedded Quarter Wave Plates

### 5.5.1 Theory & Applications

Quarter Wave Plates (QWP) impart a  $90^\circ$  phase difference between the two polarisations orthogonal components of radiation. They can be used to convert circularly polarised radiation into linearly polarised radiation, and vice versa. This ability is used in radio communications and advanced radar systems. In such systems the detectors are only sensitive to linearly polarised radiation in a single orientation. To detect or send signals polarised along the orthogonal axis would normally require the rotation of the entire antenna and detector system. This could be inconvenient if the systems are large and massive (Wu 1994). Rather than rotating the system, wave plates can be used to rotate the polarisation of the signals being sent and received. QWPs are useful when left-handed and right-circular polarisations are being used. The ability to send and receive signals in both polarisations in the same frequency band is known as frequency reuse and it allows a doubling of the data capacity of the frequency band in use (Elbert 1987).

### 5.5.2 Design

To improve the performance of the air gap designs used for the HWP, an embedded design was chosen for this QWP. The advantages of embedding grids within polypropylene are briefly described in section 4.3.1. A move to the cut wire pair (CWP) geometry for the unit cell rather than reusing the dog bone geometry used for the HWP was made in an attempt to reduce the absorption caused by the large capacitance between the arms of the neighbouring unit cells. The CWP geometry has been used previously in e.g. Tung et al. (2010) and Weis et al. (2009) to produce NRI. As mentioned in section 5.3.2 the latter paper used CWPs to create highly birefringent wave plates by supporting negative and positive refractive indices.

A HFSS simulation was run to optimise the dimensions and the separation of the copper parts to achieve a  $\Delta\phi$  of  $90^\circ$  and  $|S_{21}|^2$  in the  $x$ - and  $y$ -axes of 0.9 or greater at 102 GHz. To account for the copper being completely embedded within polypropylene, the “air box” was filled with polypropylene as opposed to a vacuum as in the previous HWP simulations. When setting the optimisation goal for the phase difference in HFSS, entering it as  $\arg(S_{21}^x) - \arg(S_{21}^y) = \Delta\phi = 90^\circ$  was insufficient because HFSS may calculate a value of  $-90^\circ$  or  $270^\circ$  which are both equivalent to  $90^\circ$  for our purposes. This was resolved by instead using  $\arccos[\cos(\Delta\phi)]$  in place of  $\Delta\phi$ . This works because the cosine function is periodic so angles equivalent to  $90^\circ$ , such as  $270^\circ$ , will all return 0. The arccosine function is programmed in HFSS to return an angle in the range  $0^\circ$  to  $180^\circ$ , so when the result of  $\cos(\Delta\phi)$  is 0, the arccosine function will return  $90^\circ$ . The final dimensions are shown in the caption to figure 5.19.

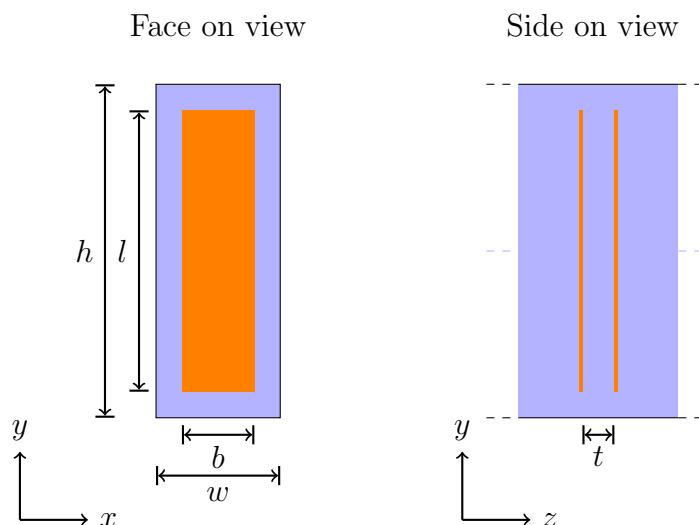


Figure 5.19: Schematic of cut wire pair cell. The copper is coloured orange and the polypropylene is blue. The dashed lines in (b) are to indicate that the polypropylene substrate continues on to the sides because the CWP was optimised and modelled as a structure embedded within an infinite medium of polypropylene. The dimensions are:  $w = 365 \mu\text{m}$ ,  $h = 980 \mu\text{m}$ ,  $l = 827 \mu\text{m}$  and  $b = 312 \mu\text{m}$ ,  $g_1 = 76 \mu\text{m}$ ,  $g_2 = 76.5 \mu\text{m}$  and  $t = 94 \mu\text{m}$ . The copper wires are  $2 \mu\text{m}$  thick.

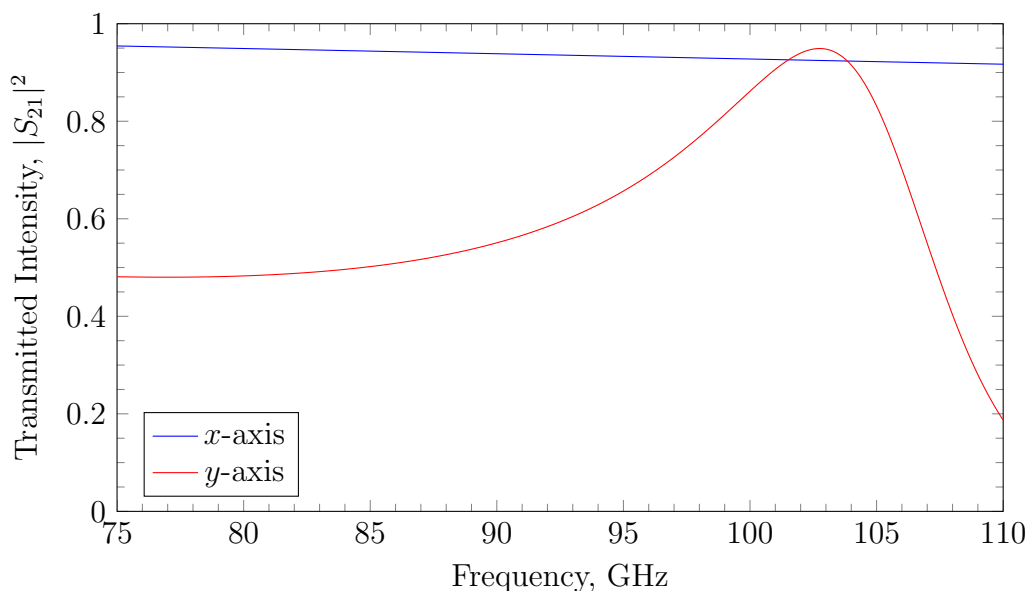


Figure 5.20: HFSS simulated transmitted intensity,  $|S_{21}|^2$ , data of the cut wire pair geometry embedded within polypropylene.

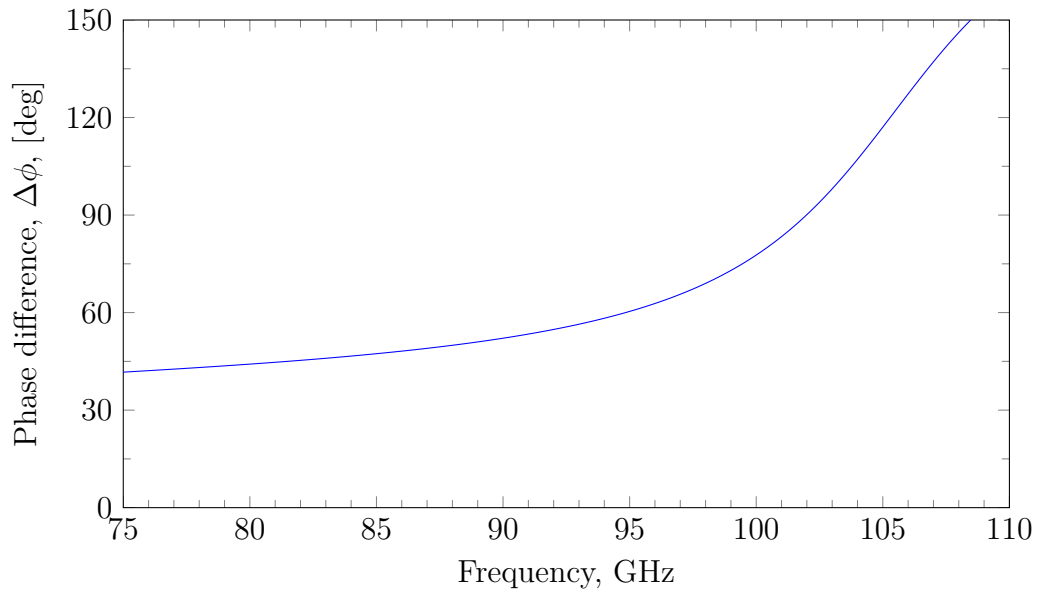


Figure 5.21: HFSS simulated transmitted phase difference,  $\Delta\phi$ , data of the cut wire pair geometry embedded within polypropylene.

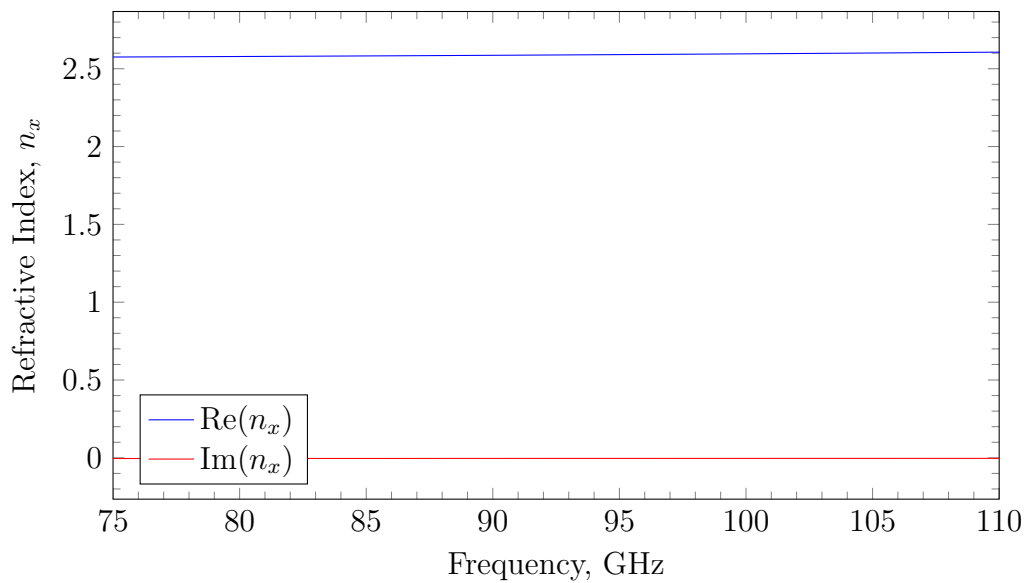


Figure 5.22: The refractive index along the  $x$ -axis calculated from HFSS simulation data.

5: HIGHLY BIREFRINGENT ARTIFICIAL DIELECTRICS

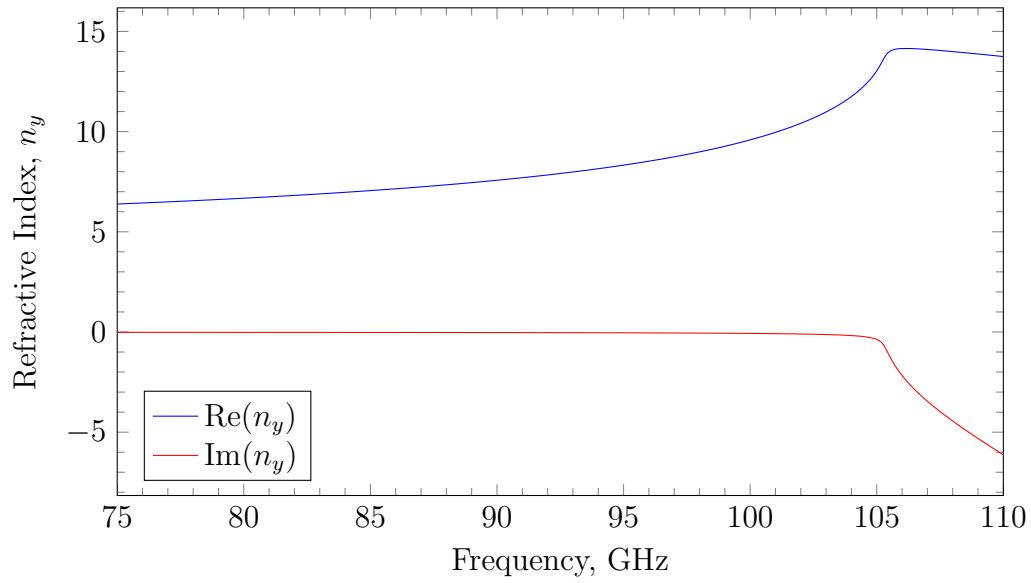


Figure 5.23: The refractive index along the  $y$ -axis calculated from HFSS simulation data.

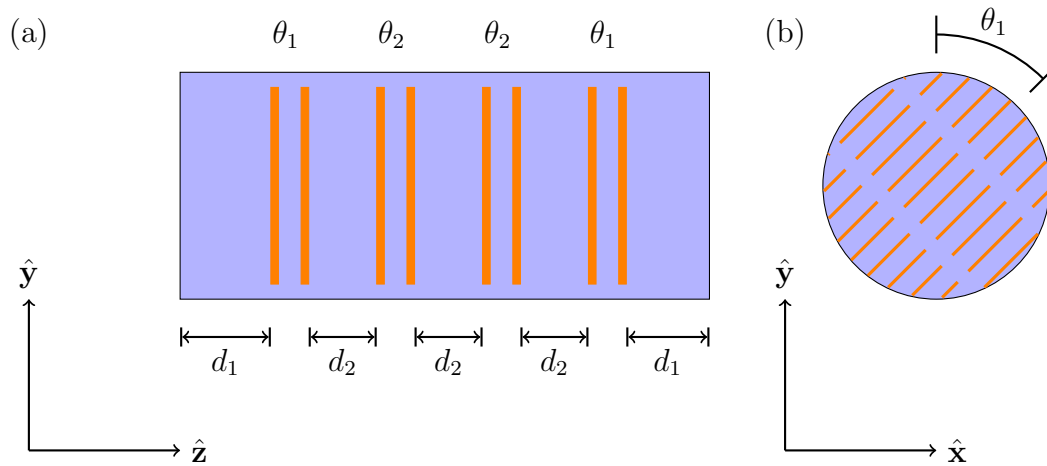


Figure 5.24: (a) Side on view of the Pancharatnam quarter wave plate. (b) Face on view.

The frequency sweep of the transmitted intensities and differential phase of the optimised unit cell are shown in figures 5.20 to 5.21. Defining the usable bandwidth for the QWP as the region where  $\Delta\phi = (90 \pm 2)^\circ$ , a single CWP is able to work at 101.7 GHz to 102.3 GHz giving it a fractional bandwidth of 0.6%. Within this band the mean transmitted intensity is 0.93 and 0.94 along the  $x$ - and  $y$ -axes respectively.  $x$ -polarised transmission remains above 0.9 across the entire W-band, whilst the  $y$ -axis shows a resonance peaking to 0.95 at 102.8 GHz. Again the physical thickness was used as the effective thickness in our calculations of  $n_x$  and  $n_y$ . The results are shown in figure 5.22 and figure 5.23 respectively. Here we see that the no negative band has been achieved, the high birefringence instead being produced by high positive values of the refractive index.

To broaden the usable bandwidth a Pancharatnam recipe based on the use of four cascaded QWP completely embedded within polypropylene was employed (figure 5.24). The TL code used for the HWP design was modified to include an extra wave plate as well the matching matrix from equation (2.5) to take into account the effect of radiation passing from air to polypropylene and vice versa. An optimisation was run that would vary 1) the individual rotation angles of the four wave plates, 2) the separation between them and 3) the thickness of the polypropylene between the outermost wave plates and air with the goal of maximising the usable bandwidth whilst keeping  $|S_{21}|^2$  along both axes  $\geq 0.8$ . Using the nomenclature of figure 5.24, the final optimised parameters required that the first and fourth QWP be rotated by  $\theta_1 = -45^\circ$ , whilst the second and third are rotated by  $\theta_2 = 17^\circ$ . The separation between the wave plates was  $d_2 = 1320 \mu\text{m}$  and the polypropylene thicknesses at the ends were  $d_1 = 630 \mu\text{m}$ .

With these optimised results, the TL based code predicted a 13 times increase in the usable fractional bandwidth (figure 5.26) from 0.6% to 7.8% between 86.2 GHz to 93.1 GHz.

5: HIGHLY BIREFRINGENT ARTIFICIAL DIELECTRICS

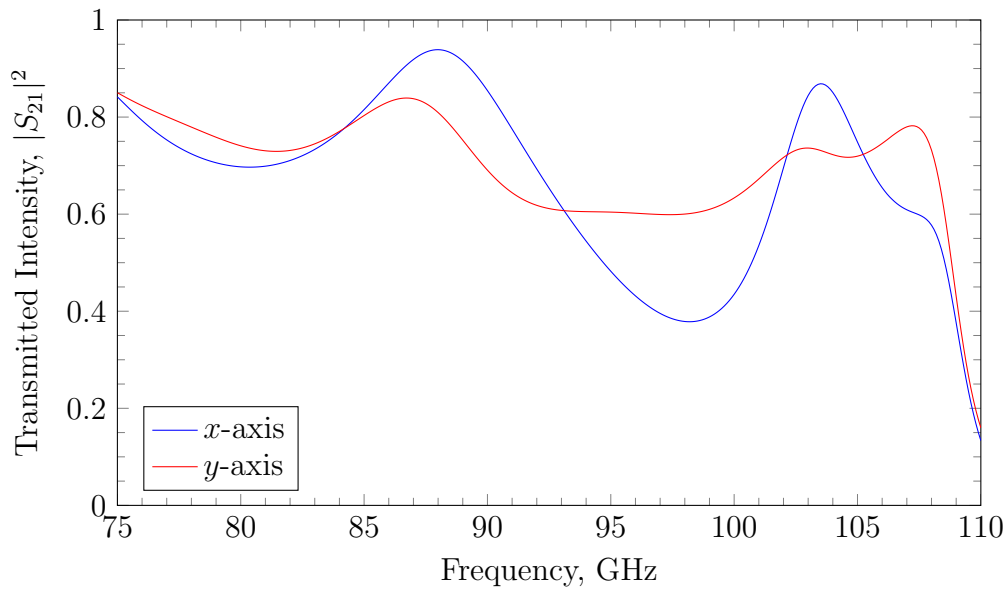


Figure 5.25: The transmitted intensity,  $|S_{21}|^2$ , of the embedded Pancharatnam QWP (figure 5.24) calculated by the TL based code.

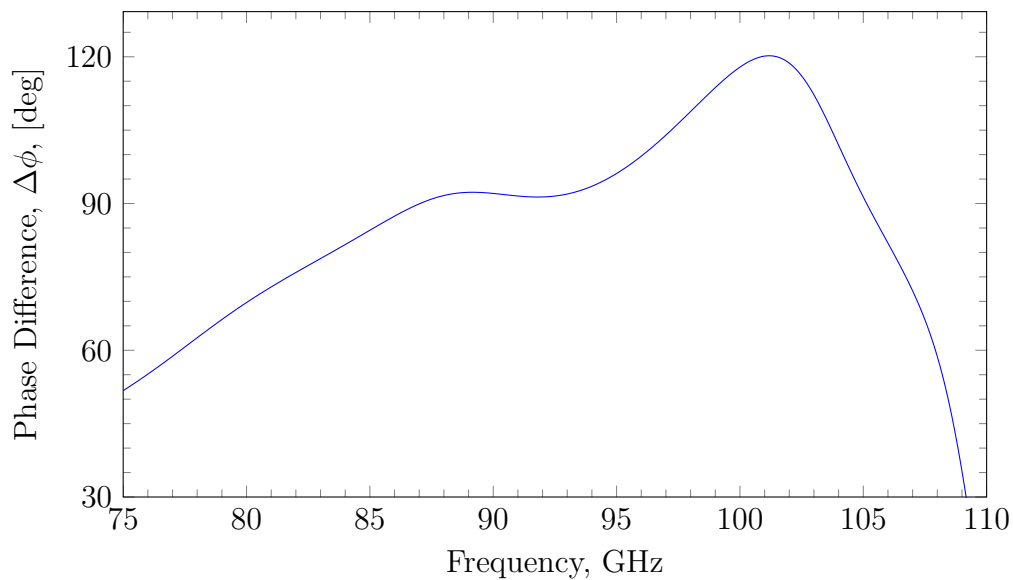


Figure 5.26: The transmitted phase difference,  $\Delta\phi$ , of the embedded Pancharatnam QWP (figure 5.24) calculated by the TL based code.

### 5.5.3 Manufacture

The manufacturing of the grids followed the procedure outlined in section 3.2.1 using 12 cm diameter samples. The photo mask had alignment marks located on the circumference identifying the compass points and the locations of the angles  $-45^\circ$  and  $17^\circ$ . Unlike the air gap half wave plate, for the embedded quarter wave plate the recipe was broken down into eight layers that were pre-bonded as described in section 3.3.1. This reduced the number of separate layers that required handling. Each layer is denoted by the dashed red lines in figure 5.27. The thickness of the polypropylene at the ends was reduced to  $629\mu\text{m}$  because this is the closest achievable thickness with the commercially available polypropylene sheets.

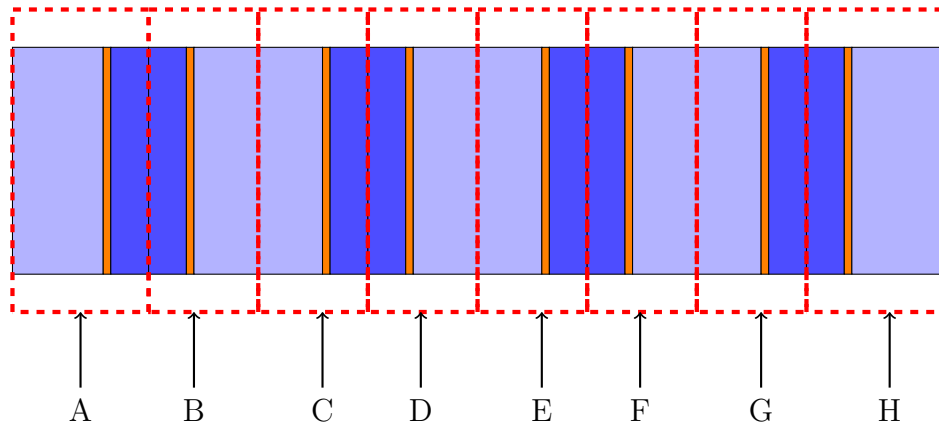


Figure 5.27: Recipe for the four unit cell structure of the full quarter wave plate consisting of eight cut wire pair grids. The copper is represent by orange, the polypropylene substrate associated with the copper is dark blue and the polypropylene spacers are light blue. The dashed red outline denote how the individual polypropylene sheets were divided into layers A to H before alignment.

Following a similar procedure described in section 4.3.4 for the NRI slab, prior to alignment, but after the pre-bonding, transmission readings were taken of the individual layers to asses their performance. The transmitted intensity and transmitted phase of layer A is shown in figure 5.28 and figure 5.29 as an example. Similar results were achieved for the other layers. The layers were then paired up, A with B, C with D etc., aligned and spot welded to form the CWP QWPs.

## 5: HIGHLY BIREFRINGENT ARTIFICIAL DIELECTRICS

Again, transmission readings were taken with these four spot welded QWPs to test performance. Alignment and hot pressing of the full QWP structure was then carried out.

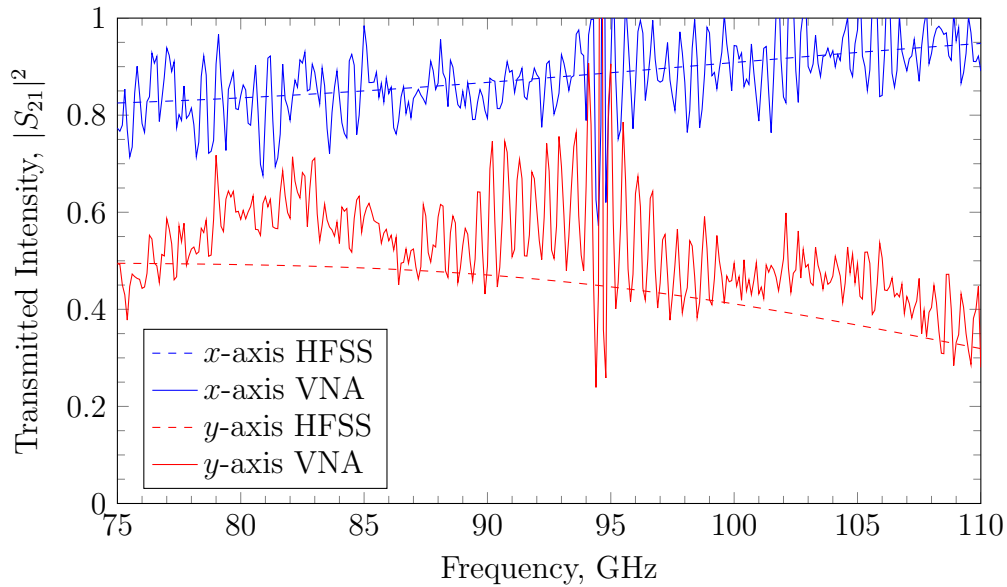


Figure 5.28: Transmitted intensity readings of layer A measured experimentally (solid) compared to the data from a HFSS simulation (dashed) of the same layer.

### 5.5.4 Measurements

Measurements were carried out in a similar way as the HWP in section 5.4.4. The difference being that a proper sample holder was able to be used owing to the larger 11 cm diameter of the QWP. The process of taking the readings was found to be easier for the quarter wave plate than the HWP owing to the fact that the QWP existed as a single rigid structure.

### 5.5.5 Results

The results of the spot welded CWP-QWP made from layers G and H are shown in figure 5.30 and figure 5.31 as an example. The transmitted intensity readings (figure 5.30) along both the  $x$ - and  $y$ -axes show a good match to the HFSS

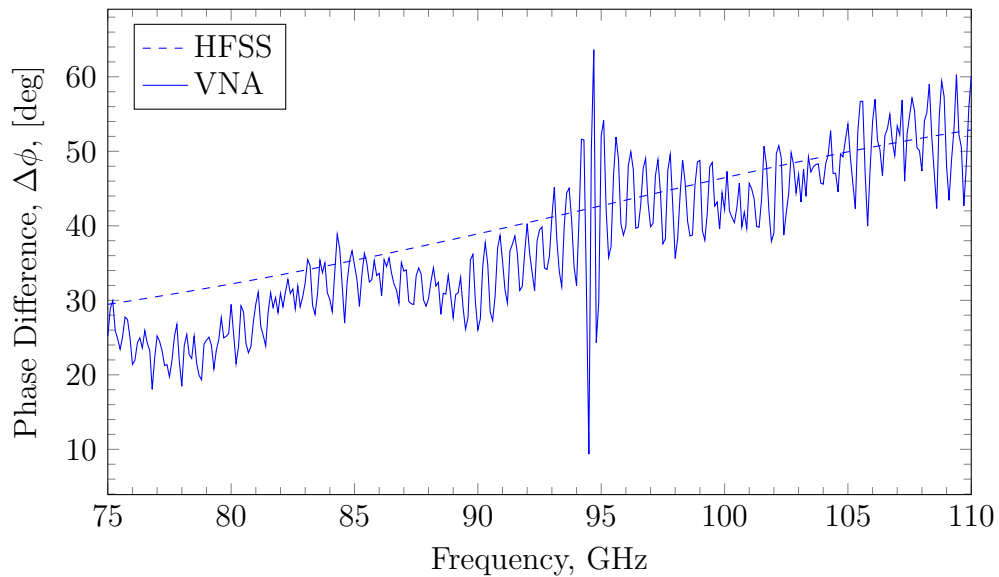


Figure 5.29: Transmitted phase difference readings of layer A measured experimentally (solid) compared to the data from a HFSS simulation (dashed) of the same layer.

simulation across most of the W-band. The  $y$ -axis readings however diverge from the expected results above 105 GHz by not decreasing in magnitude. The phase difference readings (figure 5.31) match the overall shape of the simulated data but in the GH layer's case it increases at a slower rate. This results in the blue shifting of the region where this single CWP-QWP achieves  $90^\circ$  from 102 GHz to 105 GHz. Similar behaviour was seen with the other CWP-QWPs.

The transmitted intensity and phase readings for the final hot pressed QWPs structure are shown in figure 5.32 and figure 5.33. As we can see the experimental data of the transmitted intensity does not have a good match with the expected data from the TL model. The differential phase readings on the other hand match well in the lower part of the band, between 75 GHz to 87 GHz. Above this though, where a plateauing of the phase difference is expected, the measured data continues to increase. Comparing the phase difference of this QWP to that of a single CWP-QWP the gradient of phase difference where  $90^\circ$  is crossed is shallower. The experimental data of the full QWP shows that it provides a usable fractional bandwidth of 1.4% between 86.9 GHz to 88.1 GHz. This is still small,

## 5: HIGHLY BIREFRINGENT ARTIFICIAL DIELECTRICS

but is an increase from the 0.6% of a single CWP-QWP.

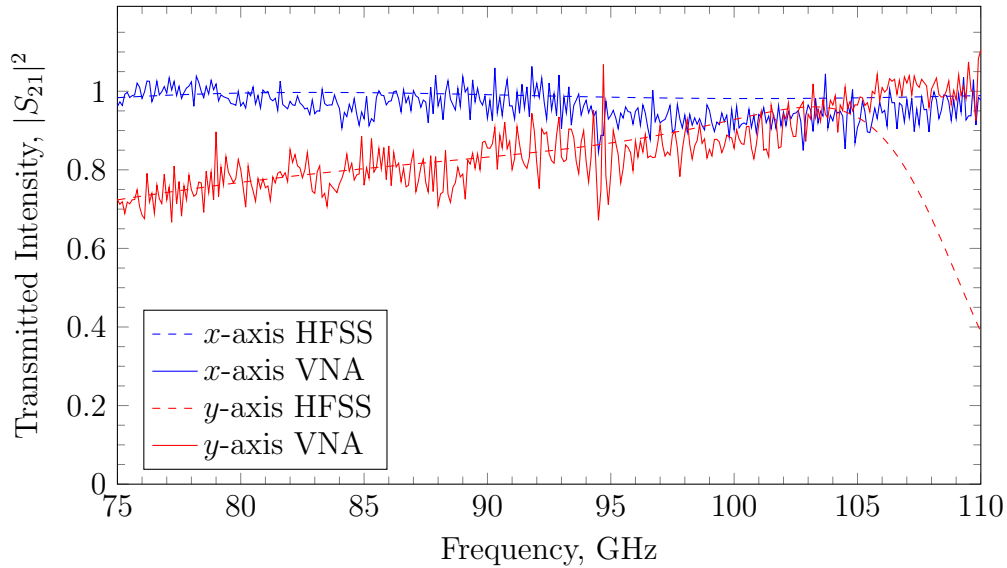


Figure 5.30: Measured (solid) and HFSS simulated (dashed) transmitted intensity readings of CWP-QWP made by spot welding layers G and H together.

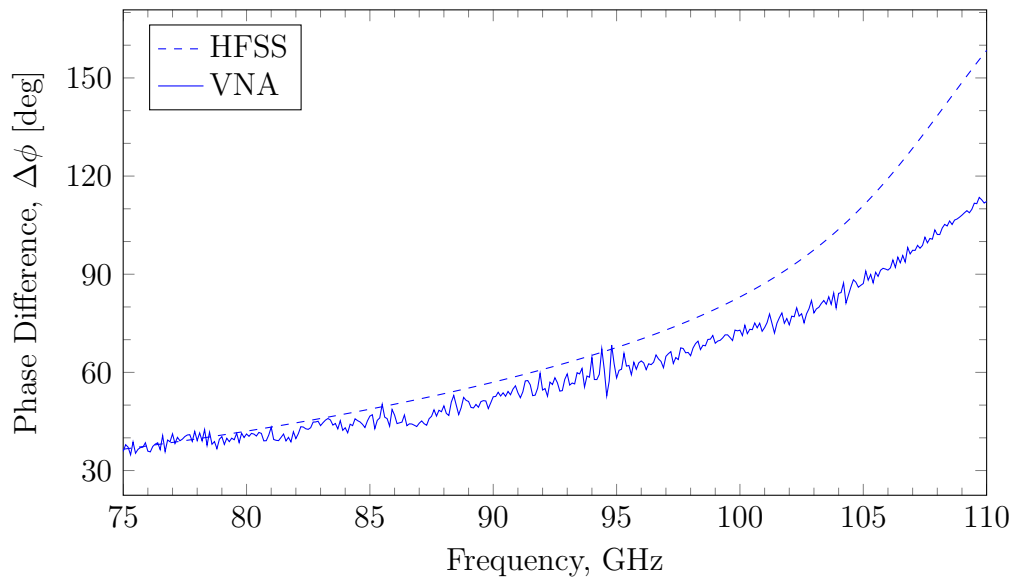


Figure 5.31: Measured (solid) and HFSS simulated (dashed) phase difference readings of CWP-QWP made by spot welding layers G and H together.

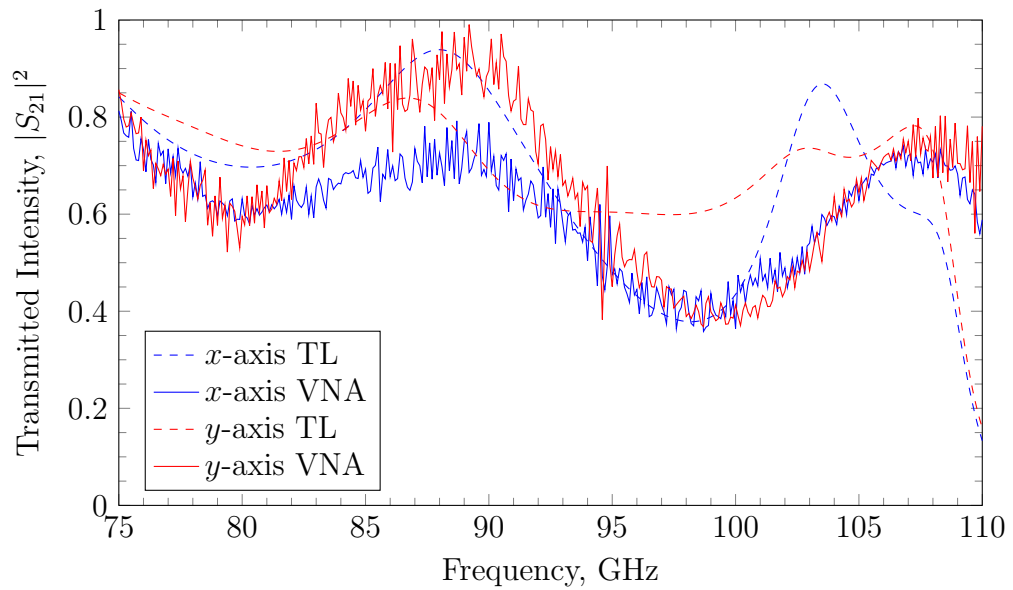


Figure 5.32: The experimental (solid) and TL modelled (dashed) of the transmitted intensity data of the full QWP.

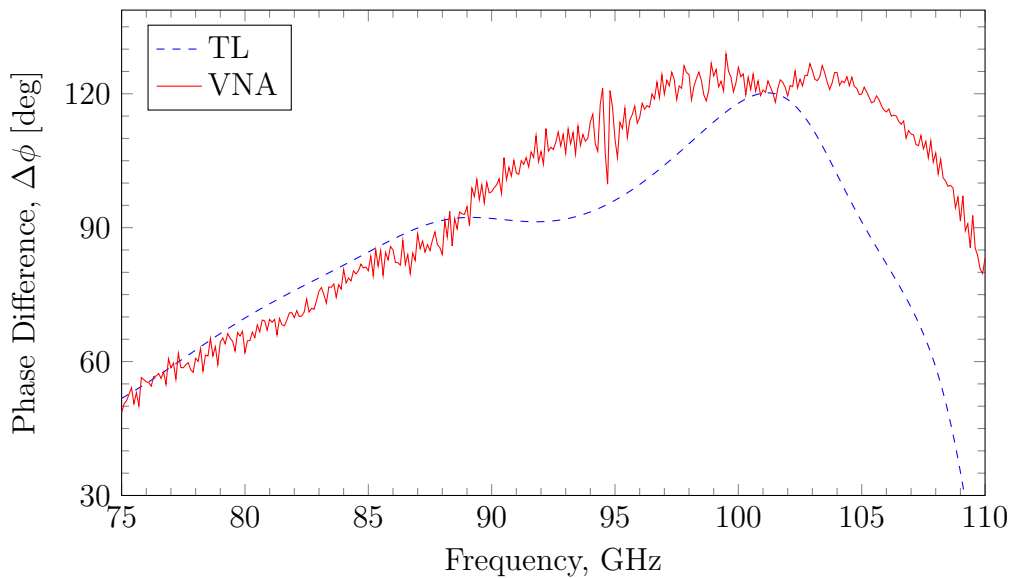


Figure 5.33: The experimental (solid) and TL modelled (dashed) of the phase difference data of the full QWP.

## 5.6 Conclusions

In this chapter, a study was carried out into the use highly birefringent metamaterial unit cells to produce wave plates. The high birefringences arise from the unit cell's ability to have a PRI along one axis and a NRI along the orthogonal axis. Defining the usable bandwidth as the region where the phase difference,  $\Delta\phi$  varies by no more than 2% of the required  $\Delta\phi$  ( $2^\circ$  for QWPs and  $3^\circ$  for HWPs) we see that these types of wave plate typically have very small usable bandwidths. Generally less than 1%. The study looked into if the Pancharatnam method could be utilised to increase this bandwidth. An air gap HWP and polypropylene embedded QWP were designed, modelled and measured for this purpose.

The air gap HWP was based upon the DBT geometry and consisted of three DBT-HWPs cascaded one after the other, with each wave plate rotated by an optimised angle. It was found that the usable bandwidth could be increased from 0.3% to 6.6%, an increase of 22 times. The embedded QWP was based on a CWP geometry and consisted of four CWP-QWPs cascaded one after the other with each plate rotated by an optimised angle. It was found that its usable bandwidth could be increased from 0.6% to 7.8%, an increase of 13 times.

The two wave plates were manufactured and tested. The air gap HWP was successful and able to show a flattening of the phase difference at the expected  $180^\circ$ , albeit with a reduced bandwidth. The embedded QWP also achieved a small widening of the phase difference at  $90^\circ$  but not as successfully as the air gap HWP. In both cases it was found that the performance of the final wave plate was highly reliant on the performance of the individual wave plates that go into making the larger device.

# Chapter 6

## Summary, Conclusions & Further Work

*All the words are going to bleed from me and I will think no more.*

Jack White, 2003 March

### 6.1 Introduction

The aim of this project was to assess whether negative refractive index (NRI) metamaterials could find a use in mm and sub-mm astronomical instrumentation. The thesis was structured with chapter 2 explaining the techniques used to simulate and model metamaterial unit cells and the devices made from them. Chapter 3 described the manufacturing process used to create individual metamaterial grids and then the assembly of larger devices from these grids. The design and manufacture of a working W-band (75 GHz to 110 GHz) NRI slab is shown in chapter 4. Lastly the designing and manufacturing of highly birefringent wave plates is in shown chapter 5. This chapter brings the thesis to a close by giving a summary of each chapter, and where relevant, the final results obtained along. An overall conclusion collects the discussion on the results obtained during this

project. Some suggestions for future work, should any be undertaken, are given at the end.

## 6.2 FEM Seeded Transmission Line Modelling

In chapter 2 a Finite Element Method (FEM) approach to simulating an infinite two-dimensional array of metamaterial unit cells was carried out using the commercial three-dimensional electromagnetic wave solver, HFSS<sup>1</sup> by Ansys. The software was used to draw, model and optimise the designs of the metamaterial unit cells using the software's various features and capabilities.

To model more complicated devices made from many layers of metamaterial unit cells such as the wave plates of chapter 5, a matrix formulation based on the Transmission Line (TL) model was used. In the TL model, matrices are used to represent the different components of the device. For example  $ABCD$  transmission matrices (equation (2.1)) were used to represent metamaterial unit cells. To ensure high accuracy from the TL models, the  $ABCD$  matrices were seeded with HFSS simulated data rather than those derived from equivalent circuits based on the metamaterials unit cells.

The accuracy of this “hybrid” or “seeded” approach was found to be very high, as long as the unit cells were kept far apart enough so that near-field interactions between the unit cells was negligible. Testing the accuracy of the TL model by comparing its results against those from a HFSS model showed that once the modelled separation was great enough, the TL model was able to provide results that differed by no more than  $\sim 10^{-4}$  for the transmitted intensity,  $|S_{21}|^2$ , and  $< 1^\circ$  for the transmitted phase,  $\arg(S_{21})$ , respectively.

The minimum distance that should be kept as the separation between unit cells in the TL model should be determined empirically via a parameter sweep changing the unit cell separation and then comparing the results of the TL model

---

<sup>1</sup><http://www.ansys.com/Products/Simulation+Technology/Electromagnetics/Signal+Integrity+&+Power+Integrity/ANSYS+HFSS>

and that of the HFSS simulation.

## 6.3 Photolithography & Grid Alignment

A step by step guide for the photolithographic process used to create metallic grids was given in chapter 3. Preparatory work begun with the mounting of polypropylene on to an aluminium ring, and annealing the polypropylene in a fan oven to make it taut and ready for copper to be deposited on its surface. Copper deposition is done using an evaporation chamber after which a uniform layer of photoresist is applied to the copper's surface with the aid of a spin coater. After harden the photoresist by heating, the copper is ready to be photolithographed.

Photolithography involves the photoresist coated copper being held beneath a "positive" photo mask whilst being exposed to ultraviolet (UV) radiation. The photo mask prevents UV light reaching the parts of the photoresisted coated copper that will form the final grid. In the exposed regions, the photoresist is broken down. The subsequent etching process involves the post UV exposed copper being dipped into a developer solution that removes the exposed photoresist. Lastly the copper is swirled around in an etching solution that removes the copper that was exposed to the UV light.

The construction of larger devices required individual grid layers to be stacked on top of one another and then aligned. Good alignment is reached through the use a light box to back light the grids, glass blocks to keep the grids flat during alignment and a loupe (handleless magnifying glass) to check the alignment. Once good alignment has been obtained the layers are spot welded to hold them in place for (if required) more layers to be aligned on top.

The preliminary performance of the spot welded device is then tested by taking transmission measurements. The individual layers in the spot welded device are then bonded together by hot pressing them within a vacuum oven.

## 6.4 Material Parameter Extraction & the Negative Refractive Index Slab

An attempt was made at creating a metamaterial slab with refractive index  $n = -1$  in chapter 4. To be able to verify the NRI behaviour a material parameter extraction code based on the method described in Chen et al. (2004) was written up. It was tested with simulated reflection and transmission data from HFSS of a variety of materials with known refractive indices, both positive and negative. The code was found to work successfully. Later a modified method was derived to handle the extraction of the parameters of a (meta)material under test (MUT) when 1) the MUT was embedded within a finite thickness of material that was not air and 2) the reflection and transmission data used for the extraction were measured in air. This modified parameter extraction method was tested using silicon embedded within a finite thickness of polypropylene. The test was successful as the silicon's refractive index was reobtained using this modified parameter extraction method.

The design process of the NRI slab was begun by using HFSS to modify and optimise a fishnet geometry from Mary et al. (2008) so it would function within the W-band and when constructed from copper and polypropylene. Further HFSS simulations were run to see how the behaviour of the fishnet design changed as its unit cells were cascaded one after the other to create a bulk metamaterial structure. It was seen that the refractive index of many cascaded cells converged such that when more unit cells are added to the cascade the refractive index no longer changes. In effect behaving like a bulk material. This result matches up with findings made in previous papers e.g. Zhou et al. (2008), Zhou et al. (2009) and Valentine et al. (2011).

A plan for a twenty-one unit cell structure was made to allow experiments able observe effects such as superlensing. During the manufacturing stage, to make the best use of materials and time, only six 21 cm diameter grids were

photolithographed allowing the construction of a three unit cell structure. These grids were aligned and hot pressed. Reflection and transmission measurements were taken with this structure and compared with HFSS simulations. Good agreement was seen in the transmitted and reflected readings of both intensity and phase. Values of the refractive index were calculated from the experimental data and it was shown that the three unit cell slab exhibited an NRI band between at least 82.2 GHz to 101.6 GHz, a fractional band of 21 %. NRI behaviour may be seen at lower frequencies but the low  $|S_{21}|^2$  values and noisy transmitted phase data makes this hard to ascertain. These experimental values were also in good match with the those calculated with HFSS simulated data. A small blue shifting of 4 GHz results in the experimental value  $n = -1$  being observed at around 90 GHz compared to the simulated value of 86.5 GHz.

The behaviour of the full twenty-one unit cell structure is expected to have similarly good match to the simulated data provided good alignment is maintained.

## 6.5 Highly Birefringent Wave Plates

In chapter 5 we moved onto applying NRI to create highly birefringent wave plates that had a positive refractive index (PRI) along one axis and a NRI in the orthogonal axis. A review of previous attempts to create wave plates with the same technique found that they were inherently narrowband with usable fractional bandwidths in the order of 0.1 %. The usable fractional bandwidth was defined as the region where differential phase,  $\Delta\phi$  was equal within 2 % of the required phase difference. The Pancharatnam method (Pancharatnam 1955a,b) was successfully utilised to broaden the usable bandwidth. The procedure was codified using a formalism previously used by Adachi and Kennaugh (1960). Two devices were designed, optimised, manufactured and experimentally tested.

### 6.5.1 Air Gap Half Wave Plate

An air gap Half Wave Plate (HWP) was designed. The process began by optimising the dimensions of a Dog Bone Triplet (DBT) unit cell so that a differential phase shift of  $180^\circ$  was achieved at 92.5 GHz with a transmitted intensity greater than 0.8 along both its axes. This single wave plate had a usable bandwidth of 0.3%. A three Dog Bone Triplet HWP transmission line model based on the Pancharatnam method was set up and the separations and rotation angles of the Dog Bone Triplets were optimised to maximise the usable bandwidth. The optimised parameters resulted in the usable bandwidth being increased to 6.6% between 88.8 GHz to 94.9 GHz, an increase of over 20 times that of a single Dog Bone Triplet HWP.

Two versions of the HWP was manufactured with photolithographed dog bone triplets mounted on aluminium rings that also acted to provide the required air gaps. Transmission measurements were taken and compared to the TL model data. The first version of the HWP performed well when comparing the values of  $|S_{21}|^2$  which demonstrated a good match. The  $\Delta\phi$  showed a flattening but at  $-150^\circ$  instead of  $-180^\circ$ . The second version of the HWP was successfully able to achieve a flat plateauing of  $\Delta\phi$  at  $-180^\circ$ , for a usable fractional bandwidth of 3.1%.

A study into the cause of the discrepancy found that misalignment of the Dog Bone grids in the triplets caused each dog bone triplet HWP to under perform and so causing the the performance of the full HWP to be affected.

### 6.5.2 Polypropylene Embedded Quarter Wave Plate

An Quarter Wave Plate (QWP) embedded within polypropylene was designed as a follow up to the air gap HWP structure. A Cut Wire Pair (CWP) design embedded within polypropylene based on that from Weis et al. (2009) and Tung et al. (2010) was optimised so that it would achieve a transmitted differential phase of  $90^\circ$  at 102 GHz. The optimised unit cell was able to achieve a usable

fractional bandwidth of 0.6 %. A four Cut Wire Pair QWP transmission line model based on the Pancharatnam method was set up and optimisations were made to the separations of the Cut Wire Pairs QWPs, their rotations and to the thickness of the polypropylene on the QWP's faces to increase the usable bandwidth. The optimised parameters resulted in fractional bandwidth being increased to 7.8 %, an increase of 13 times over a single Cut Wire Pair QWP.

The QWP was manufactured in stages. First individual layers of Cut Wires were made and transmission readings were taken to find the best performing grids. The layers were paired up and spot welded to form Cut Wire Pair QWP and their performance was assessed. Finally the full QWP structure was made and tested. The experimental data for the full QWP showed deviations from the expected results from the transmission line model results in both the  $|S_{21}|^2$  and  $\Delta\phi$  readings. Despite this a small broadening of the  $\Delta\phi$ 's usable bandwidth was observed, increasing from 0.6 % to 1.4 %, due to the shallower gradient of the phase difference when passing  $90^\circ$ .

## 6.6 Summary of Results

The following conclusions can be drawn from the work carried out during this project:

- 1) Seeding HFSS simulated data into a TL model can allow for accurate modelling of structures and devices that are constructed from a cascade of metamaterial unit cells. These results can be achieved more quickly and with less computing resources than if the full structure was simulated using FEM. Originally developed for the modelling of cascaded *single* grids, this project has shown that pairs and triplets of interacting grids can also be modelled in a TL model where the pairs and triplet are represented as a single element.
- 2) The fishnet structure is a suitable geometry from which to design and

manufacture planar NRI metamaterials in the W-band.

- 3) As can be seen from the shape of  $\text{Re}(n)$  against frequency in figure 4.44 (and similar graphs in many NRI metamaterial papers e.g. Vallecchi et al. (2009)), the  $n < 0$  band is generally very dispersive.
- 4) The Pancharatnam method can be successfully used to produce a flattening of the phase difference even if the initial gradient of the phase difference is very steep, such as the case of wave plates utilising a combination of NRI and PRI. Usable bandwidths can be increased by orders greater than ten when a system of these highly birefringent wave plates is properly optimised.
- 5) The final Pancharatnam based wave plate is also relatively thin. In this project, in the order of the operating wavelength despite being made of more than one individual wave plate. This happens because each individual plate has a subwavelength thickness due to its high birefringence.
- 6) Whilst allowing for the increase in usable bandwidth, applying the Pancharatnam method to NRI-PRI wave plates still results in wave plates with fairly small bandwidths—less than 10% for the two designed during this project. Further broadening is possible by adding more wave plates, though this would come with the disadvantage of greater absorption.

## 6.7 Conclusions

The work presented in this thesis was done with the aim of assessing if using metamaterials that exhibited NRI could improve certain optical devices used within astronomical instrumentation. Based on the results presented in the previous chapters it is the author's opinion that in their current state, NRI serves little additional benefit. Due to the need for a resonance to create a NRI in the first place, the current designs for NRI metamaterials (presented here and in the scientific literature) are highly dispersive and lossy. This can be seen in the results

for both the NRI block and the wave plates presented in chapter 4 and chapter 5 respectively.

The dispersiveness is an issue for instruments that require flat and broadband transmission properties. Wave plates used in Cosmic Microwave Background Radiation (CMBR) experiments for example can require bandwidths of  $\sim 30\%$ . However certain narrowband applications may still be found. As stated in Peralta et al. (2009), narrowband QWPs are useful for applications where only a single frequency is being studied. Indeed, the Submillimeter Array<sup>2</sup> (SMA) purposefully uses QWPs that work at only 345 GHz, the frequency close to that of the  $J = 3 \rightarrow 2$  transition of carbon monoxide's (CO) rotational states (Marrone and Rao 2008). In such cases, the highly birefringent wave plates that make use of NRI, like the HWP in section 5.4, *are* advantageous due to their thinness when compared to wave plates made of regular birefringent materials. The downside of course is that of absorption, with that of this project's single HWP reaching 0.24 at the desired phase difference.

Work using metamaterials based on the current non-interacting grids designs to produce PRI seems the more promising route to continue down. This can be seen from the many existing examples of metallic grid based devices e.g. lenses (Savini et al. 2012) and wave plates (Pisano et al. 2012b). Freed from the requirement of the creation of a resonance to produce a NRI band, a broader band (if required) and more importantly, less lossy devices can be created. Interacting grids that produce a PRI instead of a NRI like the QWP of section 5.5 also shows less absorption than its NRI counterpart.

To become useful to astronomical instrumentation, NRI metamaterials must first become less lossy. This could be done by either cooling the devices to cryogenic temperatures (Singh et al. 2010) to improve the electrical conduction of the metallic elements or creating an "active" metamaterial (Ramakrishna and Pendry 2003; Fang et al. 2011) by addition of a suitable gain medium.

---

<sup>2</sup><http://www.cfa.harvard.edu/sma/>

## 6.8 Suggestions for Further Work

### 6.8.1 Negative Refractive Index Slab

The first suggestion would be the completion of the full twenty-one unit cell slab. With a slab of this thickness it may be possible to observe effects such as superlensing and the refocussing of a radiation source near the slab's exit surface. Another interesting experiment that could be carried out is the experimental verification of the reversal of the photon orbital angular momentum carrying Laguerre-Gaussian beam's screwed wave fronts that has been predicted by Luo et al. (2008) and Xiang et al. (2010).

For possible lens applications, a polarisation independent fishnet design would need to be developed as the design presented in this thesis only show NRI for one polarisation. This can be done using different shaped holes in the fishnet design that have two orders of rotational symmetry. These include shapes such as crosses and squares for example. In addition an effort to produce a constant negative value of  $n$  over a certain bandwidth may also be interesting with regards to NRI use in lens design.

### 6.8.2 Metamaterials with Other Refractive Index Values

Other fruitful opportunities may lie beyond metamaterials with just NRI. As has been stated, metamaterials can be engineered to have electromagnetic properties of the designer's choosing. This isn't only limited to producing NRI or PRI. Values of  $n$  equal to zero have been demonstrated in e.g. Franson and Ziolkowski (2009) and possible applications include the increase of the directivity of horn antennas. This is already possible with lenses made of PRI (meta)materials, however, zero refractive index (ZRI) metamaterials would be able to do this to an extreme degree, producing a beam pattern with a top hat function shape.

# References

- S. Adachi and E. M Kennaugh (1960). “The analysis of a broad-band circular polarizer including interface reflections,” *IRE Transactions on Microwave Theory and Techniques*, **8**(5), 520–525. URL: <http://dx.doi.org/10.1109/TMTT.1960.1124780>.
- K. B. Alici and E. Ozbay (2008). “A planar metamaterial: Polarization independent fishnet structure,” *Photonics and Nanostructures - Fundamentals and Applications*, **6**(1), 102–107. URL: <http://dx.doi.org/10.1016/j.photonics.2008.01.001>.
- Ansoft (2009). *An Introduction to HFSS: Fundamental Principles, Concepts, and Use*.
- X. Chen, T. M. Grzegorzcyk, B.-I. Wu, J. Pacheco, and J. A. Kong (2004). “Robust method to retrieve the constitutive effective parameters of metamaterials,” *Physical Review E*, **70**(1), 016608. URL: <http://dx.doi.org/10.1103/PhysRevE.70.016608>.
- D. B. Davidson (2011). *Computational electromagnetics for RF and microwave engineering*. Cambridge University Press, Cambridge; New York, 2nd ed. ISBN: 9780521518918.
- B. R. Elbert (1987). *Introduction to satellite communication*. Artech House, Norwood, MA, 1st ed. ISBN: 0890062293.
- N. Engheta and R. W. Ziolkowski (2005). “A positive future for double-negative metamaterials,” *IEEE Transactions on Microwave Theory and Techniques*, **53**(4), 1535–1556. URL: <http://dx.doi.org/10.1109/TMTT.2005.845188>.

## REFERENCES

- A. Fang, Z. Huang, T. Koschny, and C. M. Soukoulis (2011). “Overcoming the losses of a split ring resonator array with gain,” *Optics Express*, **19**(13), 12688–12699. URL: <http://dx.doi.org/10.1364/OE.19.012688>.
- S. J. Franson and R. W. Ziolkowski (2009). “Confirmation of zero-n behavior in a high gain grid structure at millimeter-wave frequencies,” *Antennas and Wireless Propagation Letters, IEEE*, **8**, 387–390. URL: <http://dx.doi.org/10.1109/LAWP.2008.2002807>.
- S. Hanany, J. Hubmayr, B. R. Johnson, T. Matsumura, P. Oxley, and M. Thibodeau (2005). “Millimeter-wave achromatic half-wave plate,” *Applied Optics*, **44**(22), 4666–4670. URL: <http://dx.doi.org/10.1364/AO.44.004666>.
- A. A. Houck, J. B. Brock, and I. L. Chuang (2003). “Experimental observations of a left-handed material that obeys Snell’s law,” *Physical Review Letters*, **90** (13), 137401. URL: <http://dx.doi.org/10.1103/PhysRevLett.90.137401>.
- C. Imhof and R. Zengerle (2007). “Strong birefringence in left-handed metallic metamaterials,” *Optics Communications*, **280**(1), 213–216. URL: <http://dx.doi.org/10.1016/j.optcom.2007.07.033>.
- A. Ladu and G. Pisano (2013). “A new broadband microstrip quadrature hybrid with very flat phase response,” *Progress In Electromagnetics Research C*, **34**, 227–237. URL: <http://www.jpier.org/PIERC/pier.php?paper=12090305>.
- J. W. Lamb (1996). “Miscellaneous data on materials for millimetre and submillimetre optics,” *International Journal of Infrared and Millimeter Waves*, **17** (12), 1997–2034. URL: <http://dx.doi.org/10.1007/BF02069487>.
- R. S. Longhurst (1986). *Geometrical And Physical Optics*. Longman, London, 2nd ed. ISBN: 9788125016236.
- H. Luo, Z. Ren, W. Shu, and S. Wen (2008) “Reversed propagation dynamics of Laguerre-Gaussian beams in left-handed materials,” *Physical Review A*, **77**(2), 023812. URL: <http://dx.doi.org/10.1103/PhysRevA.77.023812>
- N. Marcuvitz (ed) (1965). *Waveguide Handbook*, volume 10 of *Massachusetts*

- Institute of Technology Radiation Laboratory*. Dover Publications Inc., New York.
- D. P. Marrone and R. Rao (2008). “The submillimeter array polarimeter,” *In*: W. D. Duncan, W. S. Holland, S. Withington, and J. Zmuidzinas, (eds), *Millimeter and Submillimeter Detectors and Instrumentation for Astronomy IV*, **7020**, 70202B, Marseille, France. SPIE. URL: <http://dx.doi.org/10.1117/12.788677>.
- A. Mary, S. G. Rodrigo, F. J. Garcia-Vidal, and L. Martin-Moreno (2008). “Theory of negative-refractive-index response of double-fishnet structures,” *Physical Review Letters*, **101**(10), 103902. URL: <http://dx.doi.org/10.1103/PhysRevLett.101.103902>.
- H. O. Moser, L. K. Jian, H. S. Chen, M. Bahou, S. M. P. Kalaiselvi, S. Virasawmy, S. M. Maniam, X. X. Cheng, S. P. Heussler, S. bin Mahmood, and B.-I. Wu (2009). “Self-supported all-metal THz metamaterials,” *In*: M. A. Noginov, N. I. Zheludev, A. D. Boardman, and N. Engheta, (eds), *Metamaterials: Fundamentals and Applications II*, **7392**, 73920E, San Diego, CA, USA. SPIE. URL: <http://dx.doi.org/10.1117/12.826679>.
- A. M. Nicolson and G. F. Ross (1970). “Measurement of the intrinsic properties of materials by time-domain techniques,” *IEEE Transactions on Instrumentation and Measurement*, **19**(4), 377–382. URL: <http://dx.doi.org/10.1109/TIM.1970.4313932>.
- S. J. Orfanidis (2010). *Electromagnetic Waves and Antennas*. URL: <http://eceweb1.rutgers.edu/~orfanidi/ewa/>.
- S. Pancharatnam (1955a). “Achromatic combinations of birefringent plates. Part I. An achromatic circular polarizer,” *Proceedings of the Indian Academy of Sciences, Section A*, **41**(4), 130–136. URL: <http://repository.ias.ac.in/31454/>.
- S. Pancharatnam (1955b). “Achromatic combinations of birefringent plates. Part II. An achromatic quarter-wave plate,” *Proceedings of the Indian Academy of Sciences, Section A*, **41**(4), 137–144. URL: <http://repository.ias.ac.in/31460/>.

## REFERENCES

- O. Paul, C. Imhof, B. Reinhard, R. Zengerle, and R. Beigang (2008). “Negative index bulk metamaterial at terahertz frequencies,” *Optics Express*, **16**(9), 6736–6744. URL: <http://dx.doi.org/10.1364/OE.16.006736>.
- J. B. Pendry (2000). “Negative refraction makes a perfect lens,” *Physical Review Letters*, **85**(18), 3966. URL: <http://dx.doi.org/10.1103/PhysRevLett.85.3966>.
- J. B. Pendry, A. J. Holden, W. J. Stewart, and I. Youngs (1996). “Extremely low frequency plasmons in metallic mesostructures,” *Physical Review Letters*, **76**(25), 4773. URL: <http://dx.doi.org/10.1103/PhysRevLett.76.4773>.
- J. B. Pendry, A. J. Holden, D. J. Robbins, and W. J. Stewart (1998). “Low frequency plasmons in thin-wire structures,” *Journal of Physics: Condensed Matter*, **10**(22), 4785–4809. URL: <http://dx.doi.org/10.1088/0953-8984/10/22/007>.
- J. B. Pendry (2004). “Negative refraction,” *Contemporary Physics*, **45**(3), 191–202. URL: <http://dx.doi.org/10.1080/00107510410001667434>.
- J. B. Pendry, A. J. Holden, D. J. Robbins, and W. J. Stewart (1999). “Magnetism from conductors and enhanced nonlinear phenomena,” *IEEE Transactions on Microwave Theory and Techniques*, **47**(11), 2075–2084. URL: <http://dx.doi.org/10.1109/22.798002>.
- X. G. Peralta, E. I. Smirnova, A. K. Azad, H.-T. Chen, A. J. Taylor, I. Brener, and J. F. O’Hara (2009). “Metamaterials for THz polarimetric devices,” *Optics Express*, **17**(2), 773783. URL: <http://dx.doi.org/10.1364/OE.17.000773>.
- G. Pisano, S. Melhuish, G. Savini, L. Piccirillo, and B. Maffei (2011). “A broadband w-band polarization rotator with very low cross polarization,” *IEEE Microwave and Wireless Components Letters*, **21**(3), 127–129. URL: <http://dx.doi.org/10.1109/LMWC.2011.2104942>.
- G. Pisano, R. Nesti, M. W. Ng, A. Orfei, D. Panella, and P. Wilkinson (2012a). “A novel broadband q-band polarizer with very flat phase response,” *Journal of Electromagnetic Waves and Applications*, **26**(5–6), 707–715. URL: <http://dx.doi.org/10.1080/10497315.2012.707715>.

- [//dx.doi.org/10.1080/09205071.2012.710795](http://dx.doi.org/10.1080/09205071.2012.710795).
- G. Pisano, M. W. Ng, V. Haynes, and B. Maffei (2012b). “A broadband metal-mesh half-wave plate for millimetre wave linear polarisation rotation,” *Progress In Electromagnetics Research M*, **25**, 101–114. URL: <http://www.jpier.org/PIERM/pier.php?paper=12051410>.
- G. Pisano, M. W. Ng, V. Haynes, and B. Maffei (2012c). “A broadband photolithographic polariser for millimetre wave applications,” *In: PIERS 2012 Kuala Lumpur Proceedings*, 1748–1751, Kuala Lumpur, Malaysia. The Electromagnetics Academy. ISBN: 978-1-934142-20-2.
- G. Pisano, M. W. Ng, F. Ozturk, B. Maffei, and V. Haynes (2013). “Dielectrically embedded flat mesh lens for millimeter waves applications,” *Applied Optics*, **52** (11), 2218–2225. URL: <http://dx.doi.org/10.1364/AO.52.002218>.
- D. M. Pozar (2012). *Microwave engineering*. Wiley, Hoboken, NJ, 4th ed. ISBN: 9780470631553.
- S. Anantha Ramakrishna (2005). “Physics of negative refractive index materials,” *Reports on Progress in Physics*, **68**(2), 449–521. URL: <http://dx.doi.org/10.1088/0034-4885/68/2/R06>.
- S. Anantha Ramakrishna and J. B. Pendry (2003). “Removal of absorption and increase in resolution in a near-field lens via optical gain,” *Physical Review B*, **67**(20), 201101. URL: <http://dx.doi.org/10.1103/PhysRevB.67.201101>.
- R. Rashed (1990). “A pioneer in anaclastics: Ibn Sahl on burning mirrors and lenses,” *Isis*, **81**(3), 464–491. URL: <http://dx.doi.org/10.1086/355456>.
- G. Savini, G. Pisano, and P. A. R. Ade (2006). “Achromatic half-wave plate for submillimeter instruments in cosmic microwave background astronomy: modeling and simulation,” *Applied Optics*, **45**(35), 8907–8915. URL: <http://dx.doi.org/10.1364/AO.45.008907>.
- G. Savini, P. A. R. Ade, and J. Zhang (2012). “A new artificial material approach for flat THz frequency lenses,” *Optics Express*, **20**(23), 25766–25773. URL: <http://dx.doi.org/10.1364/OE.20.025766>.

## REFERENCES

- <http://dx.doi.org/10.1364/OE.20.025766>.
- D. Schurig and D. Smith (2004). “Negative index lens aberrations,” *Physical Review E*, **70**(6). URL: <http://dx.doi.org/10.1103/PhysRevE.70.065601>.
- A. Schuster (1904). *An Introduction to the Theory of Optics*. Edward Arnold, London. URL: <https://archive.org/details/anintroductiont01schugoog>.
- V. M. Shalaev, W. Cai, U. K. Chettiar, H.-K. Yuan, A. K. Sarychev, V. P. Drachev, and A. V. Kildishev (2005). “Negative index of refraction in optical metamaterials,” *Optics Letters*, **30**(24), 3356–3358. URL: <http://dx.doi.org/10.1364/OL.30.003356>.
- R. A. Shelby, D. R. Smith, S. C. Nemat-Nasser, and S. Schultz (2001a). “Microwave transmission through a two-dimensional, isotropic, left-handed metamaterial,” *Applied Physics Letters*, **78**(4), 489–491. URL: <http://dx.doi.org/10.1063/1.1343489>.
- R. A. Shelby, D. R. Smith, and S. Schultz (2001b). “Experimental verification of a negative index of refraction,” *Science*, **292**(5514), 77–79. URL: <http://dx.doi.org/10.1126/science.1058847>.
- R. Singh, Z. Tian, J. Han, C. Rockstuhl, J. Gu, and W. Zhang (2010). “Cryogenic temperatures as a path toward high-Q terahertz metamaterials,” *Applied Physics Letters*, **96**(7), 071114. URL: <http://dx.doi.org/10.1063/1.3313941>.
- D. R. Smith, W. J. Padilla, D. C. Vier, S. C. Nemat-Nasser, and S. Schultz (2000). “Composite medium with simultaneously negative permeability and permittivity,” *Physical Review Letters*, **84**(18), 4184–4187. URL: <http://dx.doi.org/10.1103/PhysRevLett.84.4184>.
- D. R. Smith, S. Schultz, P. Markoš, and C. M. Soukoulis (2002). “Determination of effective permittivity and permeability of metamaterials from reflection and transmission coefficients,” *Physical Review B*, **65**(19), 195104. URL: <http://dx.doi.org/10.1103/PhysRevB.65.195104>.
- C. M. Soukoulis, S. Linden, and M. Wegener (2007). “Negative refractive index

- at optical wavelengths,” *Science*, **315**(5808), 47–49. URL: <http://dx.doi.org/10.1126/science.1136481>.
- R. Storn and K. Price (1997). “Differential evolution – a simple and efficient heuristic for global optimization over continuous spaces,” *Journal of Global Optimization*, **11**(4), 341–359. URL: <http://dx.doi.org/10.1023/A:1008202821328>.
- J. Tang and S. He (2010). “A novel structure for double negative NIMs towards UV spectrum with high FOM,” *Optics Express*, **18**(24), 25256–25263. URL: <http://dx.doi.org/10.1364/OE.18.025256>.
- H. Tao, W. J. Padilla, X. Zhang, and R. D. Averitt (2010). “Recent progress in electromagnetic metamaterial devices for terahertz applications,” *IEEE Journal of Selected Topics in Quantum Electronics*, **17**(1), 92–101. URL: <http://dx.doi.org/10.1109/JSTQE.2010.2047847>.
- A. M. Title (1975). “Improvement of birefringent filters. 2:Achromatic waveplates,” *Applied Optics*, **14**(1), 229–237. URL: <http://dx.doi.org/10.1364/AO.14.000229>.
- N. T. Tung, V. T. T. Thuy, J. W. Park, J. Y. Rhee, and Y. Lee (2010). “Left-handed transmission in a simple cut-wire pair structure,” *Journal of Applied Physics*, **107**(2), 023530. URL: <http://dx.doi.org/10.1063/1.3298505>.
- R. Ulrich (1967). “Far-infrared properties of metallic mesh and its complementary structure,” *Infrared Physics*, **7**(1), 37–55. URL: [http://dx.doi.org/10.1016/0020-0891\(67\)90028-0](http://dx.doi.org/10.1016/0020-0891(67)90028-0).
- J. Valentine, S. Zhang, T. Zentgraf, and X. Zhang (2011). “Development of bulk optical negative index fishnet metamaterials: Achieving a low-loss and broadband response through coupling,” *Proceedings of the IEEE*, **99**(10), 1682–1690. URL: <http://dx.doi.org/10.1109/JPROC.2010.2094593>.
- A. Vallecchi, F. Capolino, and A. G. Schuchinsky (2009). “2-D isotropic effective negative refractive index metamaterial in planar technology,” *IEEE Microwave and Wireless Components Letters*, **19**(5), 269–271. URL: <http://dx.doi.org/10.1109/LMWC.2009.2017585>.

## REFERENCES

- A. Vallecchi and F. Capolino (2009). “Tightly coupled tripole conductor pairs as constituents for a planar 2D-Isotropic negative refractive index metamaterial,” *Optics Express*, **17**(17), 15216–15227. URL: <http://dx.doi.org/10.1364/OE.17.015216>.
- V. G. Veselago (1968). “The electrodynamics of substances with simultaneously negative values of  $\epsilon$  and  $\mu$ ,” *Soviet Physics Uspekhi*, **10**(4), 509–514. URL: <http://dx.doi.org/10.1070/PU1968v010n04ABEH003699>.
- W. B. Weir (1974). “Automatic measurement of complex dielectric constant and permeability at microwave frequencies,” *Proceedings of the IEEE*, **62**(1), 33–36. <http://dx.doi.org/10.1109/PROC.1974.9382>.
- P. Weis, O. Paul, C. Imhof, R. Beigang, and M. Rahm (2009). “Strongly birefringent metamaterials as negative index terahertz wave plates,” *Applied Physics Letters*, **95**(17), 171104. URL: <http://dx.doi.org/10.1063/1.3253414>.
- T.-K. Wu (1994). “Meander-line polarizer for arbitrary rotation of linear polarization,” *IEEE Microwave and Guided Wave Letters*, **4**(6), 199–201. URL: <http://dx.doi.org/10.1109/75.294292>.
- Y. Xiang, H. Luo, and S. Wen (2010). “Intensity and phase rotation of beams in left-handed metamaterials,” *High Power Laser and Particle Beams*, **22**(8), 1834–1838. URL: <http://dx.doi.org/10.3788/HPLPB20102208.1834>.
- T. Xu, A. Agrawal, M. Abashin, K. J. Chau, and H. J. Lezec (2013). “All-angle negative refraction and active flat lensing of ultraviolet light,” *Nature*, **497** (7450), 470–474. URL: <http://dx.doi.org/10.1038/nature12158>.
- W. S. Zaoui, K. Chen, W. Vogel, and M. Berroth (2012). “Low loss broadband polarization independent fishnet negative index metamaterial at 40 GHz,” *Photonics and Nanostructures - Fundamentals and Applications*, **10**(3), 245–250. URL: <http://dx.doi.org/10.1016/j.photonics.2011.02.003>.
- S. Zhang, W. Fan, N. C. Panoiu, K. J. Malloy, R. M. Osgood, and S. R. J. Brueck (2005). “Experimental demonstration of near-infrared negative-index

- metamaterials,” *Physical Review Letters*, **95**(13), 137404. URL: <http://dx.doi.org/10.1103/PhysRevLett.95.137404>.
- L. Zhi-Li, D. Jie-Chen, and Z. Pu (2008). “Aberration-free two-thin-lens systems based on negative-index materials,” *Chinese Physics B*, **17**(3), 954–959. URL: <http://dx.doi.org/10.1088/1674-1056/17/3/035>.
- J. Zhou, T. Koschny, M. Kafesaki, E. Economou, J. B. Pendry, and C. Soukoulis (2005). “Saturation of the magnetic response of split-ring resonators at optical frequencies,” *Physical Review Letters*, **95**(22), 223902. URL: <http://dx.doi.org/10.1103/PhysRevLett.95.223902>.
- J. Zhou, T. Koschny, L. Zhang, G. Tuttle, and C. M. Soukoulis (2006). “Experimental demonstration of negative index of refraction,” *Applied Physics Letters*, **88**(22), 221103. URL: <http://dx.doi.org/10.1063/1.2208264>.
- J. Zhou, T. Koschny, M. Kafesaki, and C. M. Soukoulis (2008). “Size dependence and convergence of the retrieval parameters of metamaterials,” *Photonics and Nanostructures - Fundamentals and Applications*, **6**(1), 96–101. URL: <http://dx.doi.org/10.1016/j.photonics.2007.10.003>.
- J. Zhou, T. Koschny, M. Kafesaki, and C. M. Soukoulis (2009). “Negative refractive index response of weakly and strongly coupled optical metamaterials,” *Physical Review B*, **80**(3), 035109. URL: <http://dx.doi.org/10.1103/PhysRevB.80.035109>.
- R. W. Ziolkowski and E. Heyman (2001). “Wave propagation in media having negative permittivity and permeability,” *Physical Review E*, **64**(5), 056625. URL: <http://dx.doi.org/10.1103/PhysRevE.64.056625>.

*REFERENCES*

*And for my final words: 'Cause  
trouble. Please.'*

Prof. I. Browne, 2012 May

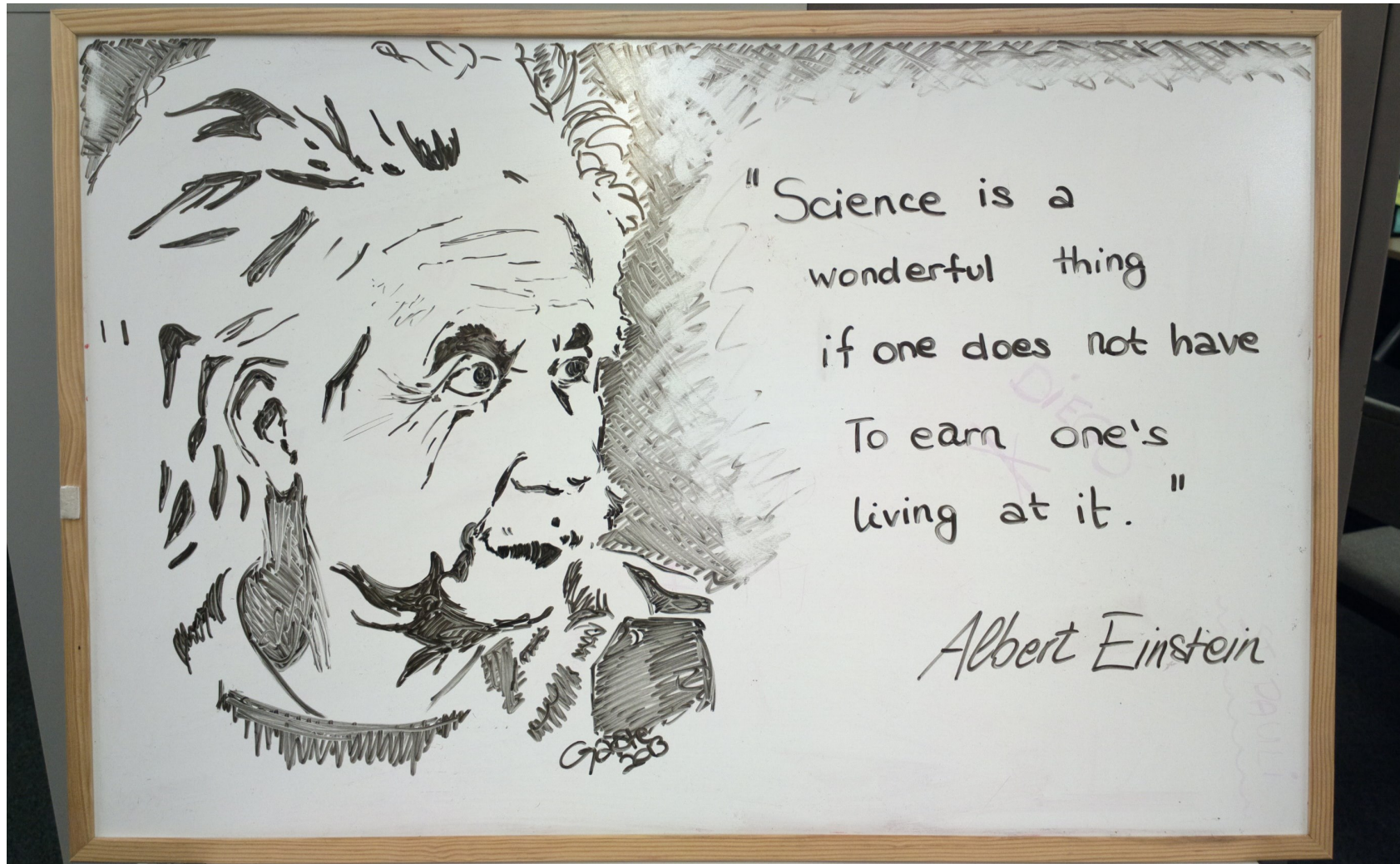


Figure 6.1: Words supposedly by Albert Einstein, 1951 March. Art definitely by Stefania Maccalli, 2013 September.